

THE MILKY WAY TOMOGRAPHY WITH SLOAN DIGITAL SKY SURVEY. IV. DISSECTING DUST

MICHAEL BERRY^{1,2}, ŽELJKO IVEZIĆ¹, BRANIMIR SESAR³, MARIO JURIC^{4,19}, EDWARD F. SCHLAFLY⁵, JILLIAN BELLOVARY⁶,
DOUGLAS FINKBEINER⁵, DIJANA VRBANEC⁷, TIMOTHY C. BEERS^{8,9}, KEIRA J. BROOKS¹, DONALD P. SCHNEIDER¹⁰,
ROBERT R. GIBSON¹, AMY KIMBALL¹¹, LYNNE JONES¹, PETER YOACHIM¹, SIMON KRUGHOFF¹, ANDREW J. CONNOLLY¹,
SARAH LOEBMAN¹, NICHOLAS A. BOND², DAVID SCHLEGEL¹², JULIANNE DALCANTON¹, BRIAN YANNY¹³, STEVEN R. MAJEWSKI¹⁴,
GILLIAN R. KNAPP¹⁵, JAMES E. GUNN¹⁵, J. ALLYN SMITH¹⁶, MASATAKA FUKUGITA¹⁷, STEVE KENT¹³, JOHN BARENTINE¹⁸,
JUREK KRZESINSKI¹⁸, AND DAN LONG¹⁸

¹ Department of Astronomy, University of Washington, Box 351580, Seattle, WA 98195, USA

² Physics and Astronomy Department, Rutgers University, Piscataway, NJ 08854-8019, USA

³ Division of Physics, Mathematics and Astronomy, Caltech, Pasadena, CA 91125, USA

⁴ Harvard College Observatory, 60 Garden Street, Cambridge, MA 02138, USA

⁵ Harvard-Smithsonian Center for Astrophysics, 60 Garden Street, Cambridge, MA 02138, USA

⁶ Department of Astronomy, University of Michigan, Ann Arbor, MI, USA

⁷ Department of Physics, Faculty of Science, University of Zagreb, Bijenička cesta 32, 10000 Zagreb, Croatia

⁸ National Optical Astronomy Observatories, Tucson, AZ 85719, USA

⁹ Department of Physics & Astronomy and JINA, Joint Institute for Nuclear Astrophysics, Michigan State University, East Lansing, MI 48824, USA

¹⁰ Department of Astronomy and Astrophysics, The Pennsylvania State University, University Park, PA 16802, USA

¹¹ National Radio Astronomy Observatory, 520 Edgemont Road, Charlottesville, VA 22903-2475, USA

¹² Lawrence Berkeley National Laboratory, One Cyclotron Road, MS 50R5032, Berkeley, CA 94720, USA

¹³ Fermi National Accelerator Laboratory, P.O. Box 500, Batavia, IL 60510, USA

¹⁴ Department of Astronomy, University of Virginia, P.O. Box 400325, Charlottesville, VA 22904-4325, USA

¹⁵ Princeton University Observatory, Princeton, NJ 08544, USA

¹⁶ Department of Physics & Astronomy, Austin Peay State University, Clarksville, TN 37044, USA

¹⁷ Institute for Cosmic Ray Research, University of Tokyo, Kashiwa, Chiba, Japan

¹⁸ Apache Point Observatory, 2001 Apache Point Road, P.O. Box 59, Sunspot, NM 88349-0059, USA

Received 2011 November 18; accepted 2012 July 1; published 2012 September 14

ABSTRACT

We use Sloan Digital Sky Survey (SDSS) photometry of 73 million stars to simultaneously constrain best-fit main-sequence stellar spectral energy distribution (SED) and amount of dust extinction along the line of sight toward each star. Using a subsample of 23 million stars with Two Micron All Sky Survey (2MASS) photometry, whose addition enables more robust results, we show that SDSS photometry alone is sufficient to break degeneracies between intrinsic stellar color and dust amount when the shape of extinction curve is fixed. When using both SDSS and 2MASS photometry, the ratio of the total to selective absorption, R_V , can be determined with an uncertainty of about 0.1 for most stars in high-extinction regions. These fits enable detailed studies of the dust properties and its spatial distribution, and of the stellar spatial distribution at low Galactic latitudes ($|b| < 30^\circ$). Our results are in good agreement with the extinction normalization given by the Schlegel et al. (SFD) dust maps at high northern Galactic latitudes, but indicate that the SFD extinction map appears to be consistently overestimated by about 20% in the southern sky, in agreement with recent study by Schlafly et al. The constraints on the shape of the dust extinction curve across the SDSS and 2MASS bandpasses disfavor the reddening law of O'Donnell, but support the models by Fitzpatrick and Cardelli et al. For the latter, we find a ratio of the total to selective absorption to be $R_V = 3.0 \pm 0.1(\text{random}) \pm 0.1(\text{systematic})$ over most of the high-latitude sky. At low Galactic latitudes ($|b| < 5^\circ$), we demonstrate that the SFD map cannot be reliably used to correct for extinction because most stars are embedded in dust, rather than behind it, as is the case at high Galactic latitudes. We analyze three-dimensional maps of the best-fit R_V and find that $R_V = 3.1$ cannot be ruled out in any of the 10 SEGUE stripes at a precision level of ~ 0.1 – 0.2 . Our best estimate for the intrinsic scatter of R_V in the regions probed by SEGUE stripes is ~ 0.2 . We introduce a method for efficient selection of candidate red giant stars in the disk, dubbed “dusty parallax relation,” which utilizes a correlation between distance and the extinction along the line of sight. We make these best-fit parameters, as well as all the input SDSS and 2MASS data, publicly available in a user-friendly format. These data can be used for studies of stellar number density distribution, the distribution of dust properties, for selecting sources whose SED differs from SEDs for high-latitude main-sequence stars, and for estimating distances to dust clouds and, in turn, to molecular gas clouds.

Key words: catalogs – dust, extinction – stars: statistics – surveys

Online-only material: color figures

1. INTRODUCTION

From our vantage point inside the disk of the Milky Way, we have a unique opportunity to study a fairly typical spiral

galaxy in great detail. By measuring and analyzing the properties of large numbers of individual stars, we can map the Milky Way in a nine-dimensional space spanned by the three spatial coordinates, three velocity components, and the three main stellar parameters—luminosity, effective temperature, and metallicity. In a series of related studies, we used data obtained

¹⁹ Hubble Fellow.

by the Sloan Digital Sky Survey (SDSS; York et al. 2000) to study in detail the distribution of tens of millions of stars in this multi-dimensional space. In Jurić et al. (2008, hereafter J08), we examined the spatial distribution of stars in the Galaxy; in Ivezić et al. (2008a, hereafter I08), we extended our analysis to include the metallicity distribution; and in Bond et al. (2010, hereafter B10), we investigated the distribution of stellar velocities. In M. Jurić et al. (in preparation), we estimate stellar luminosity functions for disk and halo stars, and describe an empirical Galaxy model and corresponding publicly available modeling code that encapsulate these SDSS-based results.

All of the above studies were based on SDSS data at high Galactic latitudes ($|b| > 30^\circ$). Meanwhile, the second phase of SDSS has delivered imaging data for ten ~ 2.5 wide stripes (in SDSS terminology, two independent observing runs produce two interleaving strips, which form a stripe; see Stoughton et al. 2002) that cross the Galactic plane (the so-called Sloan Extension for Galactic Understanding and Exploration (SEGUE) data; see Yanny et al. 2009). At least in principle, these data can be used to extend the above analysis much closer to the mid-plane of the Galaxy, and to search for evidence of effects such as disk warp and disk flare.

However, at low Galactic latitudes sampled by SEGUE data, there are severe problems with the interstellar dust extinction corrections. High-latitude SDSS data are typically corrected for interstellar extinction using maps from Schlegel et al. (1998, hereafter SFD). When the full SFD extinction correction is applied to low-latitude data, the resulting color–magnitude and color–color diagrams have dramatically different morphology than those observed at high Galactic latitudes. Parameterizations developed by J08 suggest that these problems are predominantly due to the fact that stars are embedded in the dust layer, rather than behind it (the latter is an excellent approximation for most stars at high Galactic latitudes), and thus the SFD extinction value is an overestimate for most stars. This conclusion is also supported by other Galaxy models, such as Besançon (Robin et al. 2003) and TRILEGAL (Girardi et al. 2005). Therefore, in order to fully exploit SEGUE data, both the intrinsic colors of a given star and the amount of dust extinction along the line of sight to the star have to be known. Distances to stars, which can be derived using appropriate photometric parallax relations (see I08), would then enable mapping of the stellar spatial distribution. The interstellar medium (ISM) dust distribution and dust extinction properties are interesting in their own right (e.g., Fitzpatrick & Massa 2009; Draine 2011, and references therein). An additional strong motivation for quantifying stellar and dust distribution close to the Galactic plane is to inform the planning of the Large Synoptic Survey Telescope (LSST) survey, which is considering deep multi-band coverage of the Galactic plane²⁰ (Ivezić et al. 2008b).

The amount of dust can be constrained by measuring dust extinction and/or reddening, typically at UV, optical, and near-IR wavelengths, by measuring dust emission at far-IR wavelengths, and by employing a tracer of ISM, such as H I gas. For example, in their pioneering studies in the late 1960s, Shane & Wirtanen used galaxy counts, and Knapp & Kerr (1974) exploited a correlation between dust and H I column densities to infer the amount of dust extinction. The most widely used contemporary dust map (SFD) is derived from observations of dust emission at $100 \mu\text{m}$ and $240 \mu\text{m}$, and has

an angular resolution of ~ 6 arcmin (the temperature correction applied to IRAS $100 \mu\text{m}$ data is based on DIRBE $100 \mu\text{m}$ and $240 \mu\text{m}$ data, and has a lower angular resolution of $\sim 1^\circ$; see SFD for more details). It has been found that the SFD map sometimes overestimates the dust column by 20%–30% when the dust extinction in the SDSS r band, $A_r \sim 0.85 A_V$, exceeds 0.5 mag (e.g., Arce & Goodman 1999). Such an error may be due to confusion of the background emission and that from point sources. A generic shortcoming of the far-IR emission-based methods is that they cannot provide constraints on the three-dimensional distribution of dust; instead, only the total amount of dust along the line of sight to infinity is measured. In addition, the far-IR data provide no constraints for the wavelength dependence of extinction at UV, optical, and near-IR wavelengths.

With the availability of wide-angle digital sky surveys at optical and near-IR wavelengths, such as SDSS and Two Micron All Sky Survey (2MASS; see Section 2 for more details), it is now possible to study the effects of dust extinction using many tens of millions of sources. For example, Schlafly et al. (2010, hereafter Sch2010) utilized colors of blue stars, and Peek & Graves (2010) utilized colors of passive red galaxies, to estimate errors in the SFD map at high Galactic latitudes. In both studies, *the dust reddening is assumed constant within small sky patches*, and the color distribution for a large number of sources from a given patch is used to infer the mean reddening (Peek & Graves dub this approach the “standard crayon” method). Traditional dust reddening estimation methods where the “true” color of a star is determined using spectroscopy were extended to the extensive SDSS spectroscopic data set by Schlafly & Finkbeiner (2010) and Jones et al. (2011); they obtained results consistent with the above “standard crayon” methods. Studies of dust extinction with SDSS data are limited to $A_V \lesssim 10$; 2MASS data alone can be used to trace dust up to $A_V \sim 20$ using the near-infrared color excess method (Lombardi & Alves 2001; Lombardi et al. 2011; Majewski et al. 2011), though estimates of stellar distances are not as reliable as with SDSS data.

In this work, we extend these studies to low Galactic latitudes where stars are embedded in dust, and also investigate whether optical and near-IR photometry are sufficient to constrain the shape of the dust extinction curve. We estimate dust extinction along the line of sight to *each detected star* by simultaneously fitting its observed optical/IR spectral energy distribution (SED) using an empirical library of intrinsic reddening-free SEDs, a reddening curve described by the standard parameters: $R_V = A_V/E(B - V)$, and the dust extinction along the line of sight in the SDSS r band, A_r . We first select a dust extinction parameterization using high Galactic latitude data and another variation of the “standard crayon” method that incorporates the eight-band SDSS–2MASS photometry. Our SED fitting method that treats each star separately allows an estimation of the three-dimensional spatial distributions of both stars and dust. The data set and methodology, including various tests of the adopted algorithm, are described in Section 2. Results are analyzed in Section 3, and a preliminary investigation of the three-dimensional stellar count distribution and the distribution of dust properties is presented in Section 4. The main results are summarized and discussed in Section 5.

2. DATA AND METHODOLOGY

We first describe the data used in this work, and then discuss methodology, including various tests of the adopted algorithm. All data sets used in this study are defined using

²⁰ See also Chapters 6 and 7 in the LSST Science Book available from www.lsst.org/lsst/scibook.

SDSS imaging data for unresolved sources. Objects that are positionally associated with 2MASS sources are a subset of the full SDSS sample. Although the SDSS–2MASS data set is expected to provide better performance than SDSS data alone when estimating dust properties and intrinsic stellar colors, we also consider the SDSS data set alone (hereafter referred to as “only-SDSS”) because it is effectively deeper (unless the dust extinction in the SDSS r band is larger than several magnitudes). We start by briefly describing the SDSS and 2MASS surveys.

2.1. SDSS Survey

The properties of the SDSS are documented in Fukugita et al. (1996), Gunn et al. (1998), Hogg et al. (2001), Smith et al. (2002), Stoughton et al. (2002), Pier et al. (2003), Ivezić et al. (2004), Tucker et al. (2006), and Gunn et al. (2006). In addition to its imaging survey data, SDSS has obtained well over half a million stellar spectra, many as part of the SEGUE (Yanny et al. 2009). Here, we only reiterate that the survey photometric catalogs are 95% complete to a depth of $r \sim 22$, with photometry accurate to ~ 0.02 mag (both absolute and root-mean-square, rms, error) for sources not limited by Poisson statistics. Sources with $r < 20.5$ have astrometric errors less than 0.1 arcsec per coordinate (rms; Pier et al. 2003), and robust star/galaxy separation²¹ is achieved for $r \lesssim 21.5$ (Lupton et al. 2001).

The SDSS Data Release 7 (Abazajian et al. 2009) used in this work contains photometric and astrometric data for 357 million unique objects,²² detected in 11,663 deg². About half of these objects are unresolved and are dominated by stars (quasars contribute about 1%, see J08). A full discussion of the photometric quality control for the SEGUE scans is detailed in Abazajian et al. (2009). Briefly, median reddening-free colors (Q_{gri} and Q_{riz}) were calculated for each field using magnitudes computed by both the SDSS *photo* (Lupton et al. 2001) and Pan-STARRS *PS* (Magnier et al. 2010) image processing pipelines, and the position and width of the locus of points (corresponding to the stellar main sequence) were computed. Fields within 15° of the Galactic plane had a wider distribution ($\sigma_Q(\text{photo,PS}) \sim 0.035, 0.027$ mag) than fields outside the plane ($\sigma_Q(\text{photo,PS}) \sim 0.021, 0.20$ mag). It can therefore be inferred that (unsurprisingly) the photometric precision in the plane is slightly poorer than that at higher latitudes. A more direct comparison is provided by magnitude differencing the *photo* and *PS* photometry. For stars with $14 < u, g, r, i, z < 20$, the median point-spread function (PSF) magnitude difference was found to be 0.014 mag within the plane versus 0.010 mag outside the plane.

2.2. 2MASS Survey

The 2MASS used two 1.3 m telescopes to survey the entire sky in near-infrared light (Skrutskie et al. 1997). Each telescope had a camera with three 256 × 256 arrays of HgCdTe detectors, and observed simultaneously in the J (1.25 μm), H (1.65 μm), and K_s (2.17 μm , hereafter K) bands. The detectors were sensitive to point sources brighter than about 1 mJy at the 10 σ level, corresponding to limiting magnitudes of 15.8, 15.1, and 14.3, respectively (Vega based; for corrections to AB magnitude scale

²¹ One should note that SDSS terminology “star/galaxy separation” is not an exact term; rather, it refers to separation of unresolved and resolved sources in SDSS imaging data (“stars” include quasars, and “galaxies” can include planetary nebulae, for example).

²² For more details, see <http://www.sdss.org/dr7/>

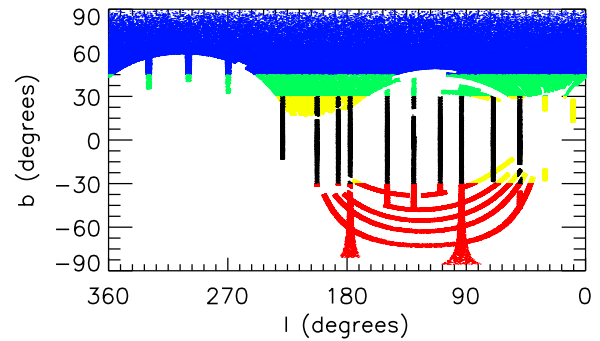


Figure 1. Sky coverage for SDSS Data Release 7, used in this study, in Galactic coordinates. The points show a small random subsample of the full sample of 73 million stars analyzed in this paper. The different colors represent the various data file sets (blue, $b > 45^\circ$; green, $45^\circ > b > 30^\circ$; black, the 10 SEGUE strips; yellow, $|b| < 30^\circ$, stars not in SEGUE strips; and red, $b < -30^\circ$).

(A color version of this figure is available in the online journal.)

see below). Point-source photometry is repeatable to better than 10% precision at these limiting magnitudes, and the astrometric uncertainty for these sources is less than 0".2. The 2MASS catalogs contain positional and photometric information for about 500 million point sources and 2 million extended sources.

2.3. The Main-sample Selection

The main sample is selected from the SDSS Data Release 7 using the following two main criteria:

1. unique unresolved sources: `objc_type=6`, binary processing flags `DEBLENDED_AS_MOVING`, `SATURATED`, `BLENDED`, `BRIGHT`, and `NODEBLEND` must be false, parameter `nCHILD=0` and
2. the *model* r -band magnitudes (uncorrected for extinction) must satisfy $r_{Mod} < 21$.

Detailed discussion of SDSS processing flags, object classification, and various magnitude types can be found in Abazajian et al. (2009). In the current context, *model* magnitudes are essentially the same as PSF magnitudes (optimal flux measures for point sources). These selection criteria yielded 73 million stars (for an SQL query used to select the main sample see Appendix A). The distribution of selected sources on the sky is shown in Figure 1.

For isolated sources, the $r < 21$ condition ensures that photometric errors are typically not larger than 0.05 mag (see Figure 1 in Sesar et al. 2007). For sources with $r < 19$, the errors reach their systematic limit of ~ 0.02 mag. When reported errors are smaller than 0.02 mag, we reset them to 0.02 mag to account for expected photometric zero-point calibration errors (Padmanabhan et al. 2008). The behavior of best-fit χ^2_{pdf} distributions described in Section 3.1.1 justifies the reset of errors. Errors can be much larger for sources in complex environments, and sometimes reported errors are unreliable (e.g., when sources are closer than 3", the photometric errors are overestimated, see Figure 14 in Sesar et al. 2008). If the cataloged photometric error is larger than 0.5 mag in the *griz* bands, or larger than 1.5 mag in the u band, that data point is not used in the analysis (formally, we reset the magnitudes to 999.9 and their errors to 9999.9 in publicly available files, see Appendix B).

2.4. SDSS–2MASS Subsample

Following Covey et al. (2007), acceptable 2MASS sources must have 2MASS quality flags `rd_flag == 222`, `bl_flag ==`

111, and $cc_flag == 0$, and selected 2MASS sources are positionally matched to SDSS sources with a distance cutoff of $1''.5$. With this matching radius, the fractions of multiple matches and spurious associations are below 0.1% at galactic latitudes $|b| > 20^\circ$. The highest false association rate of 0.5%–1% is expected around $b \sim 0^\circ$, though the exact latitude varies by a few degrees due to extinction variations; for details see Finlator et al. (2000). The combined SDSS–2MASS catalog contains ~ 23 million sources. The wavelength coverage of the SDSS and 2MASS bandpasses is shown in Figure 3 in Finlator et al. (2000). The distributions of SDSS–2MASS sources in various color–color and color–magnitude diagrams are discussed in detail by Finlator et al. (2000) and Covey et al. (2007). We emphasize that practically all sources in an SDSS–2MASS point-source sample defined by a K -band flux limit are sufficiently bright to be detected in all other SDSS and 2MASS bands. For orientation, main-sequence stars selected by the condition $K < 14.3$ are closer than approximately 1–2 kpc.

Similarly to the treatment of SDSS photometry, for stars with reported errors in the J , H , and K bands greater than 0.5 mag, we reset magnitudes and errors to 999.9 and 9999.9, respectively. We also reset photometric errors to 0.02 mag when reported errors are below this limit (systematic errors in 2MASS photometry are 0.02 mag; Skrutskie et al. 1997). The Vega-based 2MASS photometry is translated to SDSS-like AB system following Finlator et al. (2000):

$$\begin{aligned} J_{AB} &= J_{2MASS} + 0.89 \\ H_{AB} &= H_{2MASS} + 1.37 \\ K_{AB} &= K_{2MASS} + 1.84. \end{aligned} \quad (1)$$

Note that these corrections have no impact on fitting and results (because the same corrections are applied to models and observations and thus cancel, see below), but are convenient when visualizing SEDs.

2.5. Model Assumptions and Fitting Procedures

There are two empirical results that form the basis of our method. First, the stellar locus in the multi-dimensional color space spanned by SDSS and 2MASS colors is nearly one dimensional (because for most stars the effective temperature has much more effect on colors than other physical parameters, such as age and metallicity²³). The locus position reflects basic stellar physics and is so well defined that it has been used to test the quality of SDSS photometry (Ivezić et al. 2004), as well as to calibrate new photometric data (High et al. 2009).

Second, the *shape* of the dust extinction curve can be described as a one-parameter family, usually parameterized by $R_V = A_V/E(B - V)$ (Cardelli et al. 1989; O’Donnell 1994; Fitzpatrick 1999; Fitzpatrick & Massa 2009). Using this parameterization, extinction in an arbitrary photometric bandpass λ (here λ is a label for an arbitrary photometric bandpass, such as u , g , etc.) is equal to

$$A_\lambda = C_\lambda(R_V) A_r, \quad (2)$$

²³ Gravity has a very minor influence on photometry in SDSS system, as testified by the fact that it is nearly impossible to reliably separate red giants from dwarfs using SDSS photometric data (Helmi et al. 2003). Blue horizontal branch stars are easily separated from main-sequence stars using the $g - r$ color and thus can be easily treated as a special case. Metallicity has a limited impact: the only relevant effect for this study is the change of the $u - g$ color for blue turnoff stars with halo metallicity (108). Since these stars are below the flux limit imposed by the required 2MASS detection (Finlator et al. 2000), the impact of gravity and metallicity effects on results is essentially negligible.

where A_r is extinction in the SDSS r band, and $C_\lambda(R_V)$ describes the shape of the extinction curve.²⁴ Hence, the observed colors can be fit using only three free parameters: the position along the locus, R_V , and A_r (Equation (2) is not the only way to “close” the system of equations; for a detailed discussion see Appendix B). Some caveats to this statement, such as the fact that not all unresolved sources are found along the locus (e.g., quasars and unresolved binary stars), and that even for fixed dust properties A_r and A_λ depend on the source SED, are discussed in quantitative detail further below. We note that it is not mandatory to adopt an extinction curve parameterization given by Equation (2). For example, we could simply adopt the A_λ values determined for high Galactic latitude regions by Schlafly et al. (2010). However, large dust extinction observed at low Galactic latitudes offers a possibility to constrain the shape of the dust extinction curve, and Equation (2) provides a convenient one-parameter description that works well in practice (but see also Fitzpatrick & Massa 2009 for a different functional parameterization with two free parameters).

A similar method was recently proposed by Bailer-Jones (2011), where a strong prior is obtained from measured (trigonometric) distances and a requirement that stars must be consistent with stellar evolutionary track in the Hertzsprung–Russell diagram (as opposed to our constraint that stellar colors must be consistent with the stellar color locus). Such a prior has the advantage of being able to easily distinguish giant stars from main-sequence stars. Unfortunately, trigonometric distances are not available for the vast majority of stars in our sample.

2.5.1. Fitting Details

The best-fit empirical stellar template from a library described in Section 2.6 and the dust extinction according to a $C_\lambda(R_V)$ parameterization described in Section 2.7 are found by minimizing χ_{pdf}^2 defined as

$$\chi_{\text{pdf}}^2 = \frac{1}{N - k} \sum_{i=1}^N \left(\frac{c_i^{\text{obs}} - c_i^{\text{mod}}}{\sigma_i} \right)^2, \quad (3)$$

where c_i^{obs} are N observed adjacent (e.g., $u - g$, $g - r$, etc.) colors ($N = 4$ for only-SDSS data set and $N = 7$ for SDSS–2MASS data set). The color error σ_i is computed by adding photometric errors in quadrature. The number of fitted parameters is $k = 3$ for all parameters, and $k = 2$ when a fixed value $R_V = 3.1$ is assumed (see below).

The model colors are constructed using extinction-corrected magnitudes

$$m_\lambda^{\text{corr}} = m_\lambda^{\text{obs}} - A_\lambda, \quad (4)$$

with $\lambda = (ugriz[JHK])$, resulting in

$$c^{\text{mod}} = c^{\text{lib}}(t) + [C_{\lambda 2}(R_V) - C_{\lambda 1}(R_V)] A_r. \quad (5)$$

Here $\lambda 1$ and $\lambda 2$ correspond to two adjacent bandpasses which define colors c^{mod} and c^{lib} . Hence, by minimizing χ_{pdf}^2 , we obtain the best-fit values for three free parameters: R_V , A_r , and the stellar template library index, t (intrinsic stellar color or position along the locus). Once these parameters are determined, the overall flux normalization is determined by minimizing χ_{pdf}^2 for the fixed best-fit model.

²⁴ The often used parameterization of dust extinction curve, $k(\lambda - V) = E(\lambda - V)/E(B - V)$, is related to C_λ via $k(\lambda - V) = R_V (C_\lambda A_r / A_V - 1)$; Schlafly & Finkbeiner (2010) give $A_V / A_r = 1.200$.

We minimize χ_{pdf}^2 by a brute force method. All 228 library SEDs (see Section 2.6) are tried, with dust extinction values in the range $0 \leq A_r \leq 10$ with 0.02 mag wide steps. This is not a very efficient method, but the runtime on a multi-processor machine was nevertheless much shorter, in both human and machine time, than post-fitting analysis of the results.

We investigate the impact of R_V by producing two sets of best-fit t and A_r . First, we fixed $R_V = 3.1$, and then allow R_V to vary in the range 1–8, with 0.1 wide steps. The results for the two cases are compared and analyzed in the next section.

The errors, σ_i , are computed from photometric errors quoted in catalogs, with a floor of 0.02 mag added in quadrature to account for plausible systematic errors (such as calibration uncertainties), as well as for the finite locus width. In principle, σ_i could be varied with the trial library SED to account for the varying width of the stellar locus. We have not implemented this feature because it does not dominate the systematic errors.

For a given R_V value (whether constant or a grid value in the free R_V case), once the minimum χ^2 , χ_{min}^2 , is located, an ellipse is fit to the section of the χ^2 surface defined by $\chi^2 < \chi_{\text{min}}^2 + 6.17$ (i.e., within 2σ deviation for 2 degrees of freedom):

$$\chi^2(t, A_r | R_V) = a(t - t^*)^2 + b(t - t^*)(A_r - A_r^*) + c(A_r - A_r^*)^2, \quad (6)$$

where t is the template index, and t^* and A_r^* are the best-fit values corresponding to χ_{min}^2 . Using the best-fit parameters a , b and c , the (marginalized) template and A_r errors can be computed from

$$\sigma_t = \left(a - \frac{b^2}{4c} \right)^{-\frac{1}{2}} \quad (7)$$

$$\sigma_{A_r} = \left(c - \frac{b^2}{4a} \right)^{-\frac{1}{2}}. \quad (8)$$

Note that the b coefficient controls the covariance between t^* and A_r^* . The χ^2 surface around the best-fit t/A_r combination is described well by an ellipsoid, although this error ellipse approximation breaks down far from the best fit. The χ^2 surface for stars with $\chi_{\text{min}}^2 > 200$ is not fit with an ellipse and such stars, contributing less than 2% of the entire sample, are instead marked as bad fits.

2.6. The Covey et al. Stellar SED Library

Covey et al. (2007) quantified the main stellar locus in the *ugrizJHK* photometric system using a sample of $\sim 600,000$ point sources detected by SDSS and 2MASS. They tabulated the locus position and width as a function of the $g-i$ color, for 228 $g-i$ values in the range $-0.25 < g-i < 4.50$. We adopt this locus parameterization as our empirical SED library (a set of templates). Strictly speaking, this is not an exhaustive SED library that includes all possible combinations of effective temperature, metallicity, and gravity, but rather a parameterization of the mean locus and its width in the multi-dimensional SDSS–2MASS color space. An alternative approach would be to use stellar atmosphere models (such as the Kurucz library) to generate SEDs, but in this case there would be no guarantee of agreement with the actual observed SEDs (Kurucz model SEDs agree with the SDSS data at the level of ~ 0.03 mag or better; for example, see Figure 23 in Ivezić et al. 2007).

We note that Covey et al. (2007) used the SFD map to correct SDSS and 2MASS photometry for interstellar dust extinction.

Because they only studied high galactic latitude regions where typically $A_r < 0.1$, errors in derived locus parameterization due to errors in the SFD map are at most 0.01 mag, and thus smaller or at most comparable to photometric calibration errors.

This $g-i$ parameterization reflects the fact that the stellar effective temperature, which by and large controls the $g-i$ color, is more important than other physical parameters, such as age (gravity) and metallicity, in determining the overall SED shape (for a related discussion and principal component analysis of SDSS stellar spectra see McGurk et al. 2010). The adopted $g-i$ range includes the overwhelming majority of all unresolved SDSS sources, and approximately corresponds to MK spectral types from early A to late M. Due to 2MASS flux limits, the stellar sample analyzed by Covey et al. (2007) does not include faint blue stars (those with $r \gtrsim 16$ for $g-r < 0.6$; see Figure 4 in Finlator et al. 2000). Consequently, the Covey et al. (2007) locus corresponds to predominantly metal-rich main-sequence stars ($[\text{Fe}/\text{H}] > -1$) because low-metallicity halo stars detected by SDSS are predominantly faint and blue (see Figure 3 in I08). According to Galfast model (J08), stars detected in SEGUE stripes are dominated by metal-rich main-sequence stars, although we note that the fraction of red giant stars in SEGUE is expected to be much larger than observed by SDSS at high Galactic latitudes ($\sim 20\%$ versus $\sim 5\%$).

The adopted template library cannot provide a good fit for SEDs of unresolved pairs of white and red dwarfs (Smolčić et al. 2004), hot white dwarfs (Eisenstein et al. 2006), and quasars (Richards et al. 2001), whose SEDs can differ from the adopted library by many tenths of a magnitude. Systematic photometric discrepancies at the level of a few hundredths of a magnitude are also expected for K and M giants, especially in the u band (Helmi et al. 2003). Similar u -band discrepancies are expected for metal-poor main-sequence stars (I08). Nevertheless, all these populations together never contribute more than $\sim 20\%$ of the full sample (Finlator et al. 2000; Jurić et al. 2008), and in most cases can be recognized by their large values of χ_{min}^2 . At least in principle, additional libraries appropriate for those other populations can be used a posteriori to fit the observed SEDs of sources that have large χ_{min}^2 when using SEDs of main-sequence stars. This additional analysis has not been attempted here, though our results represent the first necessary step: finding sources with large χ_{min}^2 .

2.7. Parameterization of Dust Properties

To implement the fitting method described in Section 2.5, the shape of the extinction curve (C_λ , see Equation (2)) must be characterized. C_λ in the SDSS bands was initially computed (prior to the beginning of the survey, to enable spectroscopic targeting) using the standard parameterization of the extinction curve (Cardelli et al. 1989; O’Donnell 1994) with $R_V = 3.1$. The resulting values ($C_\lambda = 1.87, 1.38, 0.76, 0.54$, with $\lambda = u, g, i, z$) are commonly adopted to compute the extinction in the SDSS bands, together with A_r given by the SFD map via $A_r = 2.75E(B-V)$.

A preliminary analysis of the position of the stellar locus in the SDSS–2MASS color space suggested that the above C_λ values need to be slightly adjusted (Meyer et al. 2005). Further support for this conclusion was recently presented by Sch2010. Here, we revisit the Meyer et al. analysis using an improved SDSS photometric catalog from the so-called stripe 82 region²⁵ (Ivezić

²⁵ Available from <http://www.astro.washington.edu/users/ivezic/sdss/catalogs/stripe82.html>

et al. 2007). SDSS photometry in this catalog is about twice as accurate as typical SDSS photometry due to averaging of many observations and various corrections for systematic errors. The SDSS–2MASS subset of that catalog includes 102,794 sources unresolved by SDSS (out of about a million in the full sample), which also have a 2MASS source with $K < 14.3$ within $1''.5$. The results of our analysis provide an updated set of C_λ coefficients, which are then used to select a dust extinction parameterization for generating the required $C_\lambda(R_V)$ dependence. Similarly to a recent analysis by Sch2010, we find that the O’Donnell (1994) parameterization can be rejected, and adopt the CCM dust extinction law (Cardelli et al. 1989).

2.7.1. Determination of the Locus Shifts

The interstellar extinction reddens the stellar colors and shifts the position of the *whole* stellar locus at high Galactic latitudes, where practically all stars are located behind the dust screen. At high Galactic latitudes, distances to an overwhelming majority of stars are larger ($\gtrsim 100$ pc) than the characteristic scale height of the interstellar dust layer (~ 70 pc; J08). Both the amount of reddening and its wavelength dependence can be determined by measuring the locus position and comparing it to the locus position corresponding to a dust-free case. The latter can be determined in regions with very small extinction ($A_r \sim 0.05$) where errors in the SFD extinction map as large as 20% would still be negligible.

We measure the locus position in the seven-dimensional SDSS–2MASS color space using an extended version of the “principal color” method developed by Ivezić et al. (2004) to track the quality of SDSS photometric calibration. Briefly, two principal axes, P_1 and P_2 , are defined along the locus and perpendicular to the locus, for the appropriately chosen (blue) parts of the locus. We utilize six independent two-dimensional (2D) projections spanned by the $r - K$ and $\lambda - r$ colors, where $\lambda = u, g, i, z, J, \text{ and } H$ (see Figure 2). Since the extinction in the 2MASS K band is small and fairly template and R_V independent ($A_K/A_r = 0.133$ for $R_V = 3.1$, with only a $\sim 10\%$ variation over the range of plausible R_V and dust parameterizations, as discussed further below), the locus shifts in the $r - K$ direction provide robust constraints for A_r . For example, a 10% uncertainty in the A_K/A_r ratio results in only 1.5% uncertainty in A_r determined from a given $A_r - A_K$ value. We determine these shifts iteratively, starting with A_r given by the SFD map, and adjusting A_r until the observed and corrected $r - K$ color distributions agree in a maximum likelihood sense. This determination of A_r is very similar to the “blue tip” method introduced in Sch2010. The two main differences are due to the addition of 2MASS data. First, the low-metallicity faint blue stars are not included in the sample analyzed here. Such stars could systematically influence the locus morphology and reddening estimates based on the “blue tip” method; nevertheless, our results are in good agreement with the Schlafly et al. results, as discussed below. Second, the availability of the K magnitudes enables a robust and straightforward determination of A_r , *without any consideration of the SFD map*. For a detailed discussion of these issues, see Appendix C.

After A_r is estimated from the $r - K$ color offsets, the locus offsets in the $\lambda - r$ directions then provide constraints for the extinction wavelength dependence, C_λ . We measure these offsets using principal colors, P_1 and P_2 , with P_1 parallel to the blue part of the stellar locus and P_2 perpendicular to it (see the top left panel in Figure 2 for illustration of the principal axes

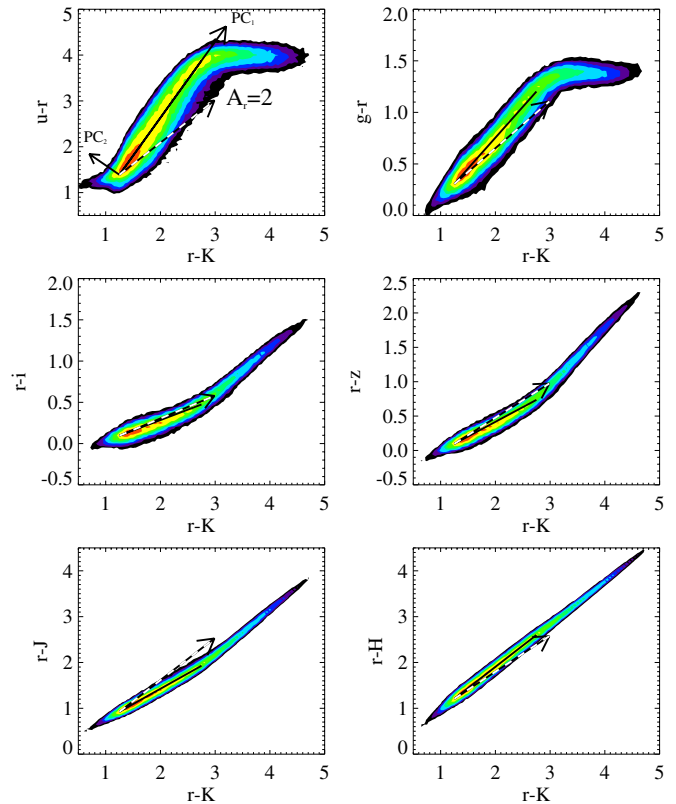


Figure 2. Distribution of unresolved SDSS sources with 2MASS detections in the $\lambda - r$ vs. $r - K$ color-color diagrams, with $\lambda = u, g, i, z, J, \text{ and } H$. The source density is shown as color-coded maps, and it increases from black to green to red. The two arrows marked PC_1 and PC_2 in the top left panel illustrate the “principal color” axes discussed in the text and used to track the locus shifts due to interstellar dust reddening. The dashed vector in each panel shows the reddening vector for $A_r = 2$ and standard $R_V = 3.1$ dust (Cardelli et al. 1989). (A color version of this figure is available in the online journal.)

and for a comparison of the locus orientation with the direction of the standard reddening vectors). The blue part of the stellar locus at the probed faint magnitudes ($14 < r < 17$) includes mostly thick disk stars with distances of the order 1 kpc or larger, which are thus beyond all the dust.

We measure the position of the blue part of the locus in each $\lambda - r$ versus $r - K$ diagram using stars with $1.5 < r - K < 2.5$ (approximately; the range is enforced using the $P_1(\lambda)$ color). The blue part of the locus is parameterized as

$$P_1(\lambda) = \cos(\theta_\lambda)(r - K) + \sin(\theta_\lambda)(\lambda - r) + c_1(\lambda) \quad (9)$$

and

$$P_2(\lambda) = -\sin(\theta_\lambda)(r - K) + \cos(\theta_\lambda)(\lambda - r) + c_2(\lambda). \quad (10)$$

The best-fit angle θ_λ found using stripe 82 data set is equal to ($61^\circ 85', 33^\circ 07', 14^\circ 57', 23^\circ 47', 34^\circ 04', 43^\circ 35'$) for $\lambda = (u, g, i, z, J, H)$. The values of c_1 and c_2 are completely arbitrary; we set $c_1(\lambda) = 0$ and determine $c_2(\lambda)$ by requiring that the median value of $P_2(\lambda)$ color is 0 ($c_2 = 0.463, 0.434, 0.236, 0.424, -0.048, -0.019$ for u, g, i, z, J, H , respectively). Given the locus shift $\Delta P_2(\lambda)$ and A_r determined from the $r - K$ color offset (or alternatively from the ΔP_1 offsets), the corresponding A_λ can be determined from

$$C_\lambda \equiv \frac{A_\lambda}{A_r} = 1 + \tan(\theta_\lambda) \left(1 - \frac{A_K}{A_r} \right) + \frac{1}{\cos(\theta_\lambda)} \frac{\Delta P_2(\lambda)}{A_r}. \quad (11)$$

Table 1
Observational Constraints and Model Values for the Extinction Curve,
 $C_\lambda \equiv A_\lambda/A_r$

Region	u	g	i	z	J	H	K_s
S82	1.810	1.400	0.759	0.561	0.317	0.200	0.132
North	1.750	1.389	0.750	0.537	0.297	0.180	0.132
CCM	1.814	1.394	0.764	0.552	0.327	0.205	0.132
F99	1.795	1.415	0.748	0.554	0.308	0.194	0.132
OD	1.813	1.406	0.783	0.562	0.325	0.205	0.132

Notes. The first two rows list observational constraints for the shape of the extinction curve, $C_\lambda \equiv A_\lambda/A_r$. The value of C_λ in the K band was assumed to be 0.132. The first row corresponds to the so-called SDSS Stripe 82 region (defined by $300^\circ < \text{R.A.} < 60^\circ$ and $|\text{decl.}| < 1^\circ:27$) and the second row to a northern region defined by $30^\circ < b < 45^\circ$ and $0^\circ < l < 10^\circ$. The last three rows list model predictions computed for an F star spectrum and the best-fit value of R_V (CCM: Cardelli et al. 1989, $R_V = 3.01$; F99: Fitzpatrick 1999, $R_V = 3.30$; OD: O’Donnell 1994, $R_V = 3.05$).

Assuming a constant A_K/A_r ratio, it is straightforward to compute the error of this estimate.

The locus position must be measured over a sky area where the amount of dust and dust properties can be assumed constant. The smaller the area, the more robust is this assumption. However, the chosen area cannot be arbitrarily small because the error in the locus position, and thus the C_λ error, is inversely proportional to the square root of the star counts. Within the analyzed stripe 82 region, the counts of SDSS–2MASS stars in the blue part of the stellar locus never drop below 70 stars deg^{-2} . We bin the data using 4° wide bins of R.A. (with $|\text{decl.}| < 1.27 \text{ deg.}$, an area of $\sim 10 \text{ deg}^2 \text{ bin}^{-1}$), which guarantees that random errors in A_λ never exceed $\sim 2\%$ (even for the u band and a factor of few smaller in other bands). In addition, we consider four larger regions: the high-latitude northern sky with $b > 45^\circ$, split into $l < 180^\circ$ and $l > 180^\circ$ subregions, a northern strip defined by $30^\circ < b < 45^\circ$, and a southern strip defined by $-45^\circ < b < -30^\circ$ (for these regions, we use SDSS DR7 photometry).

2.7.2. Interpretation of the Locus Shifts and Adopted Dust Extinction Parameterization

We find that the variations in the shape of the extinction curve across the 28 R.A. bins from Stripe 82 region are consistent within measurement errors. The values of C_λ obtained for the whole Stripe 82 region are listed in the first row in Table 1. Practically identical coefficients are obtained for the southern strip defined by $-45^\circ < b < -30^\circ$. The extinction curve values for the northern sky are consistent with the southern sky, and we recommend the entries listed in the first row in Table 1 for correcting SDSS and 2MASS photometry for interstellar dust extinction. One of the largest discrepancies is detected in a region from the northern strip defined by $30^\circ < b < 45^\circ$ and $0^\circ < l < 10^\circ$; and these values are listed in the second row in Table 1. Nevertheless, the north versus south differences are not large, and, using models described below, correspond to an R_V variation of about 0.1.

Much larger north versus south differences are detected when comparing the best-fit A_r values to the SFD map values. The accuracy of the A_r determined here is about 3%–10%, depending on the amount of dust. We find that the SFD A_r values are consistently larger by about 20% than our values determined across the southern hemisphere. Interestingly, no such discrepancy is detected across the northern sky, to within

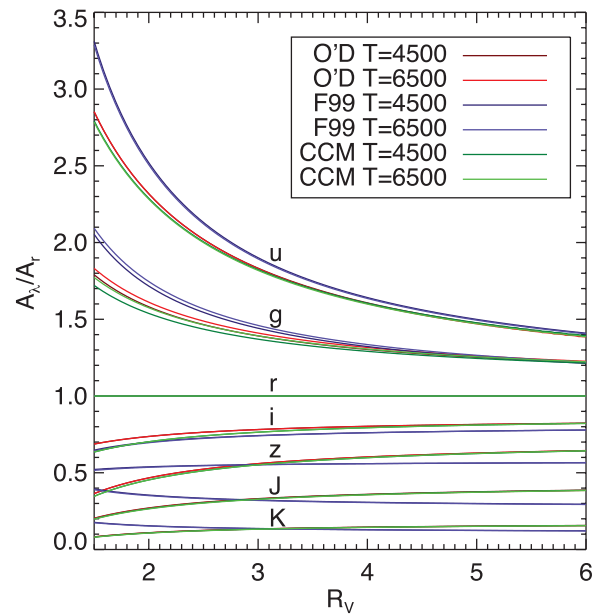


Figure 3. Model predictions for the extinction curve shape ($C_\lambda = A_\lambda/A_r$) as a function of R_V for three different parameterizations: O’D (O’Donnell 1994), F99 (Fitzpatrick 1999), and CCM (Cardelli et al. 1989), evaluated for stars with two different effective temperatures (as listed in the legend, in Kelvin). The figure shows C_λ for $\lambda = (u, g, r, i, z, J, K)$ (top to bottom, respectively). As expected, most of the sensitivity to R_V comes from the blue bands (u and g). (A color version of this figure is available in the online journal.)

measurement errors of $\sim 5\%$. In several isolated regions, the discrepancies are much larger. For example, in a region defined by $-45^\circ < b < -30^\circ$ and $157^\circ < l < 160^\circ$, the SFD values appear overestimated by 50% (the median value of A_r in that region given by the SFD map is 1.3). These results are similar to those presented in Sch2010, where the spatial variation of errors in the SFD map and their possible causes are discussed in more detail. The conclusion that the SFD A_r values are consistently overestimated in the southern hemisphere is also consistent with the results based on galaxy count analysis by Yasuda et al. (2007), which is essentially an independent method.

We adopt the C_λ values determined for the Stripe 82 region (the first row in Table 1) to select a dust extinction law used in subsequent fitting of SEGUE data. Using the same assumptions and code as Sch2010, we compute dust extinction curves for three popular parameterizations,²⁶ and for three different input stellar SEDs. As can be seen in Figure 3, the differences between the dust extinction parameterizations are much larger than the impact of different underlying spectra.

A comparison of the observational constraints and model predictions is summarized in Figure 4. Following Sch2010, we use ratios of the reddening values for this comparison. The differences in the extinction curve shape between the southern and northern sky determined here are similar to their differences from the Sch2010 results, and are consistent with estimated measurement uncertainties. The O’Donnell (1994) parameterization predicts unacceptable values of the $(A_r - A_i)/(A_i - A_z)$ ratio for all values of R_V . The other two parameterizations are in fair agreement with the data. Due to a slight offset of the Sch2010 measurements, they argued that the CCM parameterization (Cardelli et al. 1989) is also

²⁶ Strictly speaking, these are not dust grain models but rather analytic parameterizations of measured extinction curves.

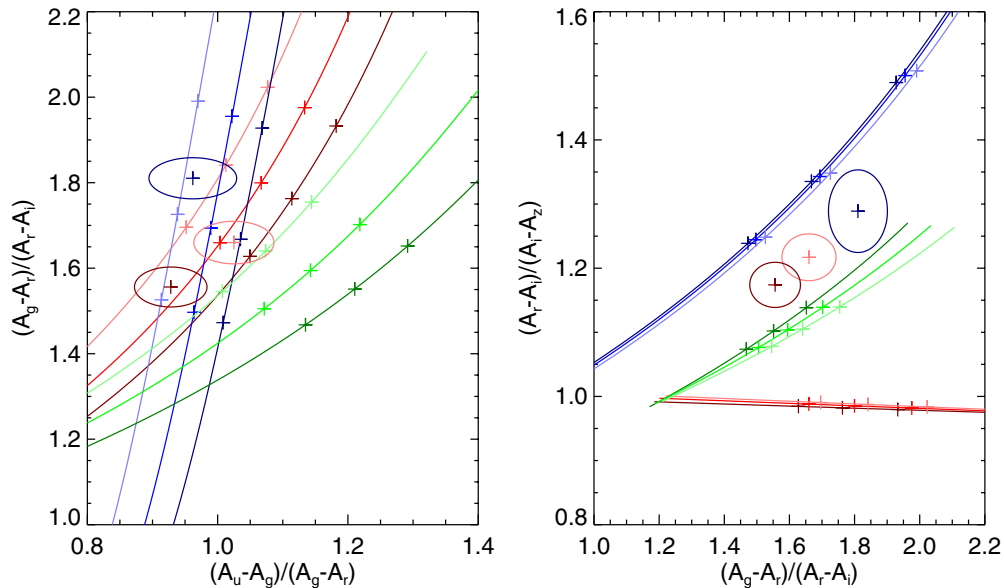


Figure 4. Comparison of the constraints on the extinction curve shape (the three plus symbols, with approximate 1σ uncertainty limits shown as ellipses) and three model predictions (see Figure 3 for legend, the additional line for each template corresponds to a star with an effective temperature of 5500 K; the three crosses along the curves correspond to $R_V = 2.6, 3.1,$ and 3.6). The pink symbol corresponds to the Stripe 82 region (southern Galactic hemisphere), the brown symbol to the northern Galactic hemisphere, and the blue symbol is the constraint from the Schlafly et al. (2010) analysis. The blue (Fitzpatrick 1999) and green (Cardelli et al. 1989) parameterizations are in fair agreement with the data (1σ – 2σ discrepancies, where σ stands for random errors and does not include various systematic errors), while the red parameterization (O’Donnell 1994) predicts unacceptable values of the $(A_r - A_i)/(A_i - A_z)$ ratio for all values of R_V (see also Figures 5 and 6). (A color version of this figure is available in the online journal.)

unsatisfactory, although the discrepancy was not as large as in the case of the O’Donnell (1994) reddening law.

Although none of the parameterizations shows a perfect agreement with the data, the discrepancies are not large. To further illustrate the constraints from different bands, we determine the best-fit R_V and its uncertainty in each band using the CCM parameterization. If a parameterization is acceptable, the constraints from different bands must be statistically consistent. As shown in Figure 5, this is indeed the case, and we obtain the best-fit $R_V = 3.01 \pm 0.05$. The systematic error of this estimate, implied by the variation of the extinction curve shape across the analyzed regions, is about 0.1. The corresponding figure for the F99 (Fitzpatrick 1999) reddening law is similar, with the best-fit $R_V = 3.30 \pm 0.1$, while for the O’Donnell (1994) parameterization, $R_V = 3.05 \pm 0.05$. However, for the latter, the predicted extinction in the i band is inconsistent with the rest of the bands at about 2σ level (see Figure 6). This inconsistency is the main reason for rejecting the O’Donnell parameterization both here and by Sch2010. A comparison between the CCM and O’Donnell laws is further illustrated in Figure 7; it appears that polynomial fitting adopted by both CCM and O’Donnell (to the 7th and the 8th order, respectively) has caused wiggles whose integral over SDSS bandpasses is the largest in the i band. The predicted values of the extinction curve for all three parameterization, using their individual best-fit values for R_V , are listed in Table 1.

For the rest of our analysis, we generate $C_\lambda(R_V)$ values using the CCM law and an F star SED (7000 K). The adopted curves are shown in Figure 8, and a few representative values are listed in Table 2. For comparison, we also list C_λ values suggested by Sch2010, and the values computed using extinction curve parameterization proposed by Fitzpatrick & Massa (2009).

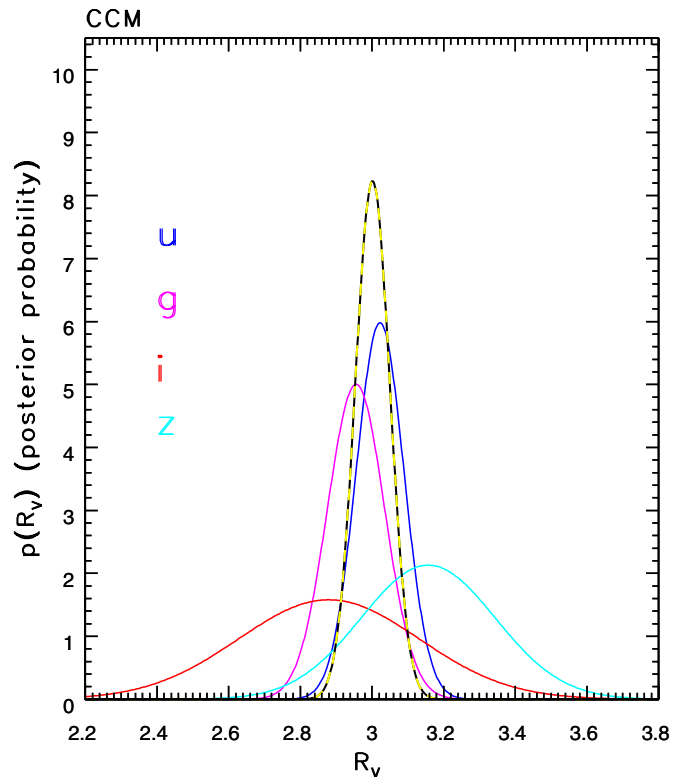


Figure 5. Constraints on R_V based on the CCM (Cardelli et al. 1989) dust reddening law. Only the SDSS bands, which provide the strongest constraints on R_V , are shown (see the legend). The dashed line shows the overall constraint on R_V (posterior probability distribution for a flat prior), with the best-fit value of $R_V = 3.01 \pm 0.05$.

(A color version of this figure is available in the online journal.)

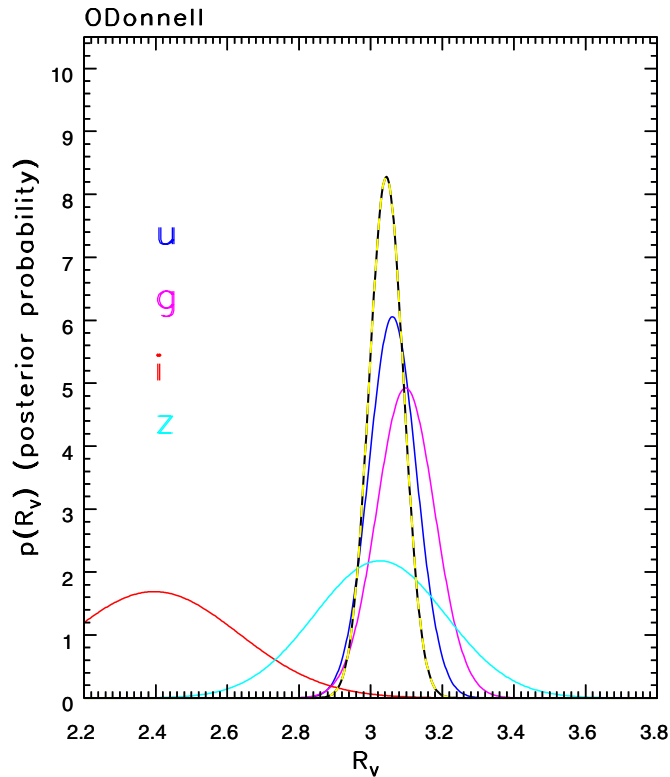


Figure 6. Analogous to Figure 5, except that O’Donnell (1994) dust reddening law is used. The predicted extinction in the i band is inconsistent with constraints from other bands.

(A color version of this figure is available in the online journal.)

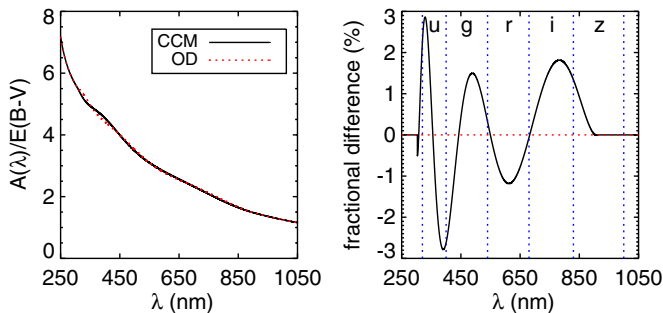


Figure 7. Left panel shows the CCM (black, solid line) and the O’Donnell (red, dashed line) dust reddening laws as function of wavelength. The right panel displays the fractional difference between the two dust extinction parameterizations with the SDSS filter transmission regions overlaid (vertical, blue, dashed lines). Given the filter transmission regions, the largest integrated difference is expected in the i band, which is what we observe.

(A color version of this figure is available in the online journal.)

2.8. Illustration of the Method and Fitting Degeneracies

To summarize, we make two basic assumptions when analyzing observed SEDs of low-latitude stars (SEGUE stripes). First, we assume that the median stellar locus in SDSS and 2MASS bandpasses, as quantified by Covey et al. (2007) at high Galactic latitudes, is a good description of stellar colors at all Galactic latitudes. Second, we assume that the normalized dust extinction curve, A_λ/A_r , can be described as a function of single parameter, $R_V = A_V/E(B - V)$. Therefore, for a given set of measured colors, four in SDSS-only case and seven in SDSS–2MASS case, we fit three free parameters: stellar param-

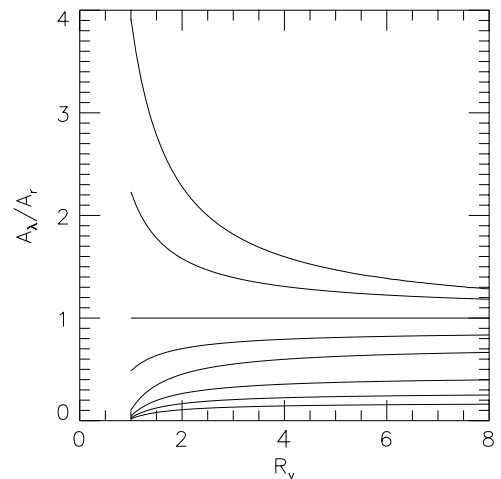


Figure 8. Adopted A_λ/A_r ratio, shown as a function of R_V , for $\lambda = (ugrizJHK)$, from top to bottom ($A_r = 1$). The curves are computed for an F star using the CCM (Cardelli et al. 1989) dust reddening law.

Table 2
Adopted Extinction Coefficients, $C_\lambda(R_V)$

R_V	u	g	i	z	J	H	K_s	Source
2.0	2.280	1.579	0.702	0.453	0.264	0.166	0.107	CCM
2.5	1.998	1.467	0.740	0.513	0.302	0.190	0.122	CCM
3.0	1.817	1.395	0.764	0.552	0.326	0.205	0.132	CCM
3.1	1.788	1.384	0.768	0.558	0.330	0.208	0.134	CCM
3.1	1.855	1.446	0.743	0.553	Sch2010
3.1	1.857	1.439	0.725	0.517	0.250	0.131	0.068	F99
4.0	1.598	1.308	0.793	0.598	0.356	0.224	0.144	CCM
5.0	1.470	1.257	0.810	0.625	0.373	0.234	0.151	CCM

Notes. An illustration of the dependence of the adopted extinction curve, $C_\lambda \equiv A_\lambda/A_r$, on R_V ($C_r = 1$ by definition; see also Figure 8). The second line with $R_V = 3.1$ lists the values suggested by Schlafly & Finkbeiner 2010, and the third line with $R_V = 3.1$ lists the values computed using Equation (5) from Fitzpatrick & Massa 2009 with $\alpha = 2.50$ (constrained by $C_r = 1$), and using $A_V/A_r = 1.20$ and the effective wavelengths from Schlafly & Finkbeiner (2010) for the SDSS bands, and 1.25 μm , 1.65 μm , and 2.17 μm for the 2MASS JHK bands, respectively. Both lines are presented for a comparison with the adopted CCM extinction curve.

eterization (position along the one-dimensional locus), t , dust amount, A_r , and R_V .

When the number of measured colors is small, when the color errors are large, or when the sampled wavelength range is not sufficiently wide, the best-fit solutions can be degenerate. The main reason for this degeneracy is the similarity of the stellar locus orientation and the direction of the dust reddening vector (see Figure 2). This degeneracy is especially strong for stars in the blue part of the locus ($g - i < 1$) and remains even when SDSS photometry is augmented by 2MASS photometry (a photometric band at a wavelength much shorter than the SDSS u band is needed to break this degeneracy).

Figure 9 illustrates an example of degenerate solutions in the $r - i$ versus $g - r$ color-color diagram, and how degeneracies are partially broken when the $i - z$ color is added to the data. Because the direction of the reddening vector in the $i - z$ versus $r - i$ color-color diagram is essentially independent of R_V , the measured $r - i$ and $i - z$ colors provide robust constraints for t and A_r , irrespective of R_V . The addition of the measured $g - r$ color to $r - i$ and $i - z$ colors then constrains R_V .

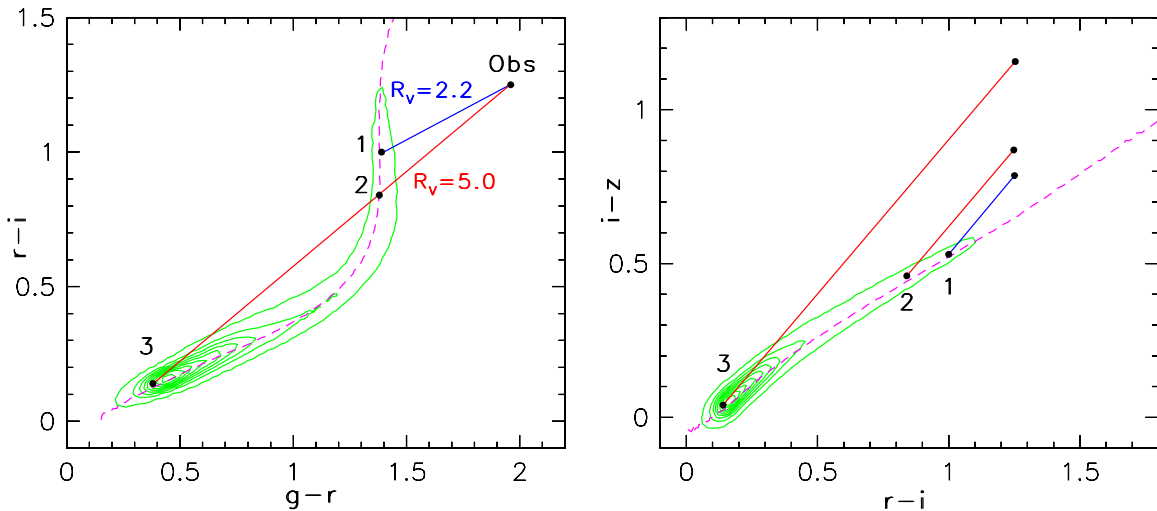


Figure 9. Illustration of the constraints on intrinsic stellar colors, extinction in the r band, A_r , and the ratio of total to selective extinction, R_V . In both diagrams, the linearly spaced contours show the main stellar locus as observed at high Galactic latitudes. The dashed lines mark the median stellar locus from Covey et al. (2007). In the left panel, the dot marked “Obs” represents a hypothetical observation. Depending on the adopted R_V , as marked, different combinations of intrinsic stellar colors (i.e., the position along the stellar locus) and A_r are consistent with the observed $g-r$ and $r-i$ colors. The three solutions marked 1–3 correspond to $(R_V, A_r) = 1:(2.2, 1.0)$, $2:(5.0, 2.2)$, and $3:(5.0, 6.0)$. As shown in the right panel, these degeneracies are broken if the $i-z$ color is also available: the three (R_V, A_r) combinations have different reddened $i-z$ colors which breaks the degeneracy between the intrinsic stellar color and A_r . The degeneracy is broken because the reddening vectors in the right panel are nearly parallel despite very different R_V values.

(A color version of this figure is available in the online journal.)

Since the stellar locus in the $i-z$ and $r-i$ color–color diagram and the reddening vector are not perpendicular, the covariance between the best-fit t and A_r values does not vanish. The addition of other bands, e.g., 2MASS bands to SDSS bands, alleviates this covariance, but not completely (and only slightly for blue stars). We quantify this effect using simulated observations, as described below.

2.9. Tests of the Method

To test the implementation of χ^2 minimization algorithm, and to study the dependence of best-fit parameter uncertainties on photometric errors, the amount of extinction, and the intrinsic stellar color, we first perform relatively simple Monte Carlo simulations and analyze the resulting mock catalog based on realistic stellar and dust distributions, and photometric error behavior.

2.9.1. The Impact of Photometric Errors

In the first test, we study the variation of best-fit parameters with photometric errors, where the latter are generated using Gaussian distribution and four different widths: 0.01, 0.02, 0.04, and 0.08 mag. The dust extinction curve shape is fixed to $R_V = 3.1$, and we only use SDSS photometry. The noiseless “observed” magnitudes for a fiducial star with intrinsic color $g-i = 1.95$ (roughly at the “knee” of the stellar locus in the $r-i$ versus $g-r$ color–color diagram) and $A_r = 1.5$ are convolved with photometric noise generated independently for each band, and the resulting “observed” colors are used in fitting. The errors in best-fit templates and A_r are illustrated in Figures 10 and 11.

The median errors in the best-fit stellar SED, parameterized by the $g-i$ color, are about twice as large as the assumed photometric errors. When photometric errors exceed about 0.05 mag, the best-fit A_r distribution becomes *bimodal*, with the additional mode corresponding to a solution with a bluer star behind more dust. Therefore, even the addition of the red z passband is insufficient to break the stellar color–reddening

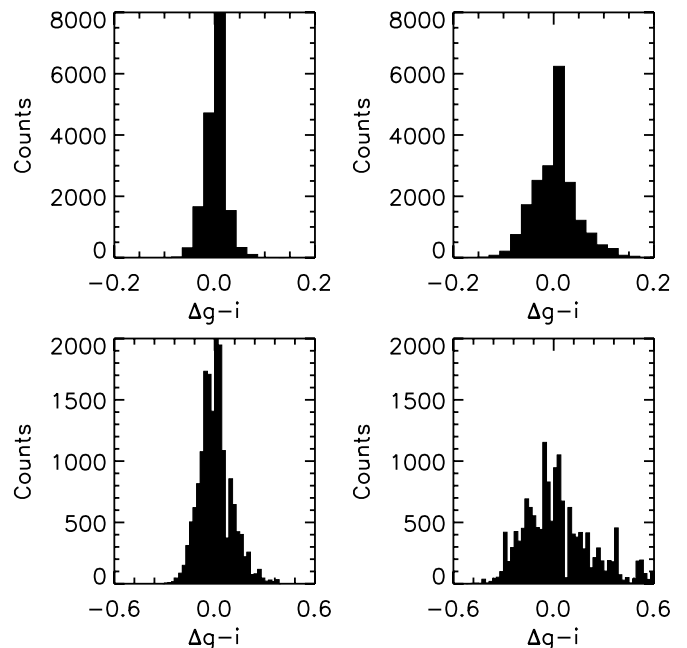


Figure 10. Monte Carlo study of error in best-fit $g-i$ color, determined through parameterization of the stellar locus, as a function of photometric errors, for a fiducial star with $g-i = 1.95$ and $A_r = 1.5$ (the abscissa, $\Delta g-i =$ true fit). The photometric errors are generated from Gaussian distributions with widths equal to 0.01 mag (top left), 0.02 mag (top right), 0.04 mag (bottom left), and 0.08 mag (bottom right). The errors in the best-fit $g-i$ are about twice as large as assumed photometric errors.

degeneracy when the photometry is inaccurate (this conclusion remains true even when 2MASS bands are added). *Our fitting results should thus be trusted only for stars sufficiently bright to have photometric errors smaller than about 0.05 mag in most bands.* With this constraint, the formal best-fit errors are typically within 20% of the true errors.

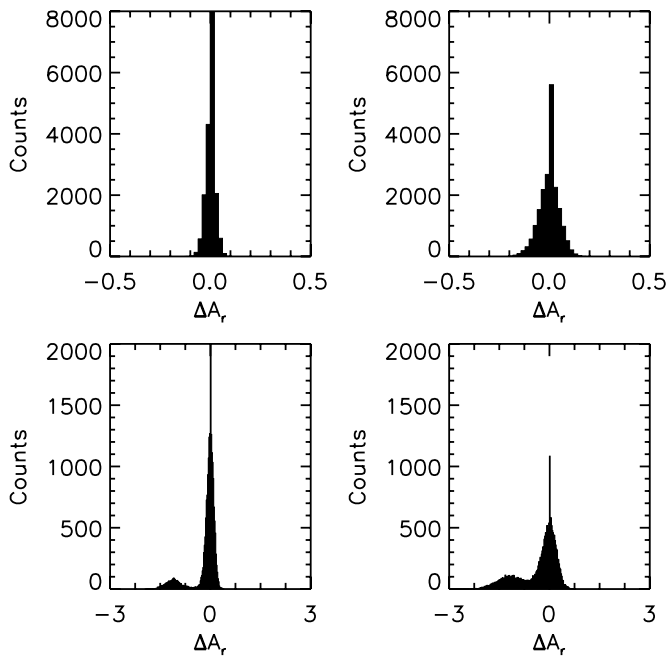


Figure 11. Analogous to Figure 10, except that the errors in the best-fit A_r are shown ($\Delta A_r = \text{true fit}$). Note that for large photometric errors (the bottom two panels), the A_r error distribution becomes bimodal; the additional mode corresponds to a solution with a bluer star with more reddening.

2.9.2. The Reddening versus Intrinsic Stellar Color Degeneracy

In the second test, we have investigated the covariance between the best-fit template and A_r values. Here, again the dust extinction curve shape is fixed to $R_V = 3.1$. Figure 12 shows the χ^2 surfaces for a blue and a red star, and for two values of A_r , when only-SDSS bands are used in fitting and Gaussian noise with $\sigma = 0.02$ mag is assumed for all bands. The best-fit template- A_r covariance is larger for the bluer star, in agreement with the behavior illustrated in Figure 9 (the angle between the reddening vector and the stellar locus is smaller for the blue part of the locus than for the red part). The A_r versus $g - i$ covariance does not strongly depend on assumed A_r . When the 2MASS bands are added, the morphology of the χ^2 surface is essentially unchanged (recall that R_V was fixed in these tests).

These tests show that our implementation of the χ^2 minimization algorithm produces statistically correct results, and that the accuracy of SDSS and 2MASS photometry is sufficient (for most sources) to break degeneracy between the dust reddening and intrinsic stellar color in case of a fixed dust extinction curve ($R_V = 3.1$). Nevertheless, *the best-fit results should be interpreted with caution when photometric errors exceed 0.05 mag, especially for intrinsically blue stars.*

2.9.3. Tests Based on a Realistic Galfast Mock Catalog

To quantify the expected fidelity of our best-fit parameters, including R_V , for a realistic distribution of stellar colors, photometric errors, and dust extinction, we employ a mock catalog produced by the *Galfast* code (M. Jurić et al., in preparation). *Galfast* is based on the Galactic structure model from J08 and includes thin disk, thick disk, and halo components. The stellar populations considered here include main-sequence and post-main-sequence subgiant and giant stars. All other populations, such as binary stars, blue horizontal branch stars, brown dwarfs, white dwarfs, and quasars, are expected to contribute only a few percent of the total source count at low Galactic latitudes rele-

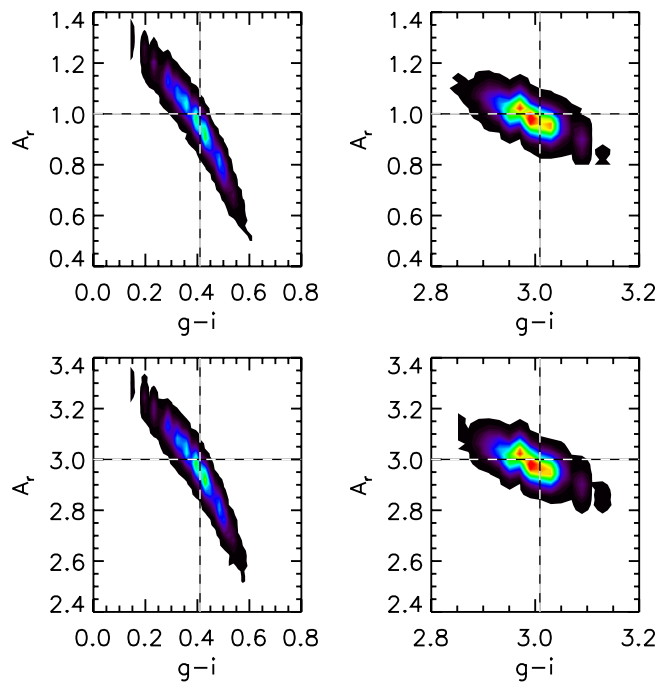


Figure 12. Analysis of the covariance in the best-fit values for A_r and $g - i$ using a simulated data set. The panels show the distributions of the best-fit values for A_r and $g - i$ for two different fiducial stars (left column: a blue star with true $g - i = 0.4$; right column: a red star with true $g - i = 3.0$), and two different extinction values (top panels: $A_r = 1$; bottom panels: $A_r = 3$). Photometric errors in the *ugriz* bands are generated using Gaussian distributions with $\sigma = 0.02$ mag (uncorrelated between different bands). Note that the A_r vs. $g - i$ covariance is larger for the blue star, and does not strongly depend on assumed A_r .

(A color version of this figure is available in the online journal.)

vant here. SDSS and 2MASS photometry is generated using the Covey et al. (2007) SED library (using the $g - i$ color provided by *Galfast*). The photometric errors are modeled using parameterization given by Equation (5) in Ivezić et al. (2008b), and the best-fit values for 5σ limiting depth derived using cataloged errors for SDSS and 2MASS data (for SDSS *ugriz* bands: 21.5, 23.0, 22.8, 22.6, and 20.5, respectively; for 2MASS *JHK* bands: 17.0, 16.0, and 15.5 on Vega scale). The dust extinction along the line of sight to each star is assigned using the three-dimensional dust distribution model of Amôres & Lépine (2005). The shape of the dust extinction curve is fixed to the CCM parameterization values for $R_V = 3.1$. The normalization of the extinction for a given line of sight is determined by requiring a match to the SFD map at a fiducial distance of 100 kpc (that is, a complex dust distribution is retained in two out of three coordinates).

The absolute magnitude and intrinsic color distribution of stars in the simulated low-latitude ($110^\circ < l < 112^\circ$ and $|b| < 5^\circ$) sample is very different from distributions seen with high-latitude samples. The two main differences are much bluer *intrinsic* color distribution, and a much larger fraction of red giants in the low-latitude data set. The origin of these differences is illustrated in the top two panels in Figure 13. As shown in the top left panel, the simulated sample is dominated by stars with intrinsic $g - i < 1.2$, and includes a large fraction of red giants (40% with $M_r < 2$). These giants pass the $r > 14$ selection cut due to large dust extinction ($A_r \sim 3$ mag for giants in the simulated sample). At high Galactic latitudes, most red giants are brighter than SDSS saturation limit $r \sim 14$.

The distributions of modeled stars in the color-magnitude and color-color-magnitude diagrams closely match SDSS and

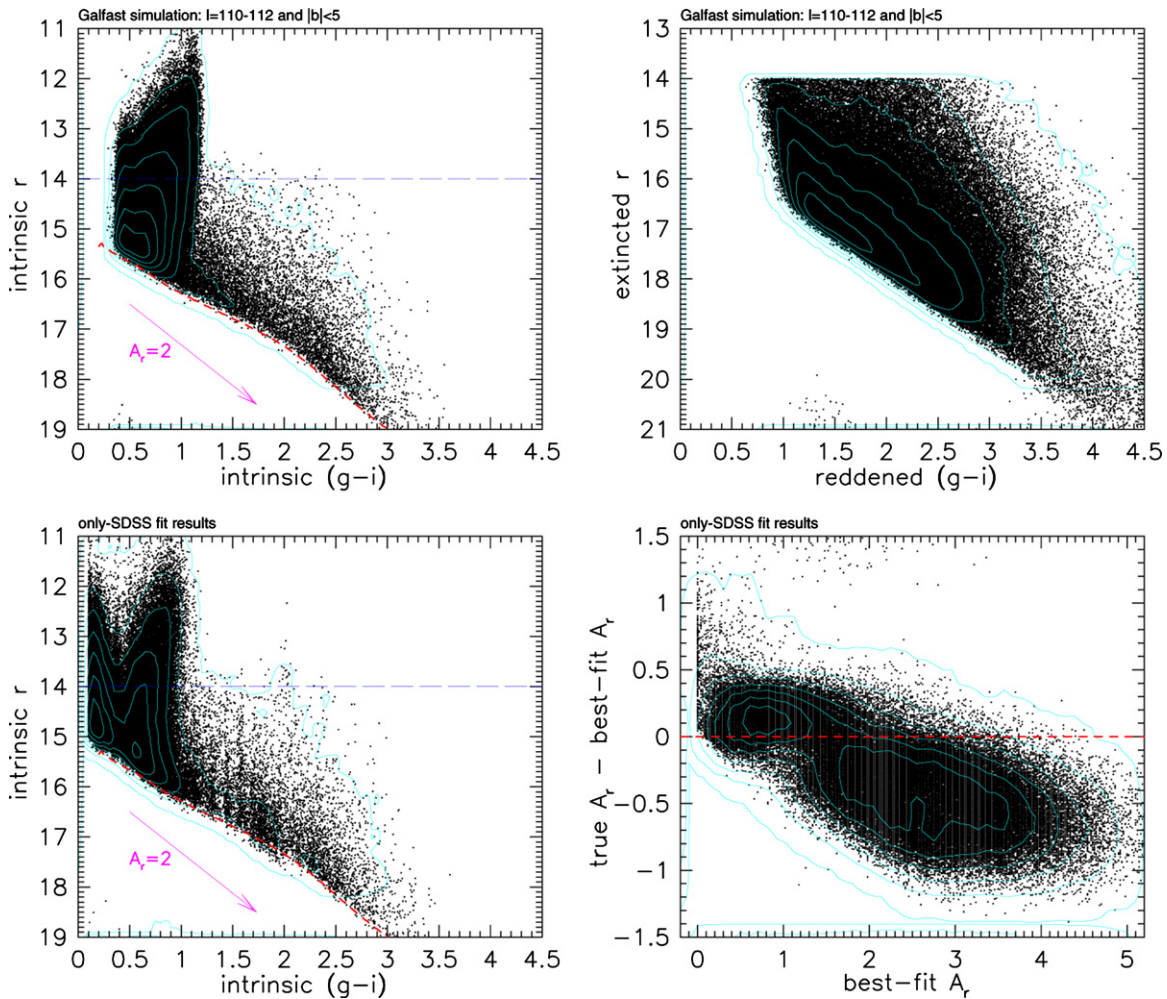


Figure 13. Analysis of a *Galfast* simulated SDSS-2MASS sample from a SEGUE strip ($l \sim 110^\circ$ and $|b| < 5^\circ$). The r vs. $g-i$ color-magnitude diagrams in the top two panels explain why the fraction of giants is much larger than observed at high Galactic latitudes. The same simulated sample, defined by *observed extinguished* magnitude cuts $14 < r < 21$ and $K < 14.3$ (Vega), is shown in both panels. The left panel is constructed using *un-extinguished* magnitudes, and the right panel with “observed” magnitudes (note the offset of the y axis by 2 mag). The horizontal dashed line in the left panel shows the SDSS saturation limit; stars above this line are dominated by red giants (the “plume” toward $g-i \sim 1$). The diagonal dashed line shows the magnitude limit for main-sequence stars with $K < 14.3$ and *no dust extinction*. The reddening arrow corresponds to $A_r = 2$ and $R_V = 3.1$ CCM extinction curve. The bottom left panel is analogous to the top left panel, except that the SDSS-based best-fit values for $g-i$ and A_r are used. The bottom right panel shows the difference between the input value of A_r and the best-fit values, as a function of the latter. The dashed line is added to guide the eye. The root-mean-square scatter for the A_r difference (rms for the y axis) is 0.33 mag, and the bias for large A_r is about 15% (an overestimate of A_r due to color- A_r degeneracy, see the text).

(A color version of this figure is available in the online journal.)

2MASS data (for an illustration see Figure 14). The much redder observed colors of stars in SEGUE stripes, compared to high-latitude sky, are reproduced with high fidelity. For example, the median $g-i$ color for the SEGUE $l \sim 110^\circ$ stripe moves from 1.0 at $r \sim 16$ to 1.7 at $r \sim 21$; only 2% of stars with $r \sim 21$ have $g-i < 1$. For comparison, at high Galactic latitudes, the median $g-i$ color also becomes redder for fainter stars, but reaches a value of 1 at $r \sim 19.5$, or over 3 mag fainter than at low Galactic latitudes. Although the two sets of diagrams are encouragingly similar, there are a few detailed differences: the observed diagrams have more outliers and a few diagrams (e.g., $J-K$ versus $i-z$ and $i-z$ versus $r-i$) imply different reddening vectors than used in simulations ($R_V = 3.1$). We discuss these differences in more detail in the next section.

The resulting mock catalog is processed in exactly the same way as catalogs with observations. Note that the simulated photometry is generated with the same SED template library and dust extinction curve as used in fitting. We analyze four different fitting methods: we use both only-SDSS (four colors)

and SDSS-2MASS (seven colors) photometric data, and we consider both $R_V = 3.1$ (the true value) and R_V as a free fitted parameter. Only stars with $r < 20$ and $K < 13.9$ (Vega) are used in analysis; this cutoff results in the median photometric errors of 0.02 mag in the r band and 0.04 mag in the K band (and 0.06 in the u band, which is the only band where errors exceed the K -band errors). There are about 94,000 simulated stars that satisfy these criteria (the simulated area covers 25 deg^2). We first analyze the fitting results when R_V is fixed to its true value, and then extend our analysis to fitting results when R_V is a free parameter.

When R_V is fixed, the obtained χ_{pdf}^2 distributions closely resemble expected distributions for 2 and 5 degrees of freedom, with slightly more objects in the tails. For example, 86% and 93% of the sample are expected to have $\chi_{\text{pdf}}^2 < 2$ for only-SDSS and SDSS-2MASS cases, while we obtained 73% and 80%. The latter fractions remain the same when the r -band and K -band limits are relaxed by 1 mag. For further analysis, we only use stars with $\chi_{\text{pdf}}^2 < 2$.

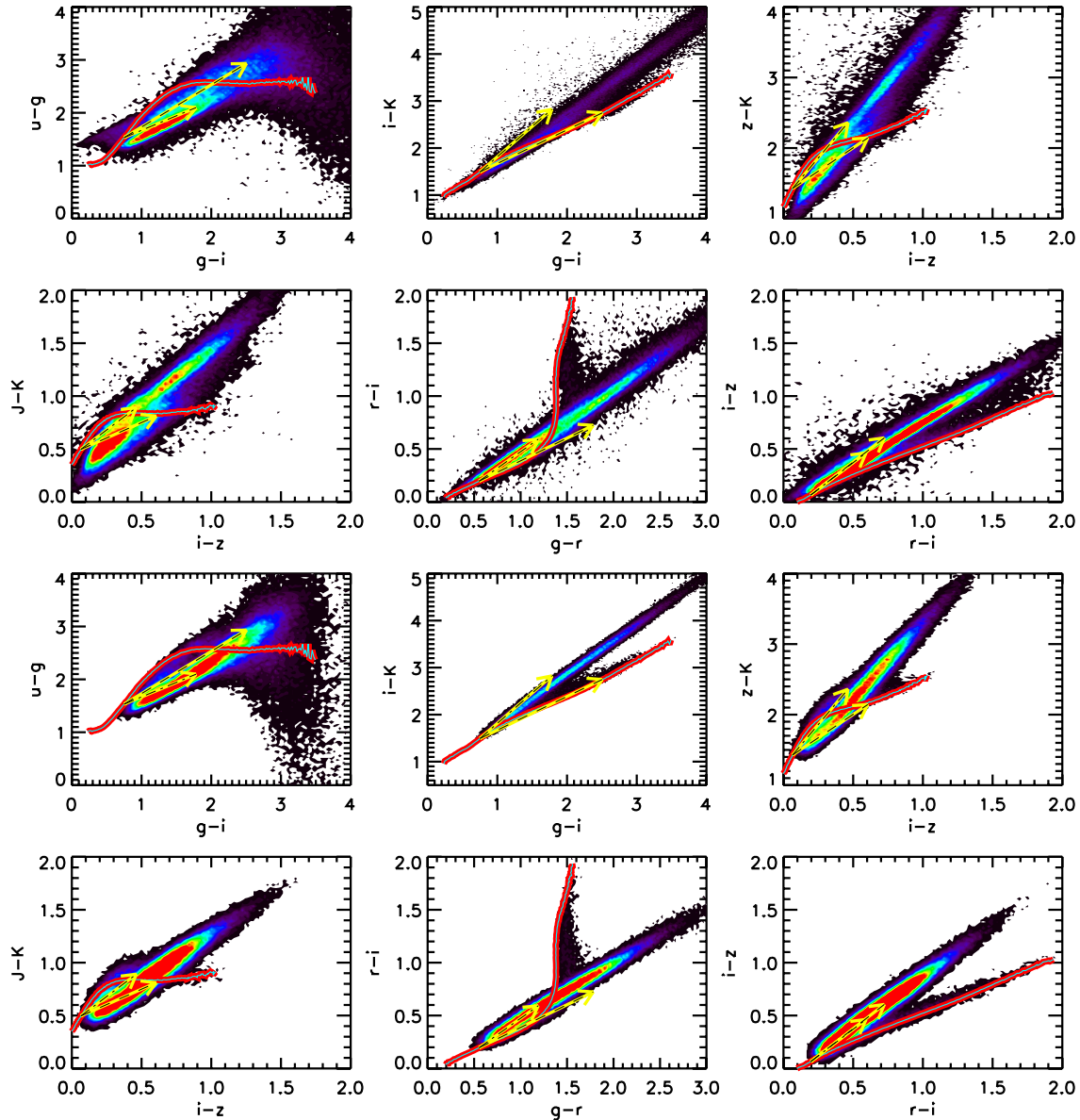


Figure 14. Comparison of six SDSS–2MASS color–color diagrams for data from the SEGUE $l \sim 110^\circ$ strip (the top six panels) and for a mock catalog produced with the *Galfast* code (the bottom six panels). The color-coded contours show the source counts on a linear scale. The two dashed arrows show reddening vectors for $A_r = 2$ and $R_V = 2$ and 4. The thick (red) line shows the Covey et al. (2007) empirical SED library and illustrates the morphology of the same diagrams observed at high Galactic latitudes (and corrected using the SFD map; typically $A_r \sim 0.1$). The two sets of diagrams are encouragingly similar, with a few detailed differences: the observed diagrams have more outliers, and a few diagrams (e.g., $J-K$ vs. $i-z$ and $i-z$ vs. $r-i$) imply different reddening vectors than used in simulations ($R_V = 3.1$).

(A color version of this figure is available in the online journal.)

The bottom left panel in Figure 13 shows the distribution of simulated stars in the intrinsic apparent magnitude versus color space, where we use only-SDSS best-fit intrinsic $g-i$ color and correct “observed” r band magnitudes using the best-fit A_r . Its overall similarity with the top left panel is encouraging. The main difference is at the blue edge, $g-i < 0.3$, with about 20% of stars having best-fit $g-i$ color biased blue (simulated sample essentially does not include stars with $g-i < 0.3$ because this is turnoff color for thick disk stars which contributes stars in that magnitude–color range). The same stars also have overestimated A_r . These biases are the result of the reddening–color degeneracy and could be mitigated by adopting a strong prior such as removing SEDs with $g-i < 0.3$ from the SED template library.

The bottom right panel compares the best-fit A_r to the input value. The best-fit A_r is systematically larger than the input val-

ues by about 10%. This overestimate is due to color–reddening degeneracy discussed above: when A_r is overestimated, the best-fit stellar color is biased blue. When the full SDSS–2MASS data set is used, the outliers seen in the bottom right panel in Figure 13 disappear, and the A_r bias is smaller by a few percent (10% versus 15% for blue stars). Overall, there is no dramatic improvement resulting from the addition of 2MASS photometry (the rms scatter for the A_r difference decreases from 0.42 mag to 0.33 mag when 2MASS photometry is added).

We find that the best-fit values based on only-SDSS data are biased when the u -band errors are large: A_r by 0.27 (true values are smaller) and $g-i$ by 0.2 mag (bluer) for stars with u -band errors of ~ 0.1 mag. When the SDSS–2MASS data set is used, both bias values fall to about 2/3 of only-SDSS values. Therefore, accurate u -band photometry is *crucial* for obtaining

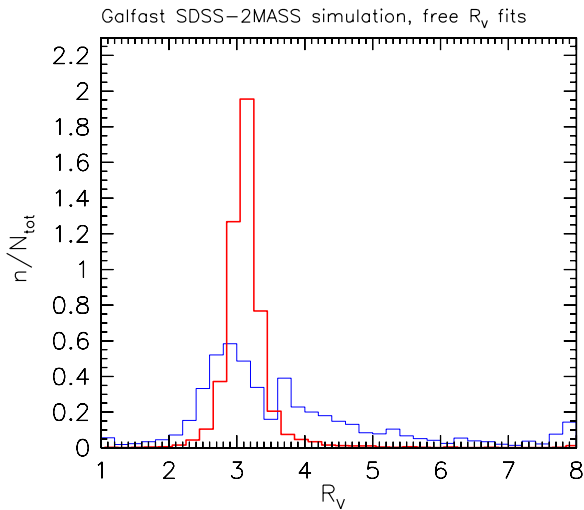


Figure 15. Comparison of the best-fit R_V values for SDSS-2MASS (narrow histogram) and only-SDSS (broad histogram) cases, using a simulated *Galfast* mock catalog. The input value is fixed to $R_V = 3.1$. The equivalent Gaussian widths determined from the interquartile range are 0.1 and 1.2, respectively. (A color version of this figure is available in the online journal.)

accurate best-fit results. In order to minimize the effects of this bias, we further limit the sample to stars with u -band errors below 0.05 mag. Unfortunately, only 40% of stars satisfy this cut.

The true errors in both stellar color and A_r (as determined by comparing the best-fit and true values) are about twice as large as marginalized errors computed using Equations (7) and (8), both in case of only-SDSS and SDSS-2MASS fits. This increased scatter is probably due to color- A_r degeneracies and deviations of the maximum likelihood contours from a 2D ellipse approximation: the errors in $g-i$ color and A_r errors are strongly correlated with a slope of $\delta(g-i)/\delta(A_r) \sim -0.65$ (when this correlation is used to “correct” the best-fit color by sliding them along this relation, the residuals are consistent with photometric errors; in other words, the entire “additional” color scatter is along this relation). The rms scatter for A_r errors is 0.42 mag and 0.33 mag for only-SDSS and SDSS-2MASS fits (20% and 16% for relative errors, i.e., errors normalized by true A_r), and the rms for $g-i$ color errors are 0.29 mag and 0.23 mag, respectively. We note that these errors are valid for individual stars, which suffer from the color-reddening degeneracy. When the results are averaged in small pixels on the sky, the scatter is significantly smaller (because the spread of stars along the color-reddening degeneracy manifold is fairly symmetric). For example, the rms error for A_r in 0.2×0.2 deg² pixels decreases by a factor 3–4 to a level of about 5%–10% (depending on the line-of-sight direction and the median A_r).

2.9.4. “Free- R_V ” Case

The analysis of fits with R_V treated as a free parameter revealed that SDSS data alone are insufficient to reliably constrain R_V , while SDSS-2MASS data set produced good results. Figure 15 compares the two resulting distributions of best-fit R_V (the input value is $R_V = 3.1$). When SDSS-2MASS photometry is used, R_V can be determined with a bias of < 0.1 , and a precision (rms) of 0.10 when all stars from the simulated sample with $\chi_{\text{pdf}}^2 < 2$ are considered. The R_V error is not correlated with stellar color nor with distance; A_r is the only parameter that controls the R_V error. As expected, the R_V error

increases for small A_r . A good practical limit is $A_r > 1$, which guarantees bias below 0.1 and an rms of at most 0.3. The R_V error decreases with A_r , and drops to 0.15 at $A_r = 2$ and below 0.1 for $A_r > 4$. For $A_r < 1$, the precision of R_V estimate significantly deteriorates; for $0.5 < A_r < 0.7$, the median best-fit R_V becomes biased to 3.2, with an rms of 0.5.

Unsurprisingly, the R_V error is much larger when using only-SDSS photometry; when considering all stars with $\chi_{\text{pdf}}^2 < 2$, the best-fit R_V is biased to 3.3, with an rms of 1.2, rendering it practically useless. The main reason for this poor performance are the facts that three free parameters are constrained using only four colors, and that these three parameters are strongly degenerate. The SDSS-2MASS data set shows superior performance when R_V is a free parameter not because 2MASS data can constrain R_V (using $C_\lambda(R_V)$ parameterization employed here), but because 2MASS data better determine A_r and intrinsic stellar color, which gives more leverage to SDSS data (mostly the u and g band) to constrain R_V .

As a result of this test, we conclude that *only R_V estimates based on SDSS-2MASS data set should be used*, and those only for stars with $\chi_{\text{pdf}}^2 < 2$ and $A_r > 1$.

2.9.5. “Dusty” Parallax Relation

The analysis of the mock *Galfast* sample uncovered an interesting possibility for identifying candidate red giant stars in SEGUE stripes. Distinguishing red giant stars using only-SDSS colors is difficult even at high Galactic latitudes (offsets from the main sequence stellar locus are at most 0.02–0.03 mag; for more details see Helmi et al. 2003), and seems futile at low Galactic latitudes. However, the best-fit A_r contains information about distance to a star, and this fact can be used for dwarf versus giant star separation at low Galactic latitudes (approximately, for $|b| < 5^\circ$).

After obtaining the best-fit intrinsic $g-i$ color, we compute distance to each star using a photometric parallax relation appropriate for main-sequence stars (I08). For red giants, the resulting distances are grossly underestimated (for example, a red giant star with $g-i = 1$ has $M_r \sim 0$, while main-sequence stars with the same color have $M_r \sim 6$, resulting in a distance ratio of ~ 15 for the same apparent magnitude). However, because red giant stars are much more distant than main-sequence stars of the same color, their best-fit values of A_r are also on average significantly larger. The latter is a consequence of the fact that A_r is proportional to the dust column along the line of sight, which in turn is roughly proportional to distance (although not exactly because the dust number density varies with position).

These differences in the best-fit A_r versus main-sequence distance behavior between main-sequence and red giant stars are illustrated in the top two panels in Figure 16. The dashed lines mark the region in the A_r versus distance diagram dominated by simulated stars with $M_r < 3$ (as illustrated in the bottom left panel). Red giant stars are found in the upper left corner of this diagram because their (main sequence) distances are too small given their A_r : it takes about 1 kpc of dust column to produce $A_r \sim 1$ mag and thus stars with $A_r > 1$ should be further than ~ 1 kpc.

This separation of red giant and main-sequence stars in the A_r versus distance diagram can be elegantly summarized via a relation that we dub “dusty parallax.” First, using the median best-fit A_r in narrow distance bins for stars with best-fit main-sequence distances $D < 0.5$ kpc (see the blob discernible in the

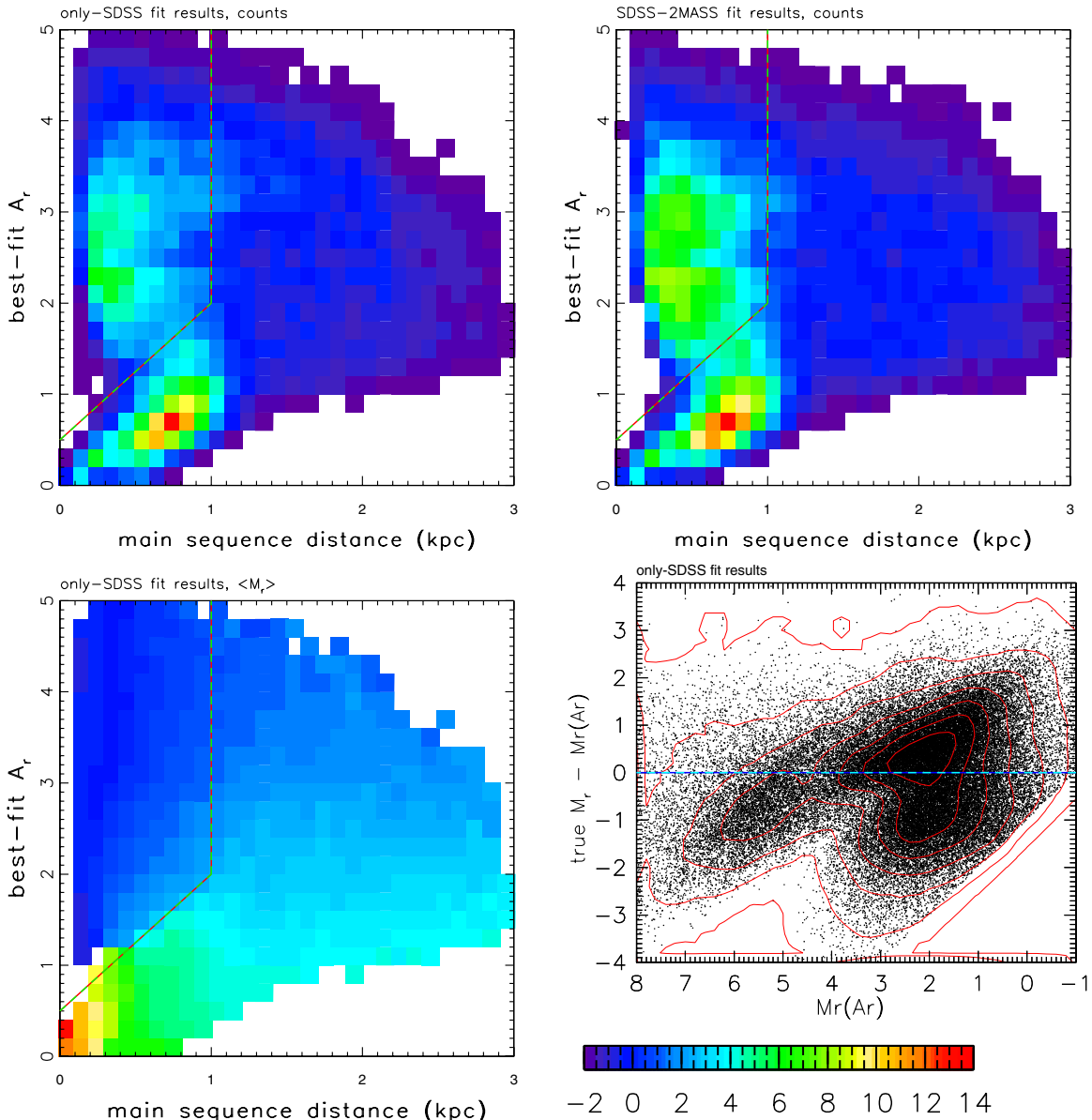


Figure 16. Left panel shows the relationship between best-fit A_r and distance computed using the SDSS-based best-fit stellar color and a photometric parallax relation appropriate for main-sequence stars, for the same simulated sample as in Figures 13 and 14. The color-coded map shows the counts of stars on a linear scale. The dashed lines isolate candidate red giant stars that have small distances and large A_r . The top right panel is analogous to the top left panel, except that the best-fit values correspond to SDSS-2MASS data. The bottom left panel shows the median input absolute magnitude (M_r) for stars in each pixel, color coded according to the legend in the lower right corner. The “red giant region” in the top two panels is dominated by giants ($M_r < 3$). The bottom right panel shows the difference between true absolute magnitude and an estimate obtained from the “dusty parallax relation” (see Equation (13)), as a function of the latter. The dashed line is added to guide the eye. The root-mean-square scatter between the two magnitudes (rms for the y axis) is 1.1 mag.

(A color version of this figure is available in the online journal.)

lower left corner), we obtained a linear relationship

$$A_r = 1.06 \frac{D}{\text{kpc}}. \quad (12)$$

The best-fit coefficient of $1.06 \text{ mag kpc}^{-1}$ is in good agreement with the coefficient corresponding to true A_r and distance for stars with $M_r > 5$, $1.13 \text{ mag kpc}^{-1}$. This agreement implies that a similar algorithm can be applied to real data (that is, the above coefficient of $1.06 \text{ mag kpc}^{-1}$ is based on simulations). Also, it is expected that the A_r/D ratio will vary with Galactic latitude and longitude because of the variations in the spatial distribution of ISM dust, so care needs to be taken to account for this effect.

This A_r versus D relation can be employed to estimate distance from the best-fit A_r for all stars, and in turn absolute magnitude M_r via “dusty parallax” relation

$$M_r^{\text{DPR}} = r - 5 \log_{10}(0.94 A_r) - A_r - 10. \quad (13)$$

A comparison of true M_r and M_r^{DPR} for *Galfast* simulation analyzed here (recall that the simulated area is bounded by $110^\circ < l < 112^\circ$ and $|b| < 5^\circ$) is shown in the bottom right panel in Figure 16. The rms scatter for the $(M_r - M_r^{\text{DPR}})$ difference is 1.2 mag (that is, much smaller than typical difference in absolute magnitude between red giants and red dwarfs with similar colors).

The coefficient from Equation (12) reflects the spatial distribution of dust generated using a smooth model from Amôres & Lépine (2005). In reality, localized clumps of dust will result in larger estimated distances and thus some main-sequence stars will be misinterpreted as candidate red giants. Nevertheless, the precision of this relation seems sufficient to broadly separate red giant and main-sequence stars using their best-fit $g - i$ color and A_r .

In many ways, this “dusty” parallax relation is similar to the reduced proper motion (RPM) method (for a detailed discussion, see Appendix B in Sesar et al. 2008); the main difference is that RPM estimates distance using its relationship with proper motion (assuming a fixed true tangential velocity, distance is inversely proportional to proper motion), while DPR estimates distance using a relationship between dust extinction and distance. We return to this relation and the selection of red giants when analyzing real data samples in the next section.

To summarize this testing section, the analysis of simulated data sets has revealed important limitations of the best-fit results, mostly stemming from the finite photometric precision of SDSS and 2MASS surveys. Most notably, the SDSS data set alone does not have enough power to reliably constrain R_V , and *only* R_V estimates based on SDSS–2MASS data set should be used, and those only for stars with $\chi_{\text{pdf}}^2 < 2$ and $A_r > 1$. The tests based on a mock *Galfast* catalog also demonstrated that the fraction of red giant stars in low Galactic latitude samples is much larger than observed at high Galactic latitudes. These conclusions are important for the interpretation of results described in the next section.

3. ANALYSIS OF THE RESULTS

We apply the method described in the preceding section (and summarized in Section 2.8) in four different ways. We fit separately the full SDSS data set (73 million sources) using only-SDSS photometry, and the SDSS–2MASS subset (23 million sources) using both SDSS and 2MASS photometry. We first consider a fixed C_λ extinction curve determined for Stripe 82 region (the coefficients listed in the first row in Table 1) and refer to it hereafter as the “fixed $R_V = 3.1$ ” case (although the best-fit CCM parameterization corresponds to $R_V = 3.0 \pm 0.1$). These fixed- R_V fits are obtained for the entire data set, including high Galactic latitude regions where dust extinction is too small to reliably constrain the shape of the extinction curve (i.e., R_V) using data for individual stars. To investigate the variation of R_V in high-extinction and low Galactic latitude regions, we use the CCM C_λ curves discussed in Section 2.7.2 (and shown in Figure 8). In this “free R_V ” case, we only consider the 10 SEGUE stripes limited to the latitude range $|b| < 30^\circ$, which include 37 million sources in the full SDSS data set, and 10 million sources in the SDSS–2MASS subset. As discussed in Section 2.9.4, the “free R_V ” results are only reliable when based on the full SDSS–2MASS photometric data set. We include the “free R_V ” only-SDSS results in the public distribution for completeness, but do not discuss them further.

The resulting best-fit parameter set is rich in content and its full scientific exploitation is far beyond the scope of this paper. The purpose of the preliminary analysis presented below is to illustrate the main results and to demonstrate their reliability, as well as to motivate further work by others—all the data and the best-fit parameters are made publicly available, as described in Appendix B.

We first analyze “fixed R_V ” fits and compare results based on only-SDSS data with those obtained using the full

SDSS–2MASS data set. This comparison shows that both data sets result in similar best fits, which adequately explain the observed dust-reddened SEDs of most stars in the samples. The main conclusion derived from the “free R_V ” fits is the lack of strong evidence for a significant overall departure from the canonical value of $R_V = 3.1$. In other words, our results are consistent with the majority of published work on interstellar dust properties.

3.1. Fixed R_V Case

Two sets of results based on a fixed dust extinction curve (“fixed $R_V = 3.1$ ” case) are compared: those based on the full SDSS–2MASS photometric data set whose seven colors provide better fitting constraints, and those for a larger and fainter only-SDSS sample which includes only four colors. We begin with a basic statistical analysis of the best-fit χ_{pdf}^2 distributions.

3.1.1. The Best-fit χ_{pdf}^2 Distributions

The distribution of the best-fit χ_{pdf}^2 , separately for low-extinction and high-extinction regions, and for low-S/N and high-S/N sources (bright and faint), is shown in Figure 17. As evident, there is no strong dependence of the shape of the best-fit χ_{pdf}^2 on signal-to-noise ratio (S/N). In low-extinction regions (top two panels) the obtained χ_{pdf}^2 distributions closely resemble theoretical χ_{pdf}^2 distributions with 2 and 5 degrees of freedom. This agreement is not too surprising because the empirical template library was derived using the same data set, and essentially demonstrates that cataloged photometric errors for SDSS and 2MASS are reliable.

In the high-extinction regions (although we discuss here only a single SEGUE stripe, we have verified that our conclusions are valid for all 10 stripes), the core of the observed χ_{pdf}^2 distributions is still similar to theoretically expected distributions (computed for Gaussian error distributions, and assuming that SEDs of all stars in the sample are well described by the template library), but tails are more extended than in low-extinction high-latitude regions. For comparison, about 70% of a sample is expected to have $\chi_{\text{pdf}}^2 < 1.2$ (valid for the low number of degrees of freedom considered here), while we obtained about 50% for the observed distributions. The increased fraction of red giants at low Galactic latitudes, increased but unrecognized photometric errors (e.g., due to crowding), more complex dust extinction curve behavior than captured by the adopted CCM parameterization, as well as increased metallicity of disk stars, may all contribute to the tails of the observed χ_{pdf}^2 distributions.

For further analysis, we use subsamples of stars with $r < 19$, $K < 14$ (Vega scale), and $\chi_{\text{pdf}}^2 < 2$, unless noted otherwise. These criteria select stars with relatively small photometric errors (typically < 0.05 mag in most bands) and whose reddened SEDs are well described by the template SED library and the CCM extinction curve. About 50%–60% of stars in only-SDSS sample, and 70%–80% stars in SDSS–2MASS subsample, are typically selected by the adopted $\chi_{\text{pdf}}^2 < 2$ cut (for theoretical χ_{pdf}^2 distributions with 2 and 5 degrees of freedom, 86% and 93% of stars would satisfy this χ_{pdf}^2 cut).

3.1.2. The Northern Galactic Cap Region

Due to small A_r for the $b > 30^\circ$ sky region (the median A_r from the SFD map is ~ 0.08 mag), the errors for best-fit A_r for individual stars can be as large as best-fit A_r itself when using

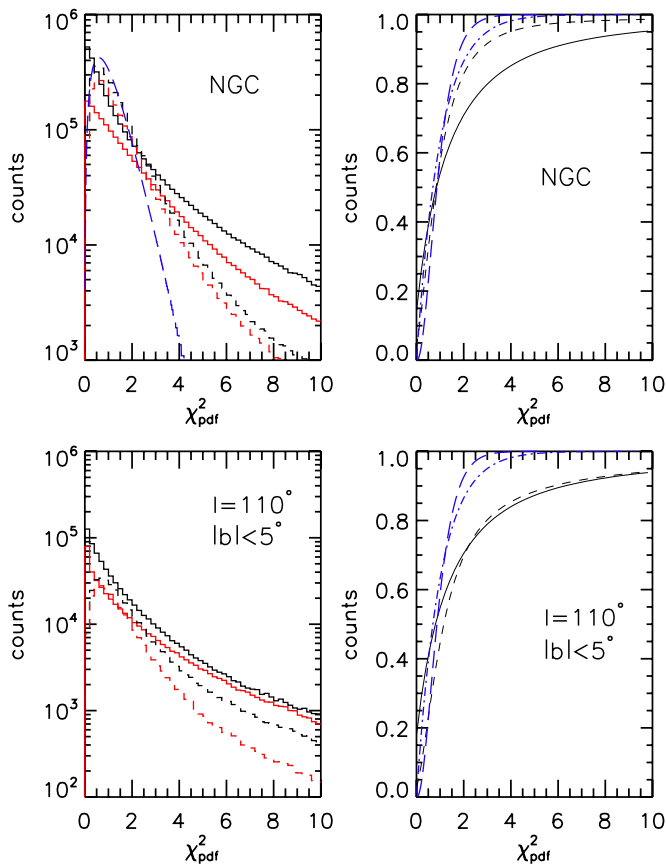


Figure 17. Distribution of the best-fit χ^2_{pdf} ($R_V = 3.1$), with differential distributions in the left two panels and cumulative distributions in the right two panels. The top two panels correspond to the north Galactic cap region ($b > 45^\circ$) and the bottom two panels to the SEGUE $l \sim 110^\circ$ strip, limited to $|b| < 5^\circ$ (a high-extinction region). The solid lines are used for SDSS-only fits and the dashed lines for fits to SDSS–2MASS data. In the two left panels, the top solid line corresponds to subsamples of stars with $r < 20$, and the bottom solid line to stars with $20 < r < 21$. The top dashed line corresponds to the full SDSS–2MASS sample, and the bottom dashed line to subsamples with $K < 13.9$ (Vega scale, approximately corresponding to K -band errors up to 0.05 mag). The solid lines in the right panels correspond to the full SDSS sample, and the short-dashed lines to the full SDSS–2MASS sample. The dot-dashed and long-dashed lines correspond to χ^2_{pdf} distributions with 2 and 5 degrees of freedom. The long-dashed line in the top left panel corresponds to the χ^2_{pdf} distribution with 5 degrees of freedom for the full SDSS–2MASS sample.

(A color version of this figure is available in the online journal.)

only-SDSS fits (fixed R_V case). Both the formal A_r errors and the differences between best-fit and SFD values for A_r begin to increase rapidly for $r > 18$ and become unreliable for $r > 19$. This behavior is in agreement with tests described in Section 2.9 and the behavior of SDSS photometric errors as a function of magnitude (even for blue stars, the median u band error is already 0.05 mag at $r = 19$, and 0.2 mag when stars of all colors are considered).

Nevertheless, by taking a median value for typically several hundred stars per $\sim 1 \text{ deg}^2$, a map can be constructed that reproduces the features seen in the SFD map (see the top left panel in Figure 18). Quantitative analysis of the median differences between the best-fit A_r and the SFD A_r values shows that the former are larger by about 50% on average, with a scatter of about 20%. This bias is probably due to color–reddening degeneracy and small extinction at high Galactic latitudes which is only a factor 2–3 larger than photometric errors. An additional

effect contributing to this bias are zero-point calibration errors in SDSS photometry: the median differences between the best-fit A_r and the SFD A_r values show a structure reminiscent of the SDSS scanning pattern (see the top right panel in Figure 18). These coherent residuals imply problems with the transfer of SDSS photometric zero points across the sky.

The median differences between observed and best-fit template magnitudes show deviations of up to 0.01 mag, and are largest in the i band, as illustrated in the bottom left panel in Figure 18. Therefore, these relatively small local calibration errors (each of the six scanning strips in an SDSS scan, i.e., the “camera columns,” is independently calibrated) are misinterpreted as a local extinction variation at the level of a few times 0.01 mag.

With the addition of 2MASS photometry, the agreement with the SFD map improves. The best-fit A_r values are overestimated, relative to SFD values, by only ~ 0.02 mag (25% on average), and the median differences do not show structure resembling the SDSS scanning pattern (see the bottom right panel in Figure 18). We note that $r < 18$ selection limit (and $K < 14$ in 2MASS case) results in about one star per the resolution element of SFD map. Therefore, to significantly improve the spatial resolution of the SFD extinction map at high Galactic latitudes, a sample several magnitudes deeper than SDSS–2MASS sample is required.

3.1.3. The SEGUE Stripes

The main goal of this work is to determine extinction at low Galactic latitudes. We consider ten ~ 2.5 wide SEGUE stripes with $|b| < 30^\circ$. The full SDSS sample includes 37 million sources, with 10 million sources in the SDSS–2MASS subset. We find that results based on the two data sets are similar, though the latter is expected to produce more reliable results. We first illustrate the behavior of best-fit A_r as a function of distance for all stripes, and then provide more quantitative discussion of the differences in best-fit results in the next section, which is focused on a single stripe ($l \sim 110^\circ$). We also provide a comparison to the SFD extinction maps further below.

A visual summary of the best-fit A_r using only-SDSS fits for the 10 SEGUE stripes, in the range $|b| < 5^\circ$ (we use such latitude-restricted subsamples for emphasizing high-extinction regions) and for three distance slices ranging from 0.3 kpc to 2.5 kpc, is shown in Figure 19. Distances to stars are determined by assuming that all sources are main-sequence stars, and using photometric parallax relation from I08 with $[\text{Fe}/\text{H}] = -0.4$ (with the best-fit intrinsic colors). An expected scatter in metallicity of 0.2–0.3 dex for disk stars corresponds to about 10%–15% uncertainty in distance. Although not all sources are main-sequence stars (such as red giants, which have grossly underestimated distances, see Section 3.1.5 below for discussion), the fraction of main-sequence stars in the samples is sufficiently large that the median A_r is not strongly biased. Furthermore, sources whose SEDs are significantly different from the main-sequence SEDs (such as quasars and binary stars) are not included: the figures are constructed only with sources that have the best-fit $\chi^2_{\text{pdf}} < 2$. We also excluded red giant candidates, as described below.

It is easily discernible from Figure 19 that the extinction along the line of sight (that is, A_r) increases with distance. On average, the stripes toward the Galactic center have more large-extinction ($A_r > 1$) regions. In several directions, A_r exceeds several magnitudes and practically no stars are detected by SDSS.

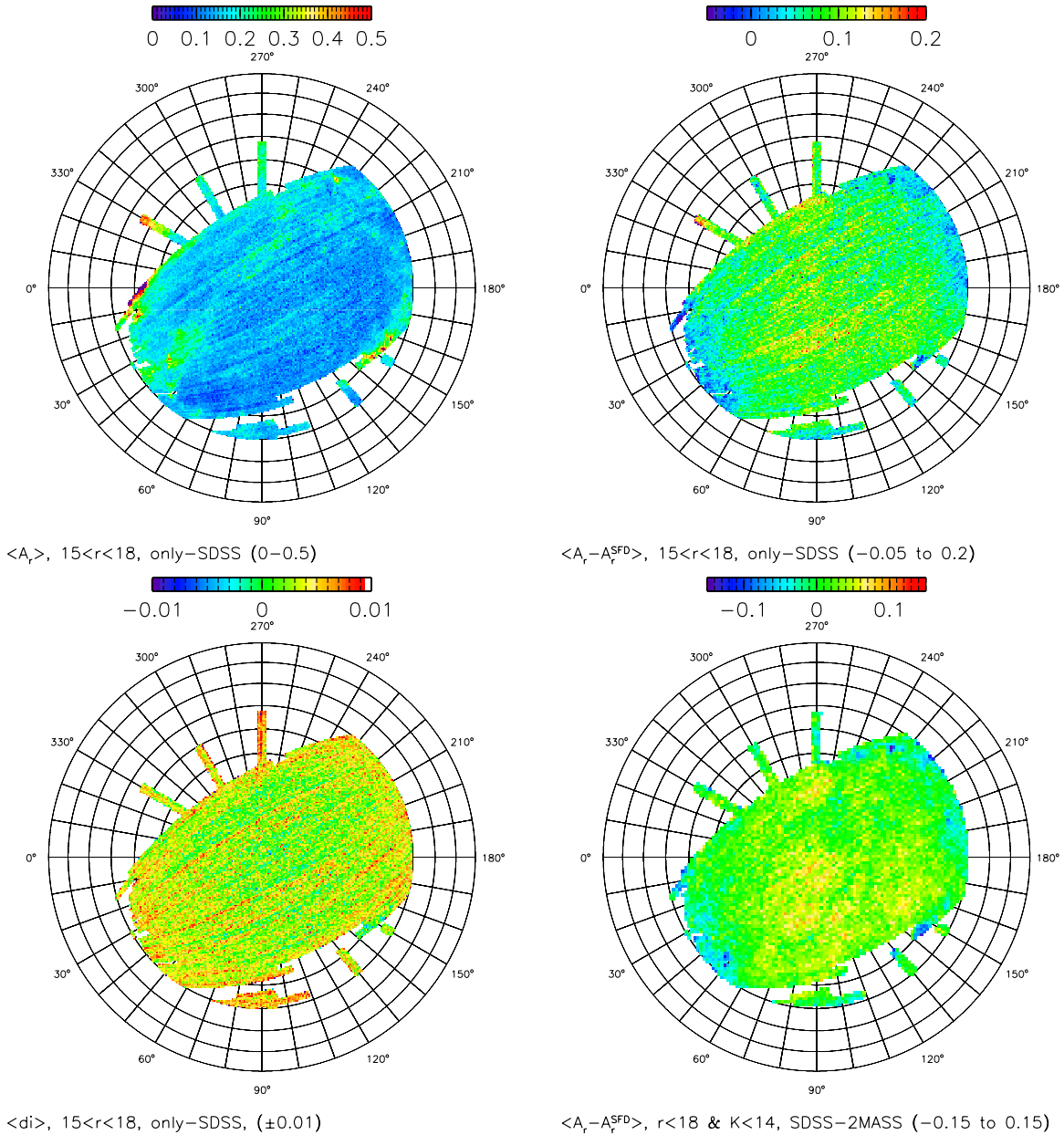


Figure 18. Analysis of the best-fit results for A_r in the low-extinction region with $b > 30^\circ$. The top left panel shows the median A_r in 0.6 deg^2 pixels in Lambert projection. The values are linearly color coded according to the legend. Stars with $15 < r < 18$ and $\chi_{\text{pdf}}^2 < 2$ from only-SDSS sample with fixed R_V are used for the plot. The median difference between A_r and the values given by the SFD map is shown in the top right panel. Note the striping reminiscent of the SDSS scanning pattern. The bottom left panel shows the median difference between observed and best-fit template magnitudes in the i band. The bottom right panel is analogous to the top right panel, except that only the subset of stars also detected by 2MASS ($K < 14$) and with full SDSS–2MASS fits (fixed R_V) are used. Note the much better agreement with the SFD values than in the top right panel (and the different color scale). For more details, please see Section 3.1.2.

(A color version of this figure is available in the online journal.)

3.1.4. Selection Function Differences for Only-SDSS and SDSS–2MASS Subsamples

Another projection of the sky position–distance– A_r space is shown in Figures 20 (only-SDSS case) and 21 (SDSS–2MASS case). As evident, the morphology of these A_r versus distance diagrams differs significantly between the two subsamples. The main reason for these changes is different sample selection functions in the flux–color space—and not differences in the best-fit A_r or distance values which agree well on a star by star basis (see the next section).

For only-SDSS case, the main selection criterion (in addition to $\chi_{\text{pdf}}^2 < 2$ in both cases) is $r < 19$ and the u -band error

limit of 0.05 mag. The latter condition is necessary to assure reliable fitting results when only four colors are used and results in a strong bias toward the blue end of the observed color distribution. In SDSS–2MASS case, it is sufficient to require $K < 15$ (Vega) to obtain reliable fitting results because there are seven colors, and because this condition limits the K -band and u -band errors to about 0.1 mag (with much smaller errors in other bands). This selection condition results in a strong bias toward the red end of the observed color distribution. Due to their selection functions, the effective r -band limiting magnitude for reliable only-SDSS samples varies from $r \sim 17$ at $g - i = 1$ to $r \sim 15$ at $g - i = 3$, while for SDSS–2MASS samples it

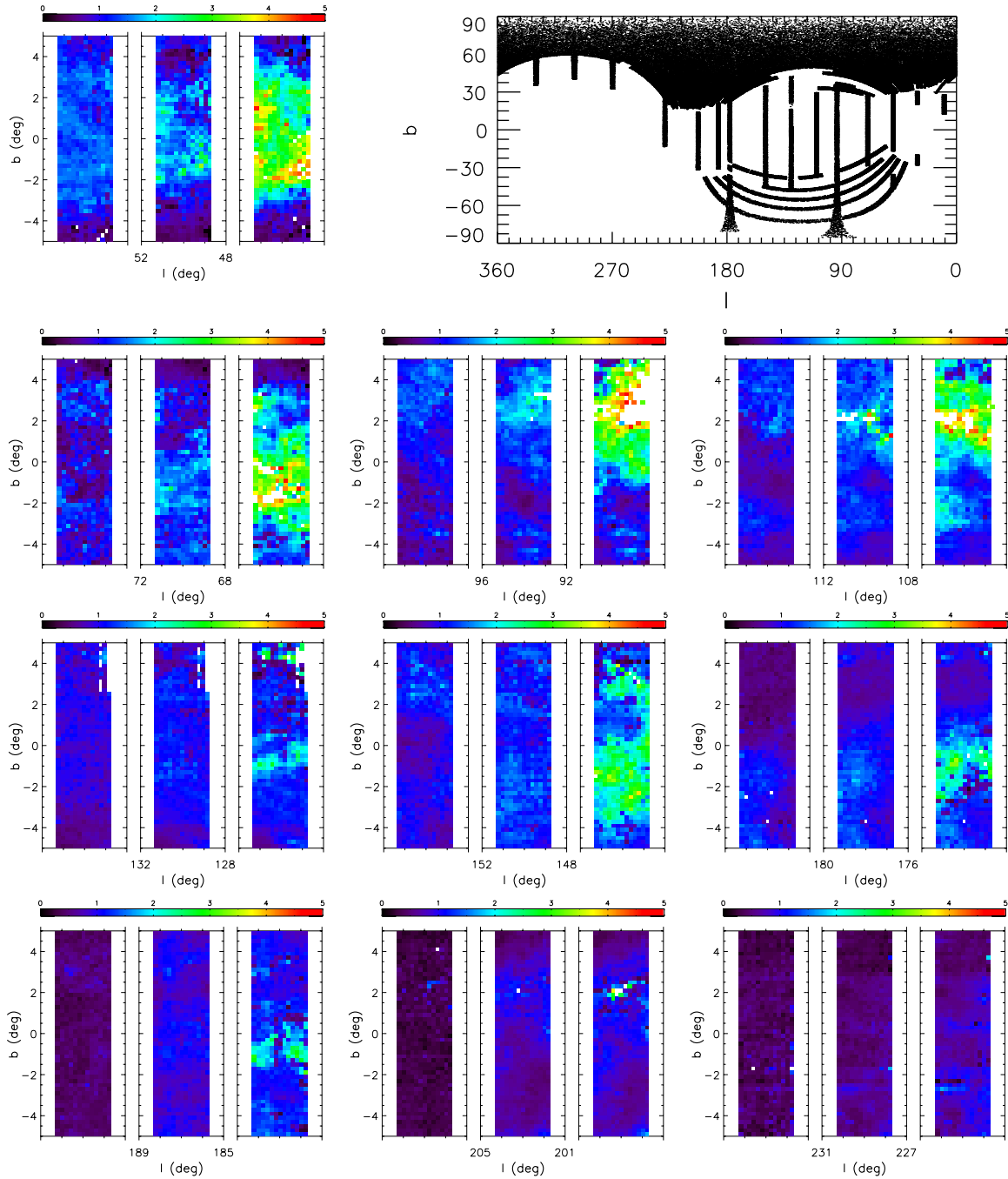


Figure 19. Color-coded maps show the best-fit A_r based on SDSS data for the 10 analyzed SEGUE stripes. Each stripe is limited to the range of $|b| < 5^\circ$. A fixed $R_V = 3.1$ is assumed. The legend above each panel shows the color scale, and each 12×12 arcmin² pixel shows the median A_r . For each stripe, three distance ranges are shown: 0.3–0.6 kpc (left), 1–1.5 kpc (middle), and 2–2.5 kpc (right). It is assumed that all stars are on main sequence when estimating distances. Only stars with best-fit $\chi^2_{\text{pdf}} < 2$ and outside the red giant region (selected here by $A_r < 1.5 + 1.5 D_{\text{kpc}}$) are used for the plot. The top right panel shows the sky coverage of the full analyzed data set.

varies from $r \sim 17$ at $g - i = 1$ to $r \sim 20$ at $g - i = 3$. As a result, SDSS–2MASS samples contain many more nearby red dwarfs at distances below 500 pc, while only-SDSS sample extends further than SDSS–2MASS sample, to about 2.5 kpc. On average, about twice as many stars survive the quality cuts for SDSS–2MASS sample as for only-SDSS sample (although the latter typically contains about four times as many stars at $|b| < 5^\circ$ before any selection).

In the A_r versus distance diagram, the selection cutoff for SDSS–2MASS sample is nearly vertical, and limits the sample to distances below about 1.5 kpc (assuming $A_r < 5$ and main-

sequence stars). For only-SDSS sample, the upper limit on u -band error introduces a diagonal selection boundary that excludes stars in the upper right corner. With the selection criteria adopted above, the sample becomes limited to $A_r < 2$ at a distance of about 1 kpc, with an overall distance limit of about 2.5 kpc.

The slopes of A_r versus distance relations along main-sequence locus seen in Figures 20 and 21 constrain the local (within 1 kpc) extinction per unit distance normalization to the range $A_r/D = 0.7\text{--}1.4$ mag kpc⁻¹, with larger values corresponding to smaller angular distances from the Galactic center.

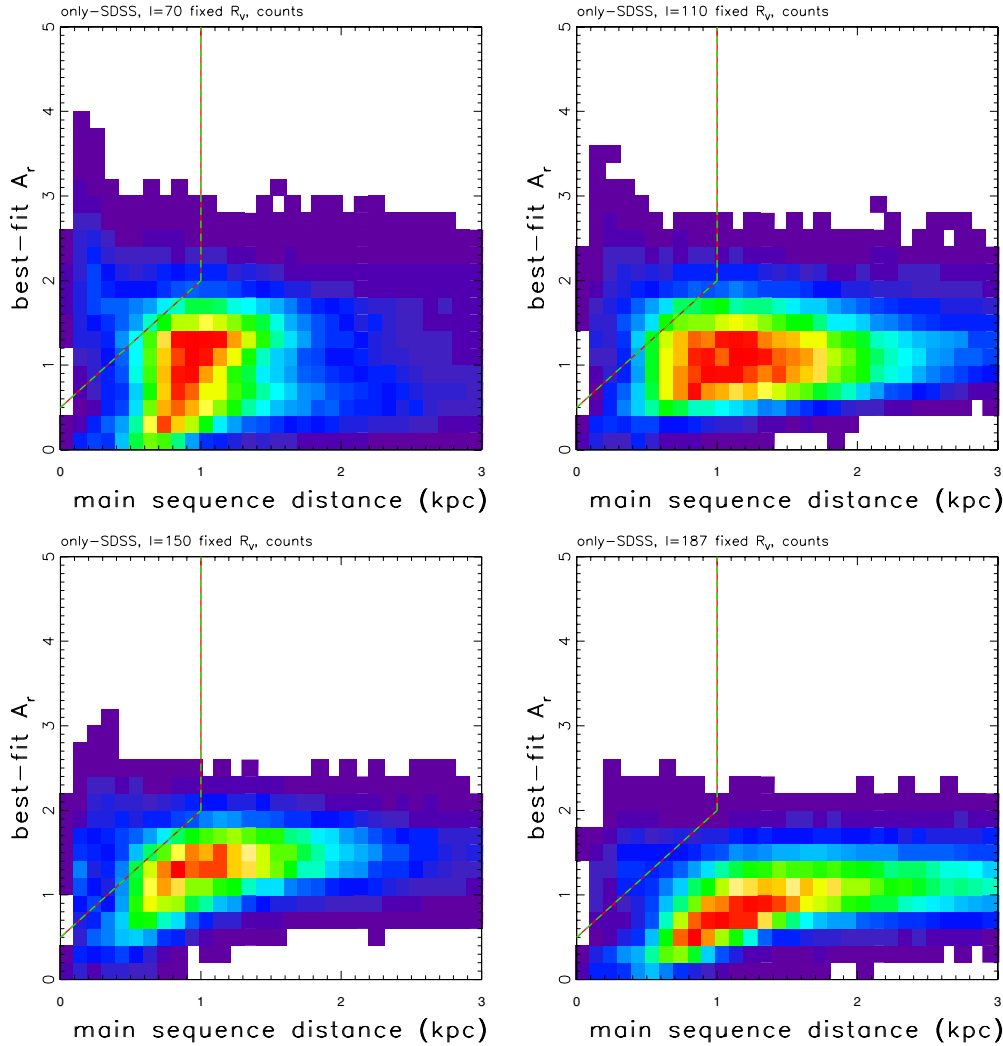


Figure 20. Counts of stars in the only-SDSS case best-fit A_r vs. best-fit main-sequence distance diagram for four SEGUE strips (top left: $l = 70^\circ$, top right: $l = 110^\circ$, bottom left: $l = 150^\circ$, bottom right: $l = 187^\circ$; for all panels $|b| < 5^\circ$). Only stars with $\chi_{\text{pdf}}^2 < 2$, $r < 19$ and error in the u band below 0.05 mag are used. Counts are normalized to the maximum value and color coded on the same linear scale, from blue (low) to red (high). The two dashed lines mark a region dominated by red giant stars (the top left corner).

(A color version of this figure is available in the online journal.)

The variation of this normalization with Galactic longitude is consistent with the exponential scale length for thin disk stars obtained by J08 ($L_1 = 2.6 \pm 0.5$ kpc, see their Table 10). Nevertheless, the variation for A_r/D with longitude observed here is more complex than predicted by simple axially symmetric dust distribution model.

3.1.5. The Selection of Candidate Red Giant Stars

The A_r versus distance diagrams based on SDSS–2MASS data (see Figure 21) show an excess of sources in the top left corner (the effect is not as strong for only-SDSS case because the selection effects due to the u -band error limit, discussed in the previous section, remove most of these sources). Based on a mock catalog discussion in Section 2.9.5, these sources are consistent with red giant stars. Informed by their distribution, and clear separation from the locus of main-sequence stars, we adopted the following criteria for the selection of candidate red giants.

1. Best-fit main-sequence distance below 1 kpc, $D_{\text{kpc}} < 1$.
2. Best-fit extinction, $A_r > 1.5 + 1.5 D_{\text{kpc}}$.

3. Best-fit intrinsic color, $0.4 < g - i < 1.4$.
4. Low Galactic latitudes, $|b| < 5^\circ$.

The first two criteria are based on the morphology observed in the A_r versus distance diagrams, and the third criterion removes outliers whose best-fit intrinsic colors are inconsistent with the color distribution for the majority of sources selected by the first two criteria. The last criterion limits the method to regions with large extinction. Detailed inspection of the morphology in the A_r versus distance diagrams for all 10 SEGUE stripes shows that a longitude-dependent selection criteria (especially the second condition) would improve performance, and we recommend such approach in case of, for example, target selection for spectroscopic follow up. Since the separation of the main-sequence locus and the red giant clump is robust in all SEGUE stripes, improved criteria should be easy to obtain. For the purposes of analysis presented below, the above uniform selection criteria will suffice.

We applied these criteria to all 10 SEGUE stripes and found that the fraction of selected stars varies significantly with Galactic longitude, from $\sim 15\%$ for stripes at $l = 50^\circ$ and $l = 70^\circ$ to $\sim 2\%$ for stripes within 20° from the Galactic

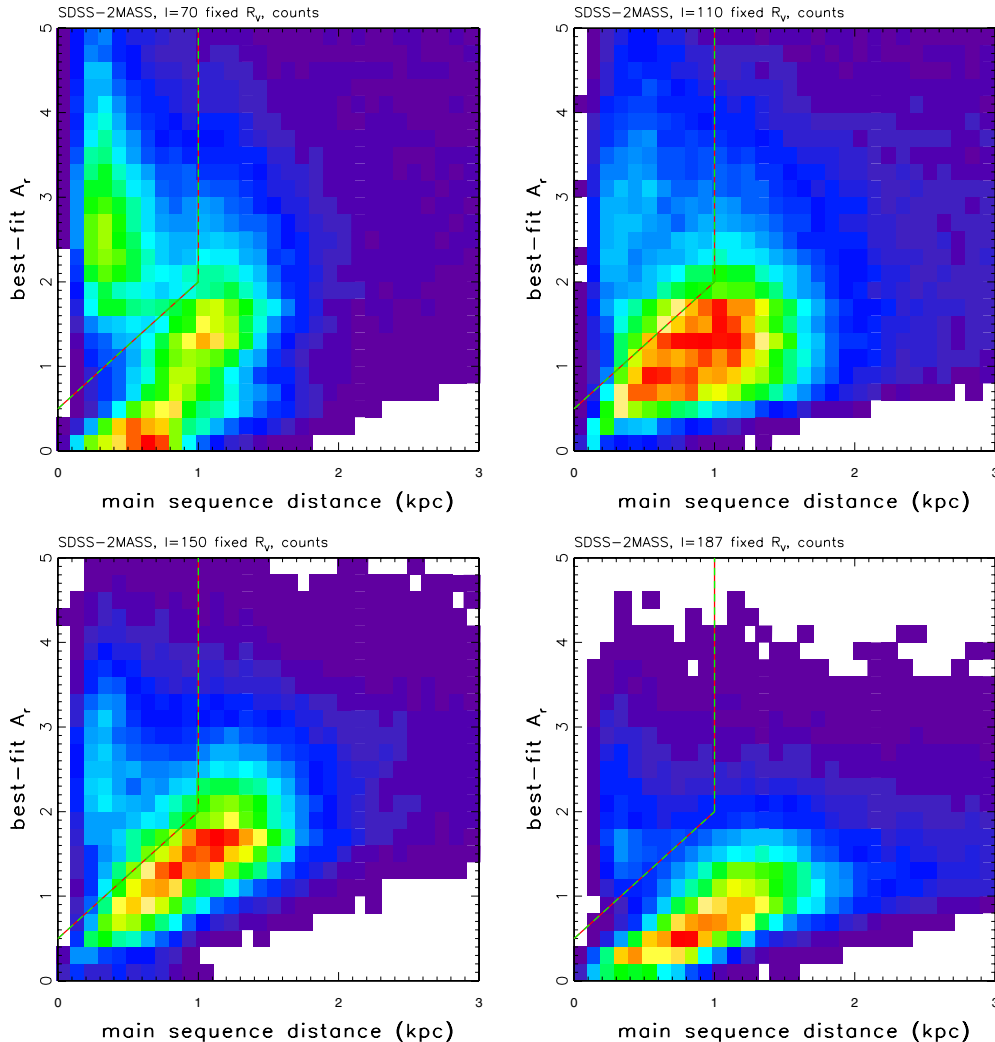


Figure 21. Analogous to Figure 20, except for best fits based on SDSS–2MASS sample (only stars with $\chi_{\text{pdf}}^2 < 2$ and $K < 15$ on Vega scale are used). Note the larger fraction of red giant stars in the top left corner, and a smaller distance limit, compared to Figure 20 and that the fraction of giants decreases with Galactic longitude. (A color version of this figure is available in the online journal.)

antcenter. The inclination of the main-sequence stellar locus in the A_r versus distance diagrams also varies with Galactic longitude, with its slope (determined for distances up to 1 kpc) decreasing from about 2.0 mag kpc^{-1} for the $l = 50^\circ$ stripe to 0.6 mag kpc^{-1} for the $l = 187^\circ$ stripe. Hence, our selection criterion 2 above could be improved by taking this variation into account (for the same reason, the proportionality “constant” in Equation (12) varies with longitude).

The observed variation of the fraction of candidate red giants with Galactic longitude represents a strong constraint for the Galactic structure models, and the change of A_r versus distance slope reflects the variation of dust number volume density in the Galactic disk. Hence, the data presented here can be used to improve Galactic stellar population models such as *Galfast* and TRILEGAL (which simulate giant populations), and dust distribution models, such as the Amôres & Lépine (2005) model employed by *Galfast*. The required detailed analysis is beyond the scope of this work.

3.1.6. Detailed Analysis of the $l \sim 110^\circ$ SEGUE Stripe

For a detailed analysis of the best-fit results, we select a single fiducial SEGUE stripe with $l \sim 110^\circ$. A simple but far-

reaching conclusion of the work presented here is that fits to intrinsic stellar SEDs and dust extinction on per star basis are capable of reproducing the morphology of observed color–color diagrams in highly dust-extinguished regions. This success is illustrated in Figure 22, where six characteristic color–color diagrams constructed with observed SDSS–2MASS photometry are contrasted with analogous diagrams constructed using best-fit results. We reiterate that the observed morphology in these diagrams at low Galactic latitudes is *vastly different* than at high latitudes (the latter is illustrated in the figure by the Covey et al. locus).

When considering SDSS–2MASS sample, fits based on the full seven-color set and those restricted to the four SDSS colors produce quantitatively similar though not identical results. The rms scatter of the difference in best-fit intrinsic colors is 0.04 mag, and rms for best-fit A_r difference is 0.07 (the median A_r is 1.9). For $A_r \sim 5$, the values based on only-SDSS photometry become biased (larger) by about 4% relative to SDSS–2MASS values. A star-by-star comparison presented in Figure 23 shows a few regions (e.g., $g - i \sim 1.5$ and small $g - i$) where results can differ substantially; nevertheless, the fraction of affected sources is small and negligible when results are averaged over many stars. The latter point is illustrated in

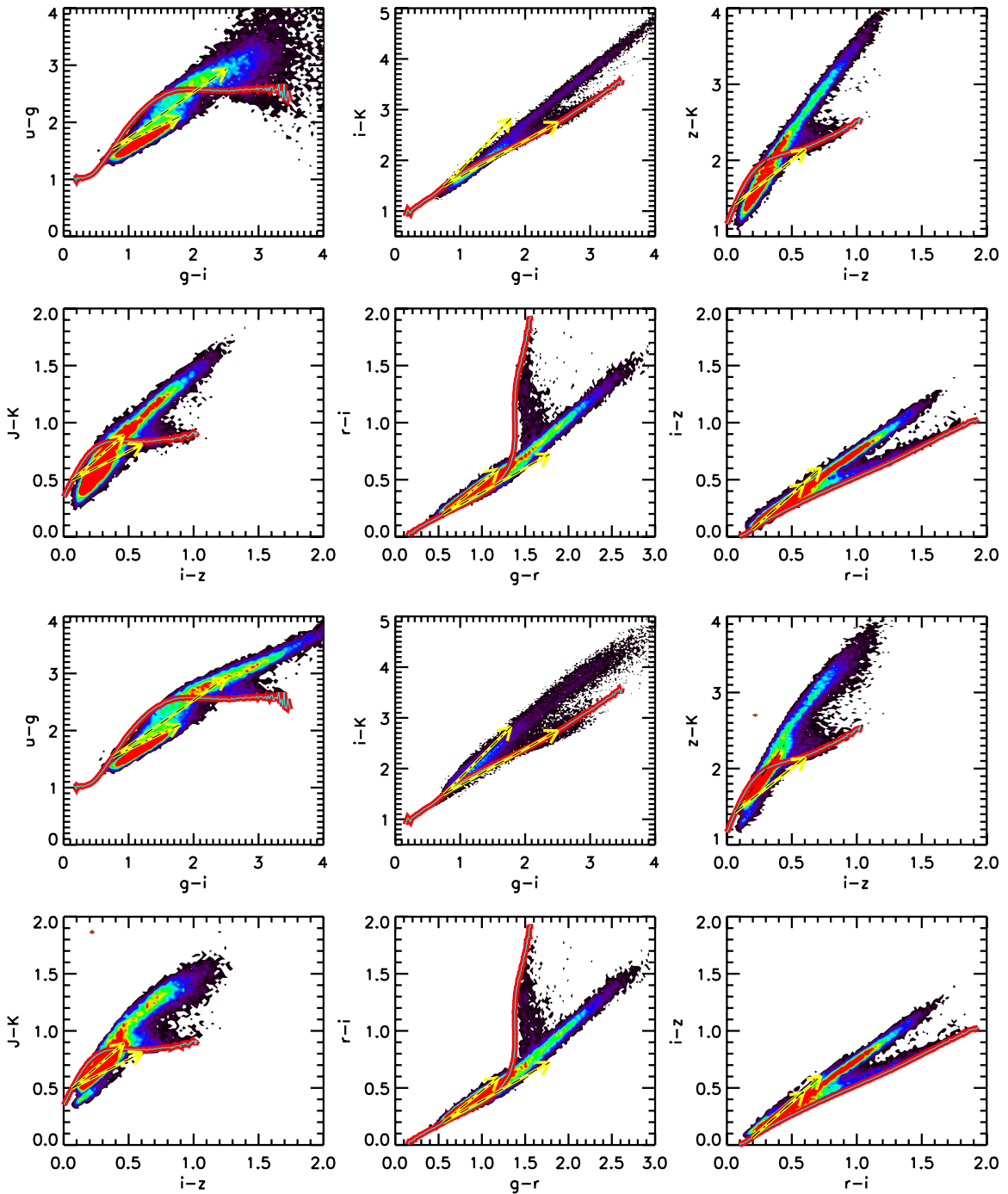


Figure 22. Comparison of six SDSS–2MASS color–color diagrams using data from the SEGUE $l \sim 110^\circ$ strip (the top six panels; same as the top six panels in Figure 14, except that here only stars with $\chi^2_{\text{pdf}} < 2$ are used) and the best-fit template colors based on SDSS–2MASS data set (the bottom six panels, in the same order). The thick lines show the Covey et al. (2007) empirical SED library and illustrate the morphology of the same diagrams observed at high Galactic latitudes. The two sets of diagrams are encouragingly similar: fits to intrinsic stellar SED and dust extinction on per star basis are capable of reproducing the morphology of observed diagrams in highly dust-extincted regions.

(A color version of this figure is available in the online journal.)

Figure 24, which compares the two A_r maps for stars at a limited range of distances. The two maps agree to better than 0.05 mag even in regions where $A_r > 4$. This agreement demonstrates that SDSS data alone are sufficient to obtain the best-fit intrinsic color and extinction along the line of sight for the majority of stars (when R_V is fixed). In the rest of analysis, we use SDSS–2MASS results, except in a few cases where we explore distances beyond 2 kpc.

A cross-section of the three-dimensional A_r map, based on only-SDSS sample from the $l \sim 110^\circ$, is shown in Figure 25. As evident, the best-fit A_r increases with the stellar distance between 0.3 kpc and 2.5 kpc. It is noteworthy that the two quantities are determined independently (distance is computed a posteriori, from the best-fit apparent magnitude). A closer look at distances below 1 kpc using SDSS–2MASS data set is shown in Figure 26. An impressive feature is the abrupt jump

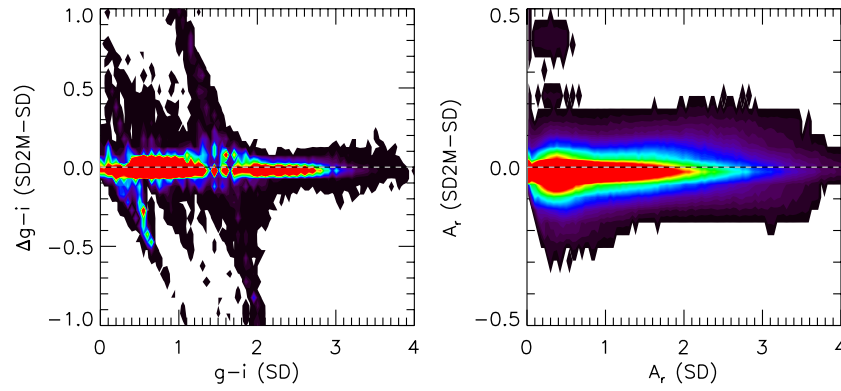


Figure 23. Comparison of the best-fit $g-i$ (left panel) and A_r (right panel) values obtained with a fixed $R_V = 3.1$ for SDSS-2MASS sample from the SEGUE $l \sim 110^\circ$ stripe, using two different fitting methods. The abscissae show the best-fit values obtained using only-SDSS data set (four fitted colors), and the ordinates correspond to the residuals of the SDSS-2MASS (seven fitted colors) minus the only-SDSS data sets. The number density of stars increases linearly from black to blue to red. The dashed lines are added to guide the eye.

(A color version of this figure is available in the online journal.)

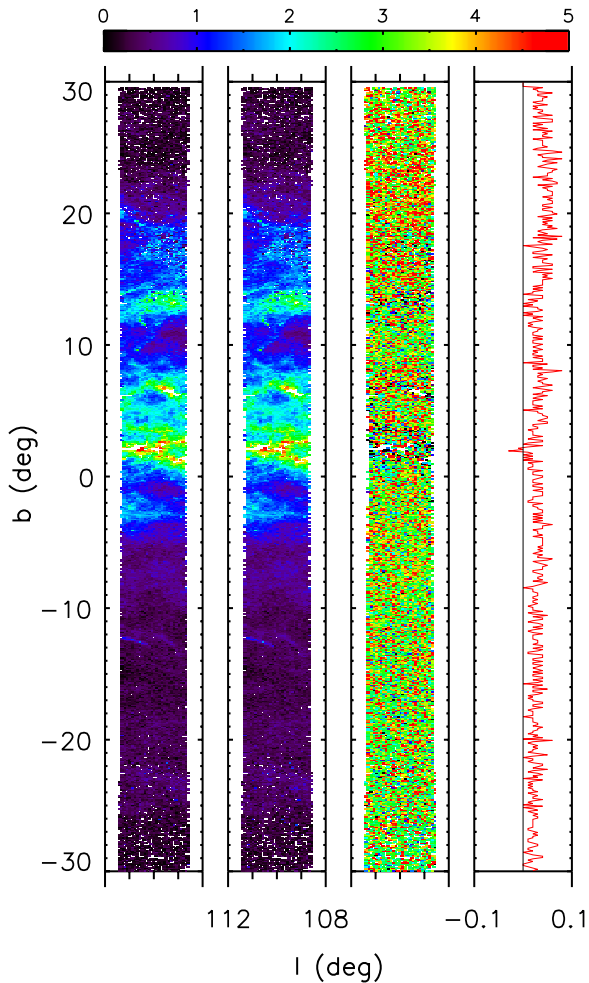


Figure 24. Analysis of the differences in the best-fit A_r between fits based on SDSS-2MASS data set (first panel from the left) and those based on only-SDSS data (second panel). Only stars with best fit $\chi^2_{\text{pdf}} < 2$, $r < 20$ and main-sequence distance 0.5–1 kpc are used for the plot. The top legend shows the coloring code for these two panels, and each 6×6 arcmin² pixel shows the median A_r for stars with $\chi^2_{\text{pdf}} < 2$. The third panel shows the median difference between the two best-fit A_r values (the second panel minus the first panel), with the color coding using the same palette, *except that the limits are ± 0.1 mag*. The fourth panel shows the median difference in A_r (i.e., the third panel) for 0.2 wide bins of Galactic latitude.

(A color version of this figure is available in the online journal.)

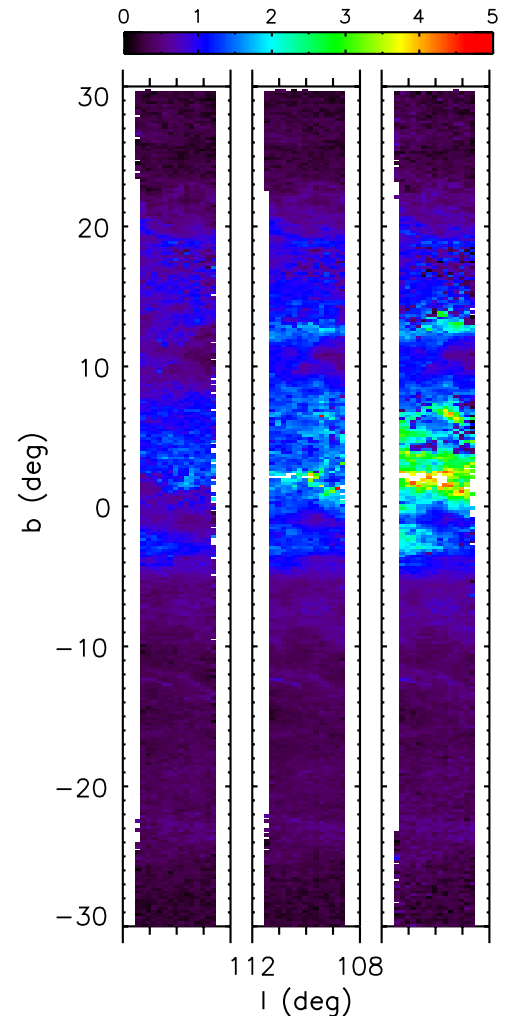


Figure 25. Color-coded maps show the best-fit A_r based on only-SDSS data set for the SEGUE $l \sim 110^\circ$ strip. The legend shows the color scale, and each 12×12 arcmin² pixel shows the median A_r . The three panels correspond to main-sequence distance range: 0.3–0.6 kpc (left), 1–1.5 kpc (middle), and 2–2.5 kpc (right). Only stars with best-fit $\chi^2_{\text{pdf}} < 2$ and outside the red giant region (selected here by $A_r < 1.5 + 1.5 D_{\text{kpc}}$) are used for the plot.

(A color version of this figure is available in the online journal.)

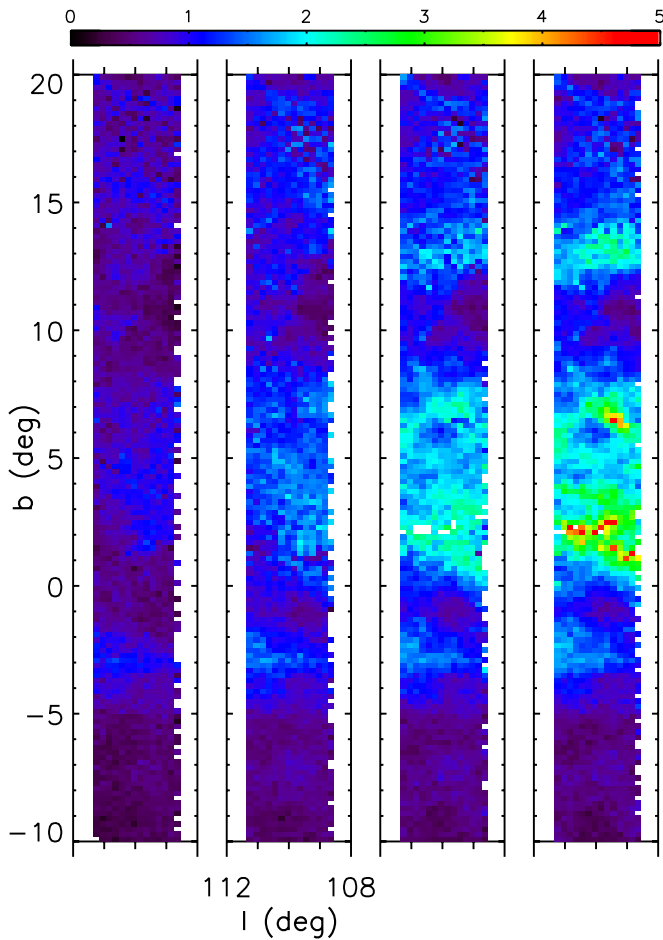


Figure 26. Analogous to Figure 25, except using the SDSS–2MASS data set and different distance slices (left to right: 0.1–0.5 kpc, 0.5–0.7 kpc, 0.7–0.9 kpc, 0.9–1.1 kpc). Note the abrupt increase in A_r for stars toward $b \sim +2^\circ$ that are more distant than 0.9 kpc.

(A color version of this figure is available in the online journal.)

in A_r toward $b \sim 2^\circ$ for stars with distances above 0.9 kpc, thus providing a robust and fairly precise lower distance limit for that dust cloud!

Differences between best-fit A_r values determined here and the SFD map are illustrated in Figure 27. Since the latter corresponds to extinction along the line of sight to infinity, our values are systematically smaller in regions with large A_r and similar at large Galactic latitudes, as expected. A detailed analysis of these A_r differences, when combined with stellar distance estimates, can provide valuable constraints for various ISM studies. For example, in Figure 28 we demonstrate good correspondence between the A_r differences and the distribution of molecular (CO) emission; our results imply that those molecular clouds must be more distant than ~ 1 kpc, and that the substructure seen around $b \sim -2.5$ is more distant than the one at $b \sim 2^\circ$ (see also Figure 26, and a more quantitative discussion in Section 4.1). Other SEGUE strips contain more examples where such “bracketing” of distances to molecular clouds can be attempted.

We note that the SFD map is expected to sometimes fail at low Galactic latitudes not just because of stars being embedded in dust, but also because its construction relied upon accurate point source subtraction (which is only performed for $|b| < 4.7^\circ$) and dust having a single temperature along each line of sight. These assumptions might be violated in the Galactic plane and

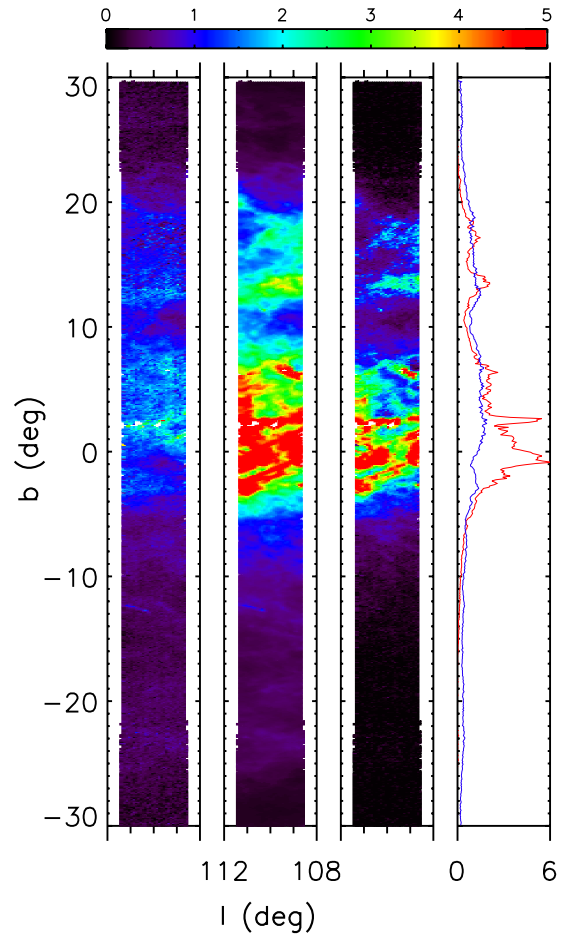


Figure 27. Analysis of the differences between best-fit A_r values (left panel, based on only-SDSS data; SDSS–2MASS version looks similar) and the SFD values (second panel) for stars with $\chi^2_{\text{pdf}} < 2$ and main-sequence distance in the range 0.8–1.2 kpc. The third panel shows the difference of the two A_r values (the second panel minus the first panel). Each 6×6 arcmin² pixel in the first three panels is color coded according to the top legend. The fourth panel shows the median best-fit A_r (blue line) and the median SFD value (red line) for 0.2 wide bins of Galactic latitude. If the SFD maps are correct, then the dust structures discernible in the two right panels at $b \sim 0^\circ$ and $b \sim +2^\circ$ must be more distant than ~ 1 kpc. This conclusion is independently confirmed for the latter dust cloud in Figure 26.

(A color version of this figure is available in the online journal.)

may be responsible for regions where SFD values are smaller than in our maps (e.g., at $b \sim 10^\circ$ – 20° in Figure 26).

3.2. Free R_V Case

If there is a significant discrepancy between the *shape* of assumed CCM extinction curve for $R_V = 3.1$ and that required by SEGUE data, photometric residuals between observed and best-fit magnitudes should show a correlation with best-fit A_r . Indeed, the failure to pass this test has revealed that our first instance of fitting erroneously used the O’Donnell extinction curve (due to an error in “metadata management”). In this case, the photometric residuals (data “minus” model) in the i band showed a highly statistically significant correlation $\Delta i = -0.015 A_r$, which implied that the adopted C_λ value in the i band was too large by 0.015 (the results for other bands did not require a change of C_λ). The analysis of used C_λ values clearly placed them on top of the O’Donnell parameterization in the right panel in Figure 4, while the revised value moved the constraint toward the CCM parameterization curves. After

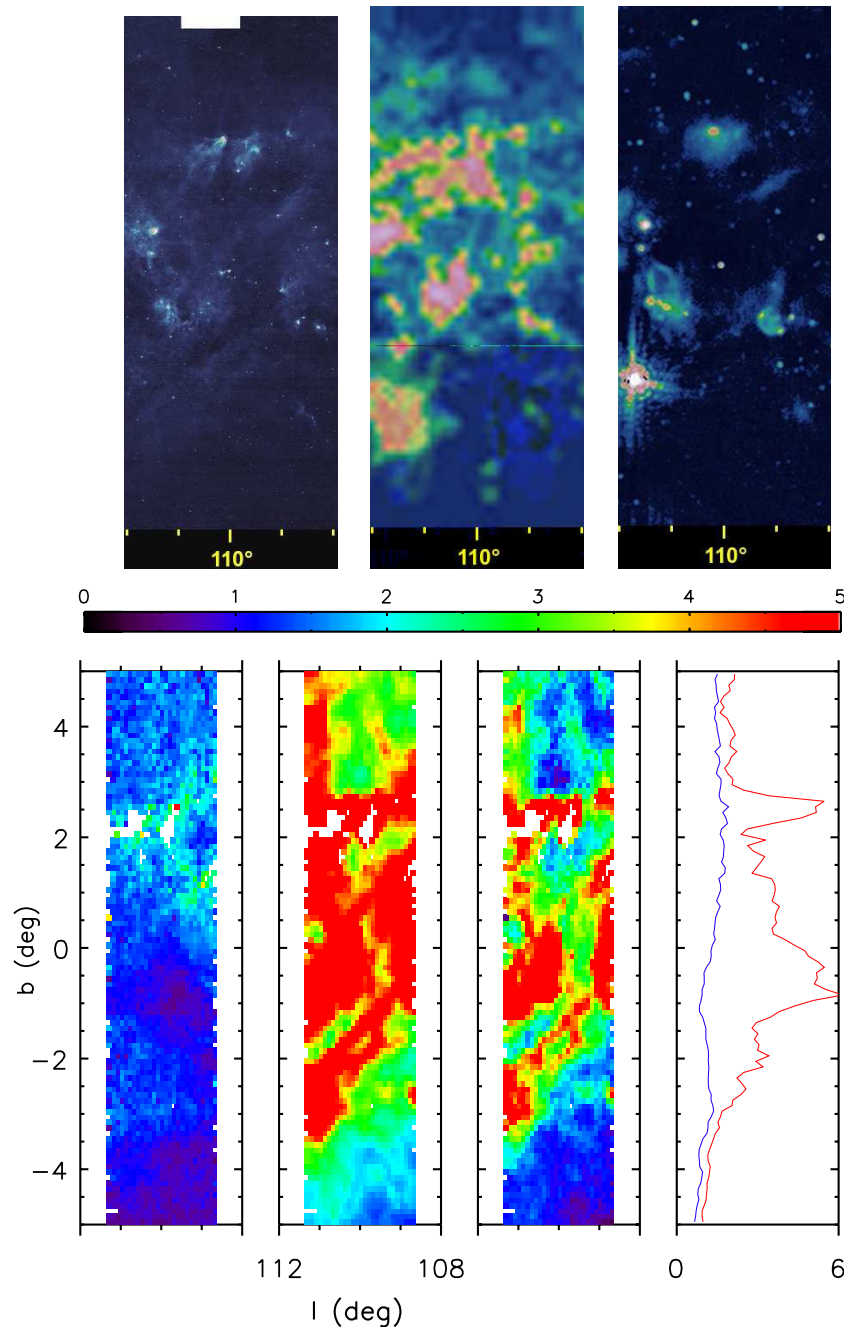


Figure 28. Bottom four panels show the $|b| < 5^\circ$ subregion of the panels shown in Figure 27. The top three panels show the mid-IR (left), CO (middle), and radio continuum (right) maps on approximately the same scale (obtained using “The Milky Way Explorer” by Kevin Jardine). The few small irregular white regions in the bottom three maps do not contain any stars with good photometry. Assuming that the SFD map is not grossly incorrect, the dust extinction determined here implies that most of the molecular cloud structures seen in the top middle panel must be more distant than ~ 1 kpc.

our second fitting iteration that correctly incorporated the CCM parameterization, we regressed photometric residuals and best-fit A_r again and found much smaller residuals: $\Delta i = -0.005 A_r$ and $\Delta z = 0.003 A_r$. For no other bands were the slopes larger than statistical measurement errors of at most 0.001. These two relatively small corrections of C_λ in the i and z bands result in a shift in the right panel in Figure 4 away from the CCM parameterization curves, and to a point between the constraints obtained using stellar locus method for Stripe 82 and the northern Galactic hemisphere! That is, the required C_λ modifications cannot be accomplished by adopting a CCM

parameterization curve for a different R_V (nor using any of the other two considered parameterizations). Hence, SEGUE data “knew” that (independent) empirical constraints on the shape of dust extinction curve from the high-latitude sky are better than the CCM parameterization for $R_V = 3.1$!

The above analysis of photometric residuals shows that there is no a priori reason to expect a significant departure from the canonical $R_V = 3.1$ value when R_V is considered a free fitting parameter. Nevertheless, it is possible that *localized* regions in the Galactic disk have a different R_V distribution, and given the unique nature of our sample, such a study is worthwhile.

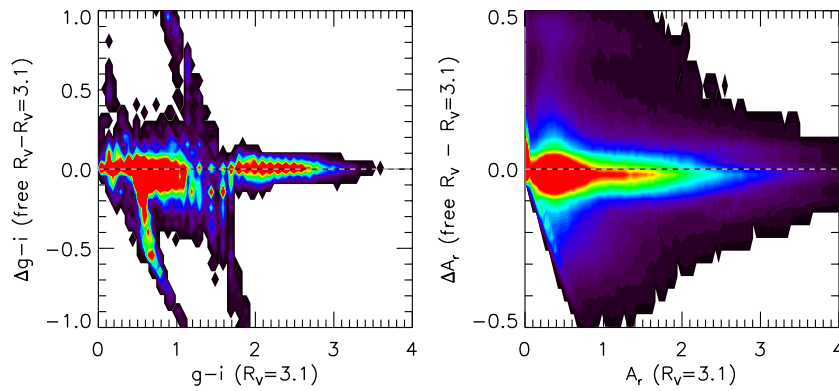


Figure 29. Comparison of the best-fit $g-i$ (left panel) and A_r (right panel) values for two different treatments of R_V , for stars in the $l = 110^\circ$ SEGUE strip (using SDSS–2MASS data). Only stars with best-fit $\chi^2_{\text{pdf}} < 2$, $r < 20$, and $K < 13.9$ (Vega) are used for the plot. The abscissae show the best-fit values obtained for a fixed $R_V = 3.1$ and the ordinates correspond to the residuals of the differences in the best-fit values when R_V is treated as a free-fitting parameter (“free R_V ” – “ $R_V = 3.1$ ”). The number density of stars increases from black to blue to red. The dashed lines are added to guide the eye.

(A color version of this figure is available in the online journal.)

The analysis of fitting results for a mock catalog described in Section 2.9.5 showed that only the SDSS–2MASS data set can be expected to provide useful constraints on R_V , and this is the fitting case analyzed here (for completeness, public data distribution includes also only-SDSS case).

A comparison of best-fit intrinsic colors and A_r between fixed- R_V and free- R_V cases is shown in Figure 29. While for some sources results can differ substantially, the fraction of discrepant sources is small. The resulting distribution of sources in the A_r versus distance diagram, shown in Figure 30 for free- R_V case, is similar to that based on fixed- R_V case (compare to Figure 21). A comparison of best-fits results for fixed- R_V and free- R_V cases shown in Figure 31 reveals that fit residuals are not significantly smaller when R_V is free.

The median R_V , as a function of the position in the A_r versus distance diagram, is shown in Figure 32 for four representative SEGUE stripes. As concluded in Section 2.9.5, the R_V results for $A_r < 1$ are expected to be biased low. For $A_r > 2$, and outside the red giant region, the median R_V does not deviate appreciably from its canonical value. A more quantitative description of this behavior is shown in Figure 33. For stars selected by 1 kpc $< D < 2.5$ kpc and $A_r > 2.5$ from $l = 110^\circ$ stripe, the median R_V is 2.90, with a mean of 2.95 and an rms of 0.22 (determined from the interquartile range, the sample size is ~ 9000 stars). Given various systematic uncertainties that cannot be smaller than 0.1–0.2, as well as expected random errors (~ 0.1), the median R_V is consistent with the canonical value of 3.1. We note that the width of the R_V histogram is about twice as large as the width of R_V determined using a fixed- R_V mock sample. Assuming that both widths are reliable, which may not be strictly quantitatively true, the implied intrinsic scatter in R_V for $l = 110^\circ$ stripe is ~ 0.2 . Results from other stripes are similar, with the median R_V showing a scatter of about 0.1. To illustrate this R_V variation, Figure 33 also shows the R_V distribution for $l = 70^\circ$ stripe, which has a median R_V of 2.80 and an rms of 0.15. We have tested for a possibility that the variation of the R_V distribution among stripes is due to calibration problems by comparing the median residuals between observed and best-fit magnitudes for each SDSS camera column (12 per stripe) and filter (including 2MASS filters). We did not find any evidence for photometric calibration errors larger than 0.01 mag.

As shown in Figure 32, candidate red giant stars (top left corner) have consistently somewhat larger values of R_V (by

about 0.2–0.4) than the typical star in the sample. Given that they are expected to be at much larger distances than main-sequence stars, it is possible that they sample different types of dust. However, given fairly large range of longitudes sampled by SEGUE stripes, this conclusion would imply that the dust in the Solar neighborhood (within 1–2 kpc) has anomalously low R_V . A more plausible explanation for increased R_V is a bias due to slight differences in SEDs between red giants and main-sequence stars. A preliminary analysis of the SDSS spectroscopic sample has revealed that spectroscopically confirmed giants show an offset from the Covey et al. locus in the seven-dimensional SDSS–2MASS color space. Such an offset is, at least in principle, capable of inducing a bias in best-fit R_V . A detailed analysis of this bias and differences in SEDs between main-sequence stars and red giants will be presented elsewhere. For the remainder of analysis presented here, we simply exclude candidate red giant stars.

A cross-section of the three-dimensional R_V map is shown in Figure 34 (recall that the R_V values are not reliable in regions of small A_r ; see the rightmost panel for reference). For most of high- A_r regions, the median values are consistent with the canonical values.

4. THE THREE-DIMENSIONAL DISTRIBUTIONS OF DUST AND STARS

Best-fit stellar distance and extinction along the line of sight, A_r , determined here can be used to infer the three-dimensional distributions of dust and stars. The determination of these distributions is not straightforward. In case of stars, complicated flux–color–extinction selection effects must be taken into account in order to obtain unbiased distributions. This analysis is best done with the aid of mock catalogs, such as those produced by *Galfast*. In case of dust, the complexity is further increased because the *integral* of dust volume density along the line of sight is constrained, and not the density itself. To translate these constraints into a positive dust volume density (more precisely, extinction per unit length as a function of position in the Galaxy), a careful statistical treatment of all errors and selection effects is mandatory. Since the full analysis is obviously far beyond this preliminary investigation, we illustrate the potential of our data set with two simplified analysis examples.

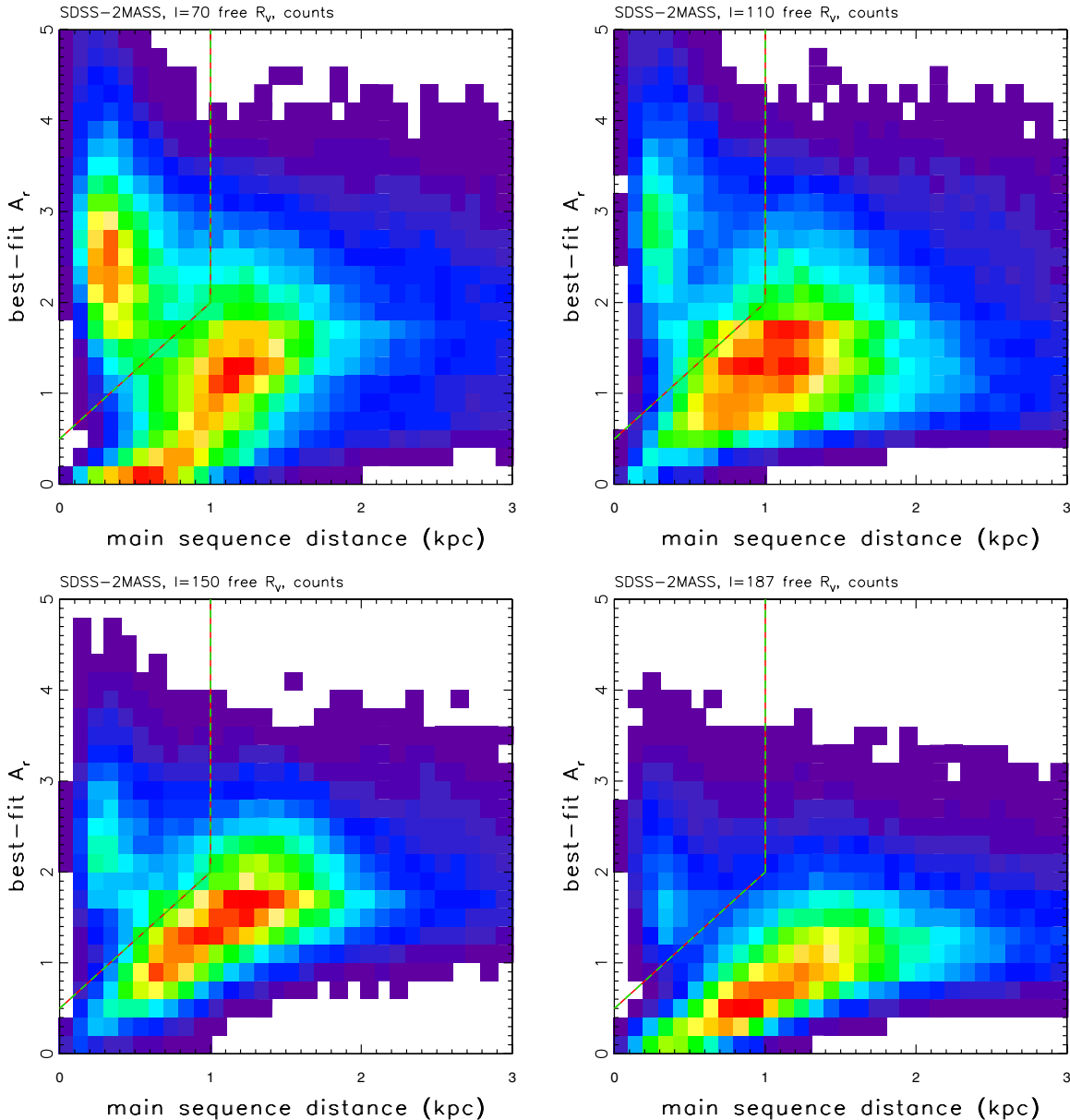


Figure 30. A_r map analogous to Figure 21, except that R_V is treated as a free parameter. Only stars with $|b| < 5^\circ$, $\chi^2_{\text{pdf}} < 2$, $r < 19$, and $K < 15$ (on Vega scale) are used.

(A color version of this figure is available in the online journal.)

4.1. The Spatial Distribution of Dust

A coarse approximate map of the spatial distribution of dust in a given distance range can be obtained by subtracting two median A_r maps corresponding to the distance limits of the chosen range. This method is not statistically optimal, but it suffices for simple visualization. Figure 35 shows the result of such analysis for mean bin distances of 1.0, 1.5, 2.0, and 2.5 kpc, with limiting bin distances 0.5 kpc larger and smaller than the mean distance.

It is easily discernible that the dust structures observed at $b \sim 2^\circ$ and $b \sim 13^\circ$ are confined to 1–1.5 kpc distance range, while the structure seen at $-3^\circ < b < 0^\circ$ is due to dust at a distance of ~ 2.5 kpc and subtends < 1 kpc along the line of sight (an analogous panel for a mean distance of 3.0 kpc shows that this structure is mostly confined to smaller distances). As discussed earlier, this ability to “bracket” distances to dust

clouds, and in turn to molecular clouds, is an important feature of our data set.

Another projection of our data set, the median A_r as a function of spatial coordinates, is shown in Figure 36 for all 10 SEGUE stripes. Aside from the fact that data for each stripe also resolve the third direction (Galactic longitude), this projection illustrates the integral constraint on the spatial distribution of dust. For each pixel, or a star in general case, the measured A_r contains (noisy) information about the dust distribution along the line connecting this pixel/star and the observing point (the origin in this figure). With an appropriate model description of dust distribution, either parametric or non-parametric, these A_r maps can be used to constrain the model (for an example of similar analysis, see Jones et al. 2011). We point out that latitudes with most dust in a given stripe vary with the stripe longitude. For example, for the $l \sim 130^\circ$ stripe, the highest-extinction regions are found at positive latitudes,

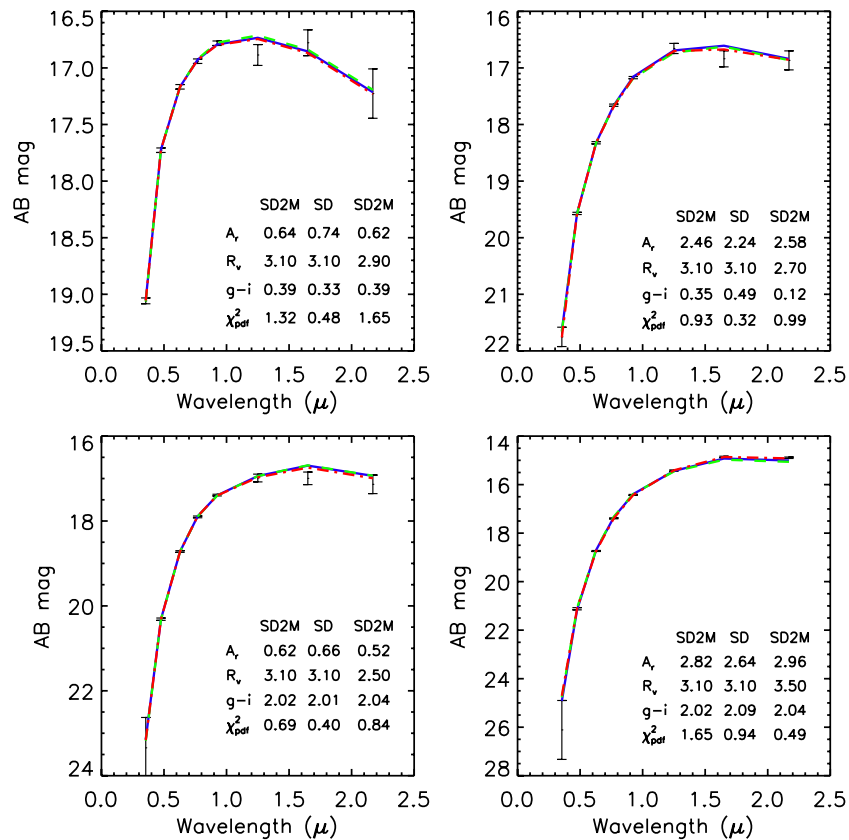


Figure 31. Comparison of three different types of best-fit SEDs: using only-SDSS data with fixed $R_V = 3.1$ (blue line) and using joint SDSS–2MASS data set with fixed R_V (green line) and with free R_V (red line). As demonstrated by the similarity of best-fit lines, the differences in best-fit parameters, listed in each panel, are due to degeneracies between intrinsic stellar color, amount of dust, and R_V . The shown cases correspond to blue and red stars (top row vs. bottom row), and small and large A_r (left column vs. right column).

(A color version of this figure is available in the online journal.)

while for the $l \sim 230^\circ$ stripe, most dust is found at negative latitudes.

4.2. The Spatial Distribution of Stars

The spatial distribution of stars (the number volume density) is shown in Figure 37. We have accounted for the change of volume with distance, but the variable distance limit due to faint flux cutoff and variable A_r is not taken into account and is clearly visible in the figure. To fully exploit these data for constraining Galactic structure models, a three-dimensional dust map must first be derived from A_r constraints (or at least carefully considered to mask high-extinction regions), and then one must apply color-dependent distance corrections.

Nevertheless, several encouraging features are already discernible in Figure 37. First, the sample seems fairly complete for distances below 1 kpc, corresponding to vertical distances from the plane of up to $|Z| \sim 0.5$ kpc. This volume is poorly explored by SDSS high-latitude data (e.g., see Figure 15 in J08) and the data set presented here will enable detailed studies of the disk stellar number density profile for small $|Z|$ (e.g., is the exponential profile valid within 100 pc from the disk mid-plane?). Second, the stellar number density at a fiducial location (say, at a distance of 0.5 kpc and $Z = 0.3$ kpc) significantly varies with Galactic longitude. This is expected behavior for an exponential disk profile in the galactocentric radial direction, and these data can be used to improve the exponential scale length estimates for thin and thick disks (for more details, please see Section 4 in J08).

5. SUMMARY AND DISCUSSION

This is the first analysis based on SDSS data that simultaneously estimates intrinsic stellar color and dust extinction along the line of sight for several tens of millions of stars detected in the low Galactic latitude SEGUE survey. The fitting method and various assumptions are described in Section 2. Our main results are the following.

1. The wavelength range spanned by the SDSS photometric system and the delivered photometric accuracy are sufficient to constrain the intrinsic stellar SED and dust extinction along the line of sight. The minimum required photometric accuracy of ~ 0.03 mag prevents non-unique solutions in most cases, and the accuracy of best-fit parameters scales roughly linearly with smaller errors. At the same time, this accuracy requirement effectively limits the sample to about $r < 19$.
2. Using the joint SDSS–2MASS photometry for stars at high Galactic latitudes, we confirmed the SDSS-based result from Sch2010 that the O’Donnell (1994) reddening law can be rejected. We adopted the Cardelli et al. (1989) reddening law in this work, which is similar to the Fitzpatrick (1999) reddening law adopted by Sch2010. Formally, both parameterizations are mildly inconsistent with the SDSS–2MASS data, but in practice photometric implications of these differences are minor (~ 0.01 mag when $A_r = 1$). We recommend the coefficients listed in the first row in Table 1 for correcting SDSS and 2MASS photometry for interstellar dust extinction.

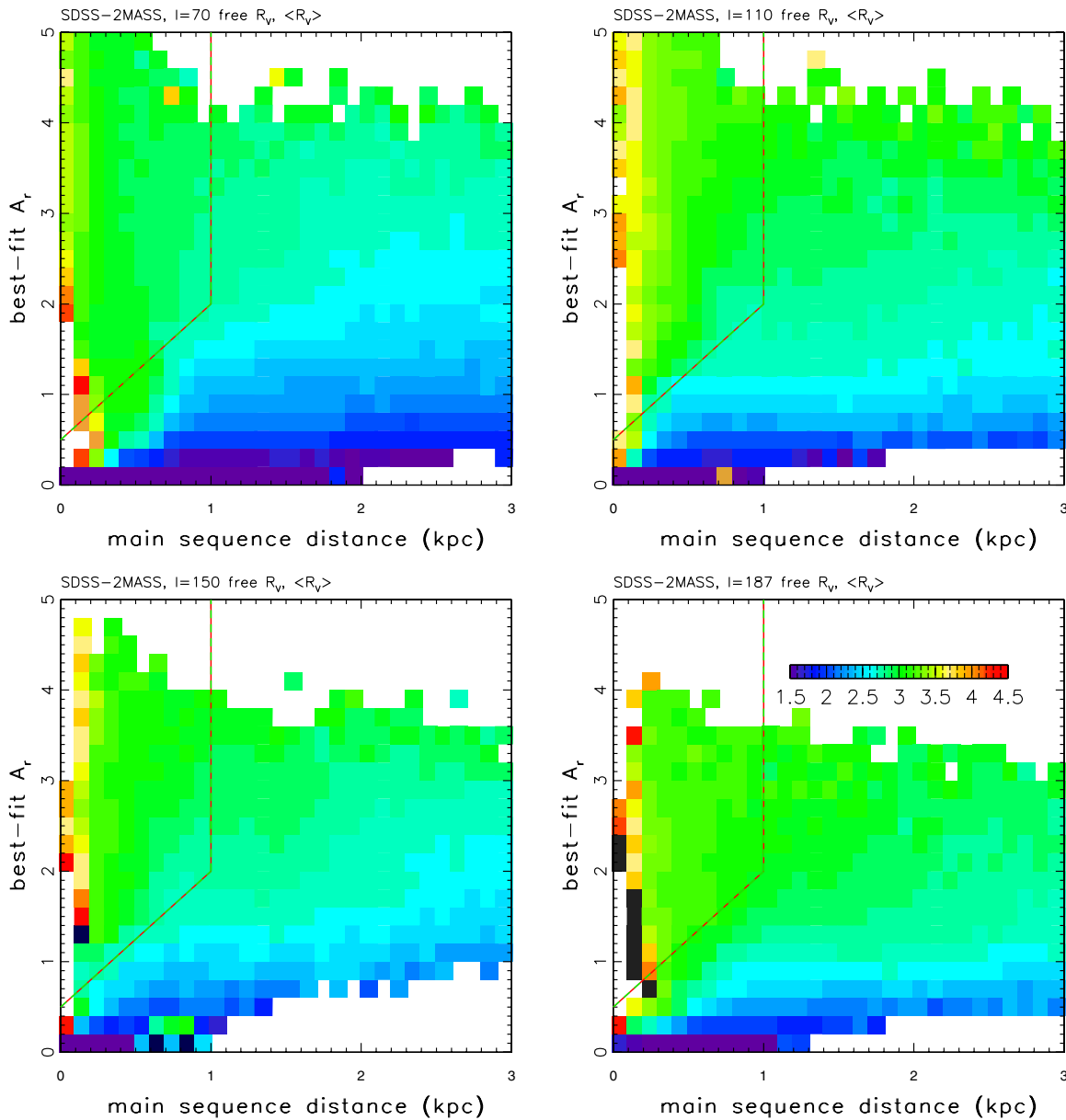


Figure 32. Similar to Figure 21, except that R_V is treated as a free parameter, and the color-coded map shows the median value of R_V (ranging from blue for $R_V = 1.5$ to red for $R_V = 4.5$, green corresponds to $R_V = 3$; see the legend in the bottom right panel). Only stars with $|b| < 5^\circ$, $\chi^2_{\text{pdf}} < 2$, $r < 19$, and $K < 15$ (on Vega scale) are used. Note that red giant stars (top left corner) have consistently larger values of R_V , and that consistently $R_V < 3$ when $A_r < 1$ for main-sequence stars. In other regions in this diagram where R_V is determined robustly, $R_V = 3.1$ cannot be ruled out in any of the 10 SEGUE stripes at a precision level of ~ 0.1 – 0.2 .

(A color version of this figure is available in the online journal.)

- For stars detected by both SDSS and 2MASS, and when R_V is not a free fitting parameter, the best-fit intrinsic stellar color and A_r for only-SDSS (four colors) and SDSS-2MASS (seven colors) fitting cases are similar. Although SDSS samples reach much further than SDSS-2MASS samples at high Galactic latitudes (the distance limits for blue stars differ by about a factor of 10), this is not the case at low Galactic latitudes because observed sources are much redder due to dust. The main benefit of only-SDSS samples is about a factor of two larger distance limit for blue main-sequence stars; however, the limiting distance for red stars is smaller than for SDSS-2MASS case due to a necessary limit on the u -band photometric errors.
- The SDSS photometry is not sufficient to reliably estimate R_V , with a realistic mock catalog implying errors of about 1. However, the addition of 2MASS photometry significantly improves the accuracy of R_V estimates, with realistic mock catalogs implying errors of about 0.3 when $A_r \sim 1$, and as small as 0.1 for $A_r > 4$. When R_V can be reliably estimated, we find that $R_V = 3.1$ cannot be ruled out in any of the 10 SEGUE strips (at a systematic-limited precision level of ~ 0.1 – 0.2). Our best estimate for the intrinsic scatter of R_V in the regions probed by SEGUE stripes is $\lesssim 0.2$.
- Simultaneous fits for the intrinsic stellar SED and dust extinction along the line of sight allow for efficient recognition of candidate red giant stars in the disk ($|b| < 5^\circ$). The selection method, which we dub “dusty parallax relation,”

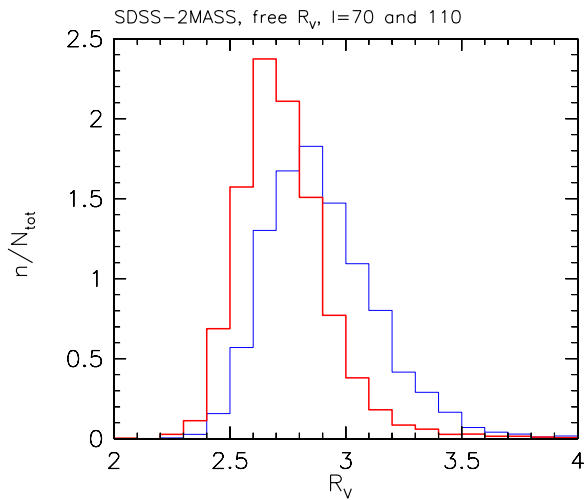


Figure 33. Comparison of the best-fit R_V values for SDSS-2MASS free- R_V case and stars with distances in the 1.0–2.5 kpc range and $A_r > 2.5$, selected from $l = 70^\circ$ (red, left histogram) and $l = 110^\circ$ (blue, right histogram) stripes (other selection criteria are the same as for stars plotted in Figure 32).

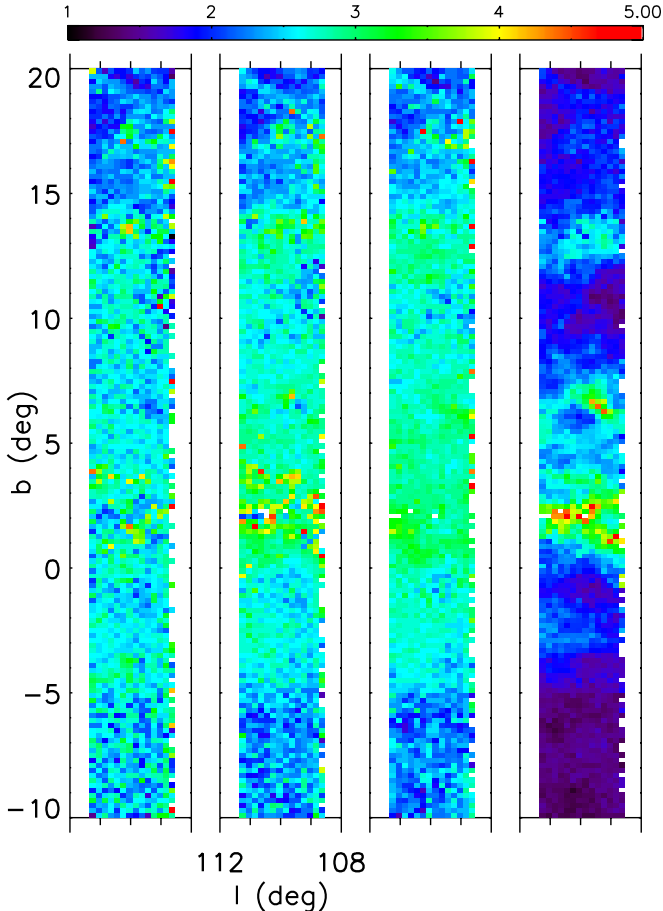


Figure 34. First three panels show the median R_V obtained using SDSS-2MASS sample for the SEGUE $l = 110^\circ$ strip, and for distance range 0.5–0.7 kpc (first), 0.7–0.9 kpc (second), and 0.9–1.1 kpc (third). Only stars outside the “red giant” region, see Figure 21, and with $\chi^2_{\text{pdf}} < 2$, $r < 21$, and $K < 14.3$ (Vega) are used for the plot. The pixel size is 6×6 arcmin², and the R_V coloring scheme is shown at the top. The fourth panel shows for reference the best-fit A_r , for the distance slice 0.9–1.1 kpc. Note that R_V is not reliable for $A_r < 2$ (black and blue regions in the fourth panel).

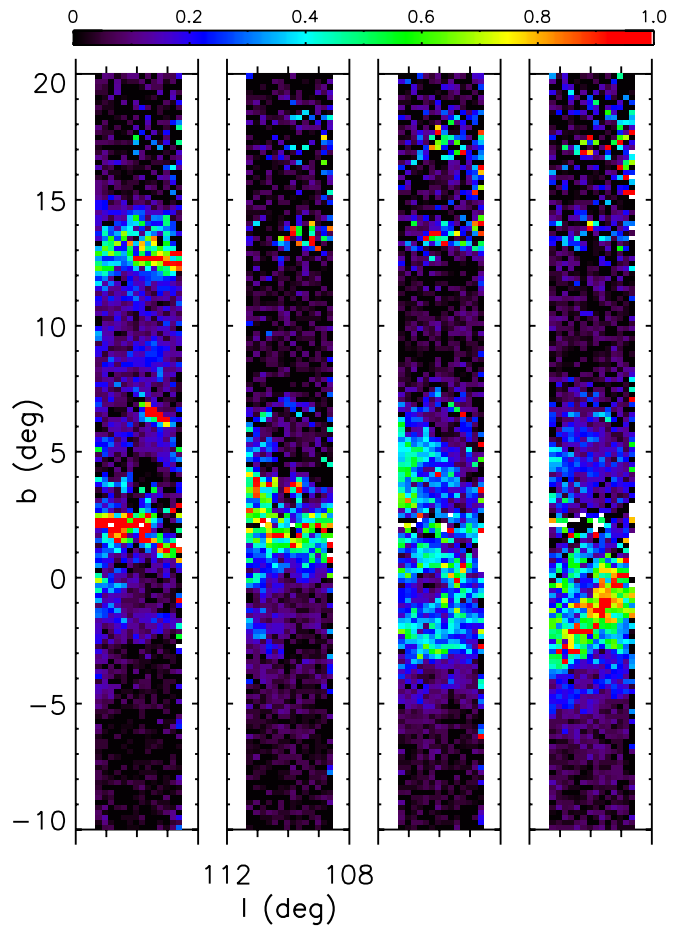


Figure 35. Illustration of the three-dimensional dust distribution for SEGUE stripe $l \sim 110^\circ$ at mean distances of 1.0, 1.5, 2.0, and 2.5 kpc, using only-SDSS sample and fixed- R_V fits. Unlike other figures that show the median A_r along the line of sight, this figure shows the differences in the median A_r (per 12×12 arcmin² pixel) for samples at distances between the quoted distance and limiting distances 0.5 kpc larger and smaller than the mean distance (e.g., the first panel shows the difference between the median A_r for 0.5–1.0 kpc and 1.0–1.5 kpc subsamples). It is easily discernible that the dust structures observed at $b \sim 2^\circ$ and $b \sim 13^\circ$ are confined to 1–1.5 kpc distance range, while the structure seen at $-3^\circ < b < 0^\circ$ is due to dust at a distance of ~ 2.5 kpc (an analogous panel for a mean distance of 3.0 kpc shows that this structure is mostly confined to smaller distances). Note that the linear extent perpendicular to the line of sight of a given angular size is 2.5 times larger in the last than in the first panel.

utilizes the increase of dust extinction with distance and identifies candidate giants as stars with anomalously large best-fit A_r for their best-fit main-sequence distance.

6. The SDSS-2MASS photometric data set allows robust mapping of the three-dimensional spatial distributions of main-sequence stars and dust to a distance of about 2 kpc (and $A_r \lesssim 2-3$). To extend this distance limits, deeper optical and infrared data are needed. With LSST and *Wide-Field Infrared Survey Explorer* (WISE) data sets (see below), the distance limit could be extended by close to a factor of 10.
7. The three-dimensional spatial distributions of stars and dust can be readily analyzed with the data sets discussed here, which we make public (see Appendix B). For most scientific applications, we recommend the use of the SDSS-2MASS data set with fits based on all seven colors and with R_V fixed to its canonical value. For studies exploring the R_V variations, the use of the full SDSS-2MASS data set is

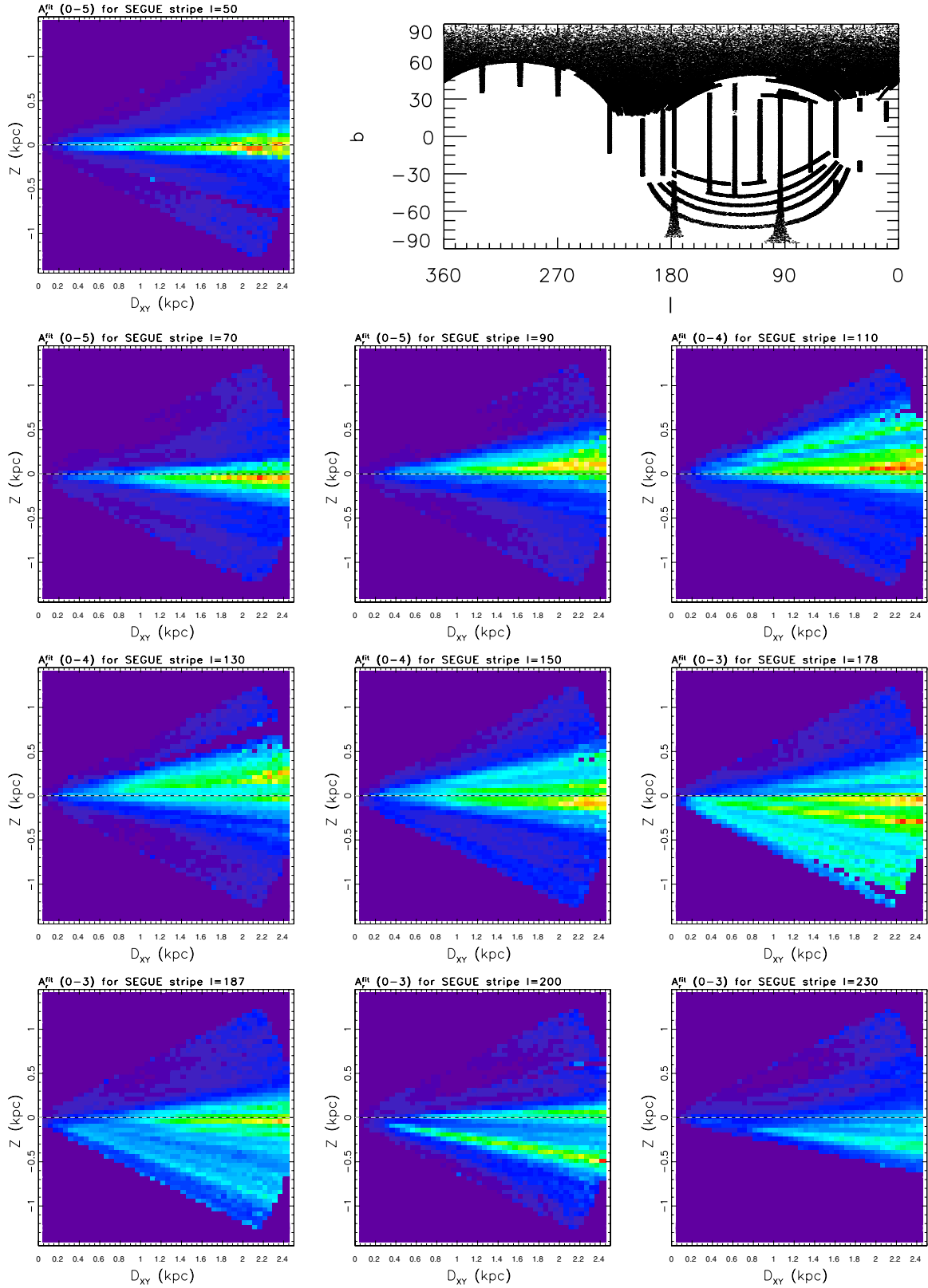


Figure 36. Median best-fit A_r (extinction along the line of sight) is shown as a function of distance from the Galactic plane, z , and distance along the plane, D_{xy} , for 10 SEGUE stripes (this is not a cross-section of three-dimensional dust distribution!). The best-fit A_r are based on the SDSS-2MASS data set and fixed- R_V fitting case, for stars with $\chi^2_{\text{pdf}} < 2$ and $K < 15$ (Vega). Each pixel is $50 \times 50 \text{ pc}^2$ and subtends $2:5$ wide stripe in the perpendicular (longitude) direction. The color scheme increases linearly from blue to red with a varying maximum value: 5 for the first three panels, 4 for the next three, and 3 for the last four panels.

(A color version of this figure is available in the online journal.)

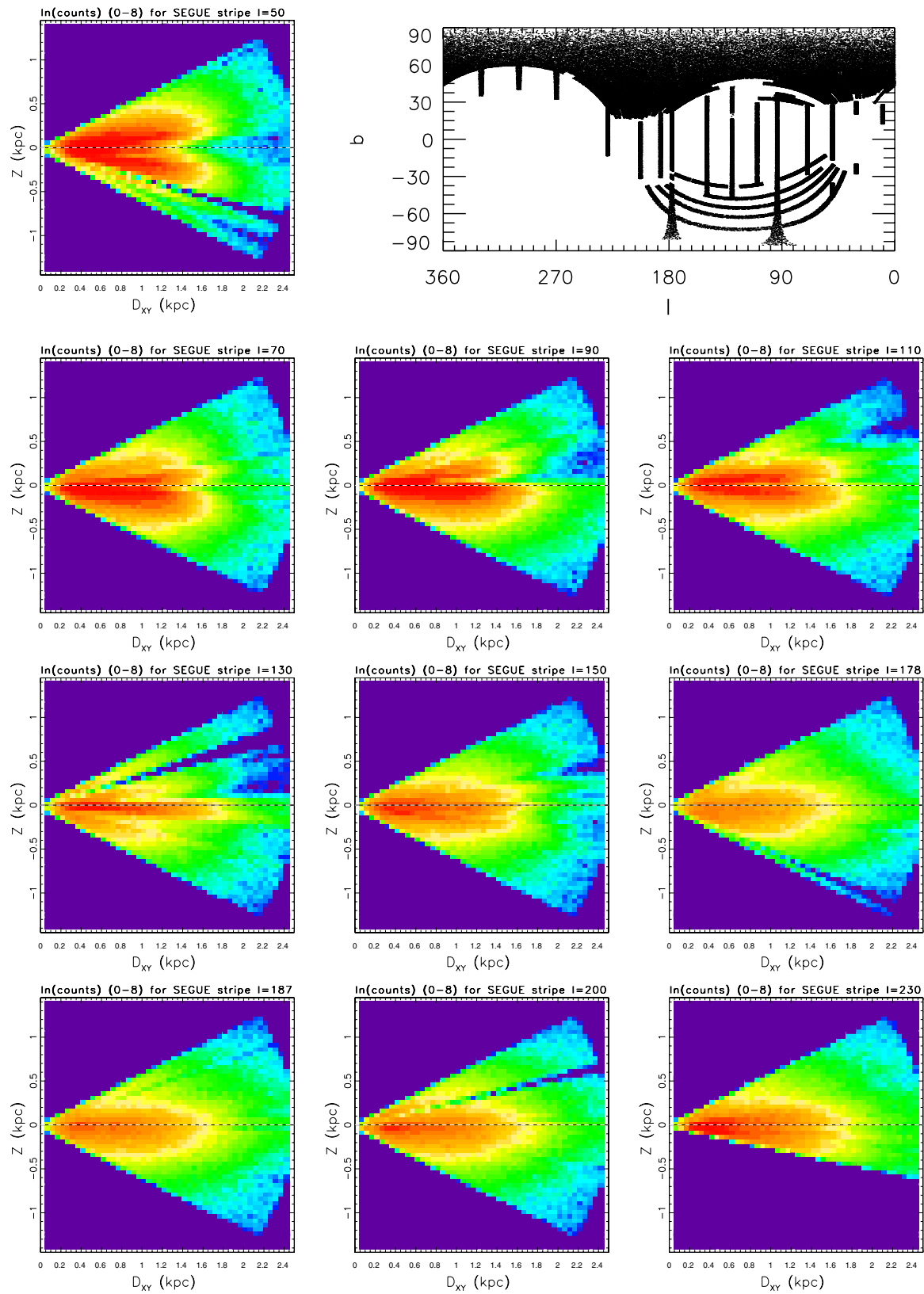


Figure 37. Local volume number density of stars is shown as a function of distance from the Galactic plane, z , and distance along the plane, D_{xy} , for the same samples as shown in Figure 36. The color scheme shows the counts on log scale with the same arbitrary normalization for all stripes. The falloff of the stellar volume number density at distances beyond ~ 1 kpc is due to the stellar color-dependent sample distance limit and does not reflect the disk structure. Note the variation of counts with Galactic longitude (the top four panels are closer to the Galactic center and contain more stars per unit volume).

(A color version of this figure is available in the online journal.)

mandatory, with best-fit R_V trustworthy only for stars with $\chi_{\text{pdf}}^2 < 2$ and $A_r > 1$. Our fits represent a “stress test” for both SDSS and 2MASS photometry, and *we emphasize that careful quality cuts must be applied to avoid unreliable results!*

Given the results presented by Sch2010, Peek & Graves (2010), Jones et al. (2011) and here, it is confirmed beyond doubt that there are some systematic problems with the normalization of SFD extinction map. Nevertheless, at high Galactic latitudes with small extinction these errors do not dominate over the photometric zero-point calibration errors in SDSS data (0.01–0.02 mag), and at low Galactic latitudes most stars are embedded in dust and thus the SFD map is of limited use.

Analysis described at the beginning of Section 3.2 shows that the data sets analyzed here can robustly distinguish predictions made by the three popular parameterizations for the shape of dust extinction curve. The O’Donnell parameterization is clearly excluded, and the other two parameterizations do not provide a perfect fit to data either. On the other hand, the differences are very small and not much larger than systematic errors in photometry. The systematic photometric and other errors translate to a systematic uncertainty in R_V of about 0.1–0.2. We did not detect any deviations from the canonical value $R_V = 3.1$ at this precision level. We reach the same conclusion by Jones et al. (2011), but here we obtained several times smaller errors due to a much wider wavelength range of utilized photometry. This uniformity of dust properties within a fairly large volume (distance limit of the order 1 kpc) probably implies that the ISM dust is well mixed during its lifetime (Draine 2011).

Last but not least, it will be very informative to directly compare the results presented here with those obtained by other methods, such as near-infrared color excess method (Lombardi & Alves 2001; Lombardi et al. 2011; Majewski et al. 2011), H α -based method (Sale et al. 2009), and Wolf method that is sensitive to gray dust (Yasuda et al. 2007; Gorbikov & Brosch 2010), to uncover and quantify various systematic errors that are likely to exist in all methods.

The results presented here will be greatly improved by several upcoming large-scale, deep optical surveys, including the Dark Energy Survey (Flaugher 2008), the Pan-STARRS (Kaiser et al. 2002), and the LSST (Ivezić et al. 2008b). These surveys will significantly extend the faint limit of the sample analyzed here (in case of LSST by ~ 5 mag) and are likely to provide more reliable photometry due to multiple observations and the use of photometric methods designed for crowded fields. Although 2MASS is too shallow to fully complement these new optical surveys, it will still provide very useful constraints in high-extinction regions. Furthermore, the recently released WISE data (Wright et al. 2010) will provide supplemental constraints with its W1 band at $3.4 \mu\text{m}$, which reaches about 2 mag deeper than 2MASS K band. These new data sets are thus certain to provide valuable new information about the dust and stellar distribution within the Galactic disk beyond the current limiting distance of a few kpc.

Ž. Ivezić and B. Sesar acknowledge support by NSF grants AST-615991 and AST-0707901, and by NSF grant AST-0551161 to LSST for design and development activity. Ž. Ivezić thanks the University of Zagreb, where a portion of this work was completed, for its hospitality, and acknowledges support by the Croatian National Science Foundation grant O-1548-2009. M. Berry, Ž. Ivezić, and B. Sesar acknowledge hospi-

tality by the Institute for Astronomy, University of Hawaii. D. Finkbeiner and E. Schlafly acknowledge the support of NASA grant NNX10AD69G. This work was supported by the Director, Office of Science, Office of High Energy Physics, of the U.S. Department of Energy under Contract No. DE-AC02-05CH11231. T. C. Beers acknowledges partial support from PHY 08-22648: Physics Frontier Center/Joint Institute for Nuclear Astrophysics (JINA), awarded by the U.S. National Science Foundation. We acknowledge the hospitality of the KITP at the University of California, Santa Barbara, where part of this work was completed (supported by NSF grant PHY05-51164). Fermilab is operated by Fermi Research Alliance, LLC under Contract No. DE-AC02-07CH11359 with the United States Department of Energy.

Funding for the SDSS and SDSS-II has been provided by the Alfred P. Sloan Foundation, the Participating Institutions, the National Science Foundation, the U.S. Department of Energy, the National Aeronautics and Space Administration, the Japanese Monbukagakusho, the Max Planck Society, and the Higher Education Funding Council for England. The SDSS Web site is <http://www.sdss.org/>. The SDSS is managed by the Astrophysical Research Consortium for the Participating Institutions. The Participating Institutions are the American Museum of Natural History, Astrophysical Institute Potsdam, University of Basel, University of Cambridge, Case Western Reserve University, University of Chicago, Drexel University, Fermilab, the Institute for Advanced Study, the Japan Participation Group, Johns Hopkins University, the Joint Institute for Nuclear Astrophysics, the Kavli Institute for Particle Astrophysics and Cosmology, the Korean Scientist Group, the Chinese Academy of Sciences (LAMOST), Los Alamos National Laboratory, the Max-Planck-Institute for Astronomy (MPIA), the Max-Planck-Institute for Astrophysics (MPA), New Mexico State University, Ohio State University, University of Pittsburgh, University of Portsmouth, Princeton University, the United States Naval Observatory, and the University of Washington.

APPENDIX A

SQL QUERY EXAMPLE

The following SQL query was used to select and download data for all SDSS stars with spectroscopic and proper-motion measurements (see <http://casjobs.sdss.org/CasJobs>).

```
SELECT
  round(p.ra,6) as ra, round(p.dec,6) as dec,
  p.run, p.camcol, p.field,
  --- comments are preceded by ---
  round(p.extinction_r,3) as rExtSFD,
  --- r band extinction from SFD
  round(p.modelMag_u,3) as uRaw,
  --- N.B. ISM-uncorrected model mags
  round(p.modelMag_g,3) as gRaw,
  --- rounding up
  round(p.modelMag_r,3) as rRaw,
  round(p.modelMag_i,3) as iRaw,
  round(p.modelMag_z,3) as zRaw,
  round(p.modelMagErr_u,3) as uErr,
  round(p.modelMagErr_g,3) as gErr,
  round(p.modelMagErr_r,3) as rErr,
  round(p.modelMagErr_i,3) as iErr,
  round(p.modelMagErr_z,3) as zErr,
  (case when (p.flags & '16') = 0 then 1
   else 0 end) as ISOLATED,
```

```

ISNULL(round(t.pmL,3), -9999) as pmL,
  --- proper motion data are set to
ISNULL(round(t.pmB,3), -9999) as pmB,
  --- -9999 if non-existent (NULL)
ISNULL(round(t.pmRaErr,3), -9999) as pmErr
  --- if pmErr < 0 no pm data
INTO mydb.dustSample
FROM phototag p LEFT OUTER JOIN propermotions
  t ON
  (p.objID = t.objID and t.match = 1 and
  t.sigra < 350 and t.sigdec < 350)
  --- quality cut on pm
WHERE
  p.type = 6 and          --- select
  unresolved sources
  (p.flags & '4295229440') = 0 and
  --- '4295229440' is code for no
  --- DEBLENDED_
  AS_MOVING or SATURATED objects
  p.mode = 1 --- PRIMARY objects only,
  which implies
  --- !BRIGHT && (!BLENDED ||
  NODEBLEND || nchild == 0)]
  p.modelMag_r < 21 --- adopted faint limit
  --- the end of query

```

APPENDIX B

DATA DISTRIBUTION

All data files, as well as a detailed description of their content, are available from a public data repository.²⁷ Due to the large data volume, we separate our catalogs into four groups. We fit stellar SEDs twice for all 10 SEGUE strips: once with selective extinction fixed at $R_V = 3.0$ and a second time with R_V as a free fitting parameter (limited to the range 1–7.9). Similarly, we present the only-SDSS and SDSS–2MASS data sets separately. For the $R_V = 3.0$ case, the data files in each data set (only-SDSS and SDSS–2MASS) are defined by Galactic coordinates, and are designed to contain fewer than 10 million stars each. For the free- R_V case, we distribute only the data from SEGUE strips with $|b| < 30^\circ$ because R_V is poorly constrained at higher Galactic latitudes with small extinction. This data organization allows users to download data for a relatively small region of sky without the burden of downloading the whole data set. These data sets are made available in two formats: as FITS tables and as plain ASCII text files.

All of the data files contain SDSS astrometry and photometry (and proper motions), the SFD value for A_r , and best-fit model parameters (including a best-fit distance estimate). Additionally, the SDSS–2MASS data files also contain 2MASS astrometry and photometry, the only-SDSS best-fit parameters, and the SDSS–2MASS best-fit parameters.

We emphasize that our fits represent a “stress test” for both SDSS and 2MASS photometry, and thus careful quality cuts must be applied to avoid unreliable results!

APPENDIX C

DISCUSSION OF THE METHODOLOGY

Here, we provide a more detailed discussion of two aspects of methods discussed in Section 2.

C.1. Closing the System of Equations

Stellar colors constrain reddening due to dust, e.g., $A_{ug} = A_u - A_g$, rather than dust extinction, here A_u and A_g . Therefore, when inferring the amount of dust extinction, both in case of single stars that are projected onto the unreddened stellar locus in the multi-dimensional color space, and in case of color offsets of the whole stellar locus at high Galactic latitudes, there is always one constraint *fewer* than the number of photometric bands. A convenient way of thinking about this “missing” equation is that dust extinction is described by its “scale” A_r and four (or seven in SDSS–2MASS case) measures of the *scaleless shape* of the extinction curve, $C_\lambda = A_\lambda/A_r$. Three different approaches can be used to “close” this system of equations, and to break “reddening-extinction” degeneracy (we do not discuss the best approach, based on *known* distance modulus, DM, and absolute magnitude, M_r , which directly constrains A_r via $r = M_r + DM + A_r$, because our data set does not include a parallax distance to the vast majority of stars).

The first approach assumes that A_r is provided as an additional input, for example, from the SFD map as A_r^{SFD} . In this case, $A_{ug} = (C_u - C_g) A_r^{\text{SFD}}$, and it is easy to show that

$$C_u = 1 + \frac{A_{ug} + A_{gr}}{A_r^{\text{SFD}}} \quad (\text{C1})$$

$$C_g = 1 + \frac{A_{gr}}{A_r^{\text{SFD}}} \quad (\text{C2})$$

$$C_i = 1 - \frac{A_{ri}}{A_r^{\text{SFD}}} \quad (\text{C3})$$

$$C_z = 1 - \frac{A_{ri} + A_{iz}}{A_r^{\text{SFD}}}. \quad (\text{C4})$$

If there are systematic errors in A_r^{SFD} , they will be propagated to C_m . Such effects can be tested for by tracing the variation of resulting C_m across the sky, and by correlating deviations with A_r^{SFD} . In particular, given many lines of sight, it is possible to fit a spatially invariant model for errors in A_r^{SFD} (e.g., an additive and a multiplicative error).

To illustrate the impact of errors in A_r^{SFD} on C_m determined with this method, we computed A_{color} using the CCM model with $R_V = 3.1$ and true $A_r = 1$, and we assumed a multiplicative error in A_r^{SFD} . A correction factor of 0.95 produces the overall best-fit $R_V = 3.28$, with the *i*- and *z*-band constraints on R_V biased to even higher values. For a correction factor of 0.9, the best-fit $R_V = 3.48$, with the *i* and *z* extinction values barely consistent with the CCM extinction curve. For additive errors such that the true $A_r = A_r^{\text{SFD}} + 0.05$, the best-fit R_V varies from 2.20 for $A_r^{\text{SFD}} = 0.1$ to 2.93 for $A_r^{\text{SFD}} = 1$. Therefore, this method is quite sensitive to systematic errors in A_r^{SFD} and should be used with caution.

The second approach uses a model-based extinction curve to predict C_m as a function of *single* parameter R_V . Given that there are three “spare” constraints, model predictions can be tested for self-consistency (and perhaps used to select the “best” model). This method results in estimates for A_r and can be used to test external maps, such as SFD, though *only in a model-dependent way*.

The third approach, adopted here, is to assume (fix) one value of C_m and solve for A_r and all remaining C_m . While at first this approach sounds arbitrary, it becomes sound when SDSS data

²⁷ http://www.astro.washington.edu/users/ivezic/r_datadepot.html

are augmented with 2MASS data. The reason is that the effective wavelength for the 2MASS K band is $2.2 \mu\text{m}$, which in this context is almost as large as infinity.²⁸ When using both SDSS and 2MASS, A_r is estimated using offsets of the $r-K$ color distribution. The main reason why this approach works is the fact that A_K/A_r is small (0.132) and varies little with R_V and among all plausible dust extinction models. For example, for $R_V > 2$ all models predict variations of A_K/A_r not exceeding 20%. This variation translates to only about a 3% error when the $r-K$ shift is interpreted as $A_r - A_K = (1 - A_K/A_r) A_r = 0.868 A_r$. When using this approach, there are seven colors constructed with eight photometric bands, and the result is estimates for A_r and six C_m .

C.2. Methods for Quantifying Color Offsets for the Stellar Locus

What is the optimal method for measuring A_{ug} , A_{gr} , etc., using the stellar locus? If we think of the stellar locus in a 2D color-color diagram as of an “image,” then we essentially “slide” the image of the reddened sample to perfectly align with the image of the “intrinsic” dereddened locus. This alignment can be performed in each 2D color-color diagram, or alternatively all four color shifts can be determined simultaneously in the 4D color space. At the other extreme, the color shifts can be determined using 1D projections of each color, as in the “blue tip” method proposed by Schlafly et al. (2010).

If there were no astrophysical systematics and measurement error distributions were fully understood, these methods should produce identical results (e.g., the $g-r$ offsets estimated from the $g-r$ versus $u-g$ and $r-i$ versus $g-r$ diagrams would be statistically consistent). However, there are astrophysical systematics, such as distance, age, and metallicity effects, that may introduce various biases. For example, M dwarf stars in SDSS sample can be as close as 100 pc and thus be within dust layer, and the “blue tip” is sensitive to age and metallicity of turnoff stars that define it. The idea behind the principal color method employed here is to avoid distance effects by considering only stars bluer than M dwarfs, and to mitigate age and metallicity effects by measuring shifts perpendicular to the locus. The reason for the latter is that age variation “extends” or “shortens” the locus (i.e., shifts the “blue tip”), but does not strongly affect its position in the perpendicular (P_2) direction. When considering metallicity, systematic effects are a little bit more complicated, but are mostly confined to the u band. For blue stars, the $g-r$ color is essentially a measure of effective temperature with negligible dependence on metallicity (Ivezić et al. 2008a). At a given $g-r$ color, the $u-g$ color depends on metallicity (it becomes bluer as metallicity decreases, see the top right panel in Figure 2 in Ivezić et al. 2008a). For example, at $g-r = 0.3$, the $u-g$ color varies by about 0.2 mag as the metallicity varies from the median thick-disk value (-0.5) to the median halo value (-1.5). This shift is not parallel to the locus in the $g-r$ versus $u-g$ color-color diagram, so it does have some effect on the P_2 distribution. However, already at $g-r = 0.5$, the fraction of halo stars in SDSS sample is sufficiently small that this effect becomes negligible (because such red halo stars are too faint to be detected by SDSS). Hence, in the range $0.5 < g-r < 1.2$, only the dust reddening (and photometric calibration errors, of course!) can significantly shift the locus perpendicularly to its blue part (even in the $u-g$ versus $g-r$ diagram). An added benefit from the S/N viewpoint is that the

P_2 distributions are very narrow, an advantage that mitigates the fact that the reddening vectors are measured only along P_2 directions.

REFERENCES

- Abazajian, K. N., Adelman-McCarthy, J. K., Agüeros, M. A., et al. 2009, *ApJS*, **182**, 543
- Amôres, E. B., & Lépine, J. R. D. 2005, *AJ*, **130**, 659
- Arce, H. G., & Goodman, A. A. 1999, *ApJ*, **512**, L135
- Bailer-Jones, C. A. L. 2011, *MNRAS*, **411**, 435
- Bond, N. A., Ivezić, Ž., Sesar, B., et al. 2010, *ApJ*, **716**, 1
- Cardelli, J. A., Clayton, G. C., & Mathis, J. S. 1989, *ApJ*, **345**, 245
- Covey, K. R., Ivezić, Ž., Schlegel, D., Finkbeiner, D., et al. 2007, *AJ*, **134**, 2398
- Draine, B. T. 2011, *Physics of the Interstellar and Intergalactic Medium* (Princeton, NJ: Princeton University Press)
- Eisenstein, D. J., Liebert, J., Harris, H., et al. 2006, *ApJS*, **167**, 40
- Finlator, K., Ivezić, Ž., Fan, X., Strauss, M. A., et al. 2000, *AJ*, **120**, 2615
- Fitzpatrick, E. L. 1999, *PASP*, **111**, 63
- Fitzpatrick, E. L., & Massa, D. 2009, *ApJ*, **699**, 1209
- Flaugher, B. 2008, in *A Decade of Dark Energy: Spring Symposium*, ed. N. Pirzkal & H. Ferguson, <http://www.stsci.edu/institute/conference/spring2008>
- Fukugita, M., Ichikawa, T., Gunn, J. E., et al. 1996, *AJ*, **111**, 1748
- Girardi, L., Groenewegen, M. A. T., Hatziminaoglou, E., & da Costa, L. 2005, *A&A*, **436**, 895
- Gorbikov, E., & Brosch, N. 2010, *MNRAS*, **401**, 231
- Gunn, J. E., Carr, M., Rockosi, C., et al. 1998, *AJ*, **116**, 3040
- Gunn, J. E., Siegmund, W. A., Mannery, E., et al. 2006, *AJ*, **131**, 2332
- Helmi, A., Ivezić, Ž., Prada, F., et al. 2003, *ApJ*, **586**, 195
- High, F. W., Stubbs, C. W., Rest, A., Stalder, B., & Challis, P. 2009, *AJ*, **138**, 110
- Hogg, D. W., Finkbeiner, D. P., Schlegel, D. J., & Gunn, J. E. 2001, *AJ*, **122**, 2129
- Ivezić, Ž., Lupton, R. H., Schlegel, D. J., et al. 2004, *Astron. Nachr.*, **325**, 583
- Ivezić, Ž., Sesar, B., Jurić, M., et al. 2008a, *ApJ*, **684**, 287
- Ivezić, Ž., Smith, J. A., Miknaitis, G., Lin, H., et al. 2007, *AJ*, **134**, 973
- Ivezić, Ž., Tyson, J. A., Acosta, E., et al. 2008b, [arXiv:0805.2366](https://arxiv.org/abs/0805.2366)
- Jones, D. O., West, A. A., & Foster, J. B. 2011, *AJ*, **142**, 44
- Jurić, M., Ivezić, Ž., Brooks, A., et al. 2008, *ApJ*, **673**, 864
- Kaiser, N., Aussel, H., Burke, B. E., et al. 2002, *Proc. SPIE*, **4836**, 154
- Knapp, G. R., & Kerr, F. J. 1974, *A&A*, **35**, 361
- Lombardi, M., & Alves, J. 2001, *A&A*, **377**, 1023
- Lombardi, M., Alves, J., & Lada, C. J. 2011, *A&A*, **535**, A16
- Lupton, R., Gunn, J. E., Ivezić, Z., Knapp, G. R., et al. 2001, in *ASP Conf. Ser. 238, Astronomical Data Analysis Software and Systems X*, ed. F. R. Harnden Jr., F. A. Primini, & H. E. Payne (San Francisco, CA: ASP), 269
- Magnier, E. A., Liu, M., Goldman, B., et al. 2010, *Highlights Astron.*, **15**, 818
- Majewski, S. R., Zasowski, G., & Nidever, D. L. 2011, *ApJ*, **739**, 25
- McGurk, R. C., Kimball, A. E., & Ivezić, Ž. 2010, *AJ*, **139**, 1261
- Meyer, J. M., Ivezić, Ž., Finkbeiner, D. P., et al. 2005, *BAAS*, **37**, 131
- O'Donnell, J. E. 1994, *ApJ*, **422**, 158
- Padmanabhan, N., Schlegel, D. J., Finkbeiner, D. P., et al. 2008, *ApJ*, **674**, 1217
- Peek, J. E. G., & Graves, G. J. 2010, *ApJ*, **719**, 415
- Pier, J. R., Munn, J. A., Hindsley, R. B., et al. 2003, *AJ*, **125**, 1559
- Richards, G. T., Fan, X., Schneider, D. P., et al. 2001, *AJ*, **121**, 2308
- Robin, A. C., Reylé, C., Derrière, S., & Picaud, S. 2003, *A&A*, **409**, 523
- Sale, S. E., Drew, J. E., Unruh, Y. C., et al. 2009, *MNRAS*, **392**, 497
- Schlafly, E. F., & Finkbeiner, D. P. 2010, [arXiv e-prints](https://arxiv.org/abs/1005.0007)
- Schlafly, E. F., Finkbeiner, D. P., Schlegel, D. J., et al. 2010, *ApJ*, **725**, 1175
- Schlegel, D. J., Finkbeiner, D. P., & Davis, M. 1998, *ApJ*, **500**, 525
- Sesar, B., Ivezić, Ž., & Jurić, M. 2008, *ApJ*, **689**, 1244
- Sesar, B., Ivezić, Ž., Lupton, R. H., Jurić, M., et al. 2007, *AJ*, **134**, 2236
- Skrutskie, M. F., Schneider, S. E., Stiening, R., Strom, S. E., et al. 1997, in *The Impact of Large Scale Near-IR Sky Surveys*, ed. F. Garzon, N. Epchtein, A. Omont, B. Burton, & P. Persi (Astrophysics and Space Science Library, Vol. 210; Dordrecht: Kluwer), 25
- Smith, J. A., Tucker, D. L., Kent, S., et al. 2002, *AJ*, **123**, 2121
- Smolčić, V., Ivezić, Ž., Knapp, G. R., et al. 2004, *ApJ*, **615**, L141
- Stoughton, C., Lupton, R. H., Bernardi, M., et al. 2002, *AJ*, **123**, 485
- Tucker, D. L., Kent, S., Richmond, M. W., et al. 2006, *Astron. Nachr.*, **327**, 821
- Wright, E. L., Eisenhardt, P. R. M., Mainzer, A. K., et al. 2010, *AJ*, **140**, 1868
- Yanny, B., Rockosi, C., Newberg, H. J., et al. 2009, *AJ*, **137**, 4377
- Yasuda, N., Fukugita, M., & Schneider, D. P. 2007, *AJ*, **134**, 698
- York, D. G., Adelman, J., Anderson, J. E., et al. 2000, *AJ*, **120**, 1579

²⁸ Please do not take this statement out of this context!